

**BOUNDARY LIPIDS OF PENTAMERIC LIGAND-GATED ION
CHANNELS IN MODEL AND NATIVE MEMBRANES**

BY

LIAM M. SHARP

A dissertation submitted to the
Graduate School—Camden
Rutgers, The State University of New Jersey
in partial fulfillment of the requirements
for the degree of
Doctor of Philosophy

Graduate Program in Computational and Integrative Biology

Written under the direction of
Grace Brannigan
and approved by

Dr Grace Brannigan

Dr Sean O'Malley

Dr Joseph Martin

Dr Jérôme Hénin

Camden, New Jersey

January 2021

© 2021

Liam M. Sharp

ALL RIGHTS RESERVED

ABSTRACT OF THE DISSERTATION

Boundary lipids of pentameric ligand-gated ion channels in model and native membranes

by LIAM M. SHARP

Dissertation Director:

Grace Brannigan

This thesis reports on molecular simulations of pentameric ligand-gated ion channels (pLGICs) in both model and quasi-realistic membranes. The goal is to identify specific pLGIC boundary lipids, how they are distributed around a pLGIC's transmembrane domain (TMD), and predict specific lipid binding affinities. To accomplish this we use coarse grained molecular dynamics simulation (CGMD). We present four projects examining pLGICs in a series of model and quasi-native membranes.

For project one, we determine which lipid domain a nAChR resides in through nearest neighbor analysis and boundary lipid enrichment across membrane compositions, and predict boundary lipid distributions for multiple membranes consisting of PUFAs, saturated lipids, and cholesterol. In the second project we expand on project one by simulating nAChRs in non-domain forming membranes containing the same acyl-chain fractions but different lipid topologies. Comparing the previous domain and current non-domain forming simulations, we analyzed the difference in bound acyl-chain saturation, protein subunit-subunit interactions, and differences in boundary lipid distributions. Third, we simulated ELIC as a model pLGIC in binary model membranes consisting of neutral and anionic lipids. Using both 1D enrichment and 2D density analysis we predict anionic

boundary lipid distributions around the annulus of *Erwinia* ligand-gated ion channel (ELIC). These model membrane studies paved the way for the fourth study: simulating nAChR in quasi-native neuronal membranes consisting of 36 unique lipid species and both neutral and anionic head groups. We use polar density enrichment analysis to predict specific boundary lipids and introduce a new method for calculating affinities for lipids occupying protein binding sites.

Acknowledgements

I would like to start with Dr. Brannigan, whose patience, encouragement, and guidance has brought forward the scientist I am today. To Dr. O’Malley, Dr. Martin, and Dr. Hénin for advice and suggestions. To Reza, who showed me the wonder of coding. To my lab mates off to newer things, Sruthi, Ruchi, Shashank, Kristen, and those still here, Jesse, Anushriya, Ezry, Connor, and Jahmal, thank you all so much! To my friends outside of the lab, Heather, Sean, Nidhi, Zheming, Sung, Chris, Nick, Cody, Nate, Steve, and Dan.

There is more to life than school however. To Garth, Laura, Josh, Scott, Liz, Jordan, Sairam, Michael, Mike, Yip, Alex, Alex, Jenny, Vickey and Dave: thank you all. Without you I would go mad. The occasional beer, the rambunctious D&D campaign, video games, and travel has all helped me get to this point.

To Dad, who would look at the work I was doing, and tell me to go to bed or go for a walk. To Caleb who would bug me until I listened to his new beat. To my Mom, who pushed me to accept making mistakes as part of the process.

While there are still more to thank, I have a finite number of pages. To both friends and family not mentioned, your support has meant so much to me. I would like to leave you with a quote by Sir Terry Pratchett.

“But then science is nothing but a series of questions that lead to more questions.” — Terry Pratchett, The Long Earth

Dedication

In memory of Kathleen McGovern, loving and eccentric mother of Liam and Caleb.

Table of Contents

Abstract	iii
Acknowledgements	v
Dedication	vi
List of Tables	xi
List of Figures	xiii
Introduction	1
1. Introduction	1
1.1. Pentameric Ligand-Gated Ion Channels	1
1.2. Lipids and Membranes	4
1.3. Boundary Lipids	6
1.4. Approaches to Determining pLGIC Boundary Lipids	7
1.5. Goals of this Thesis	9
2. Boundary lipids of the nicotinic acetylcholine receptor: spontaneous partitioning via coarse-grained molecular dynamics simulation	11
2.1. Abstract	11
2.2. Introduction	12
2.3. Methods	17
2.3.1. System Composition	17
2.3.2. Simulations	18

2.3.3. Analysis	19
2.4. Results	20
2.4.1. Domains formed in PUFA-containing ternary membranes are not affected by introduction of an nAChR	22
2.4.2. nAChR consistently partitions to the liquid disordered do- main	26
2.4.3. Spontaneous integration of lipids into nAChR TMD bundle	28
2.4.4. Lipid sorting over the 5-20 nm range is associated with larger domains	29
2.5. Discussion	32
3. Untangling direct and domain-mediated interactions between nico- tinic acetylcholine receptors in DHA-rich membranes	37
3.1. Abstract	37
3.2. Introduction	38
3.3. Methods	42
3.3.1. System setup	42
3.3.2. Simulation details	43
3.3.3. Analysis	44
3.4. Results	46
3.4.1. nAChR boundary lipid preferences	47
3.4.2. nAChR clustering in the presence and absence of lipid do- mains	52
3.4.3. Closest subunits across dimerizing proteins	52
3.5. Discussion	56
4. Direct binding of phosphatidylglycerol at specific sites modulates desensitization of a ligand-gated ion channel	58

4.1. Abstract	58
4.2. Introduction	59
4.3. Results	63
4.3.1. Selective binding of phospholipids to ELIC	63
4.3.2. Selective effect of POPG on ELIC stability and function .	66
4.3.3. Five interfacial arginines contribute to POPG binding . .	69
4.3.4. Specific interfacial arginines mediate POPG effect . . .	73
4.3.5. L240A reduces desensitization and enhances POPG binding	75
4.4. Discussion	78
4.5. Methods	84
4.5.1. Mutagenesis, expression and purification of ELIC	84
4.5.2. Native MS measurements	84
4.5.3. Thermal stability assay	86
4.5.4. Excised patch-clamp recordings from giant liposomes . .	87
4.5.5. Stopped-flow fluorescence recordings	89
4.5.6. Lipid extraction and MS analysis	90
4.5.7. Coarse-grained simulations of ELIC	91
4.6. Reference	93
5. Nicotinic Acetylcholine Receptor Boundary Lipid Characteriza-	
tion Within Native and Experimental Membranes	101
5.1. Abstract	101
5.2. Introduction	102
5.3. Methods	106
5.3.1. Simulation Composition	106
5.3.2. Simulations	107
5.3.3. Calculation of Polar Density Distributions	108

5.3.4. Calculation of the density-threshold affinity	110
5.3.5. Binding Site Definition and Occupancy Calculations	111
5.3.6. Calculation of Accessible Area	112
5.4. Results and Discussion	114
5.4.1. Effect of acyl chain on site selectivity among neutral lipids	115
5.4.2. Lipid preferences of intersubunit and M4 sites	117
5.4.3. Effect of Head Group Charge on Affinity Depends on Leaflet and Binding Site	119
5.4.4. Role of Individual Lipid Headgroups in Determining Affinity	121
5.5. Conclusions	123
Appendix A: GABA_AR and ELIC domain partitioning in polyunsaturated fatty acid rich model membranes	127
Appendix B : Chapter 2 Supplementary	130
Appendix C: Chapter 4 Supplementary	132
Appendix D: Chapter 5 Supplementary	134
Vita	150
Bibliography	155

List of Tables

3.1. Composition of nAChR Boundary Lipid chains in domain forming (homoacidic) and non-domain forming (heteroacidic) membranes.	47
4.1. ELIC WT activation and desensitization rate constants derived from a double exponential fit to the time course of flux in Fig. 4.4F (n=3, \pm SD).	68
5.1. Density-threshold affinities() of neutral lipids for both sites in the outer leaflet, by head group.	122
5.2. Density-threshold affinities(ΔG) of neutral lipids for both sites in the inner leaflet, by head group.	122
C1. Phophatidylethanolamine and phosphatidylglycerol species identi- fied in lipid extracts by MS/MS. Table shows m/z, intensity, mass and mass accuracy of each phospholipid species.	134
D1. Lipid ratios used for neuronal simulations grouped by head group. .	142
D2. Affinities broken down by headgroup and acyl chain to reveal cross- correlation.	144
D3.1.Complete listing of affinities for intersubunit sites in the outer leaflet.	145
D3.2.Complete listing of affinities for M4 sites in the outer leaflet. . . .	146
D3.3.Complete listing of affinities for intersubunit sites in the inner leaflet.	147
D3.4.Complete listing of affinities for M4 sites in the inner leaflet. . . .	148
D4.1.Table SI Parameters used for calculating density threshold affinities for intersubunit sites in the outer leaflet.	149

D4.2.Table SI Parameters used for calculating density threshold affinities for M4 sites in the outer leaflet.	149
D4.3.Table SI Parameters used for calculating density threshold affinities for intersubunit sites in the inner leaflet.	149
D4.4.Table SI Parameters used for calculating density threshold affinities for M4 in the inner leaflet.	149

List of Figures

1.1.	Protein structure of the nicotinic acetylcholine receptor and Erwinia ligand-gated ion channel.	3
1.2.	Domain formation in model PUFA rich domain forming membranes.	6
2.1.	nAChR boundary lipids in binary mixtures of DPPC and CHOL.	21
2.2.	Quantitative analysis of bulk membrane mixing and nAChR boundary lipid composition across small membranes containing DPPC, Cholesterol, and either dDHA-PE or dLA-PC.	23
2.3.	Trajectories of ternary mixtures at ratios of 2:2:1 DPPC:PUFA:Chol.	24
2.4.	Comparison of nAChR partitioning based on lipid headgroups (PC and PE).	25
2.5.	Lipid density enrichment or depletion around a single central nAChR.	30
2.6.	Embedded lipids in the nAChR.	31
3.1.	Nicotinic acetylcholine receptor (nAChR) structure	40
3.2.	Protein clustering in domain-forming (top row) and hybrid (bottom row) membranes.	46
3.3.	Distribution of nAChR boundary cholesterol or acyl chain fractions in mixed membranes containing homoacidic phospholipids.	49
3.4.	Distribution of nAChR boundary cholesterol or acyl chain fractions in mixed membranes containing heteroacidic phospholipids.	50
3.5.	Enrichment or depletion of lipid species surrounding a single nAChR.	51
3.6.	Pairwise distance distribution across multi-protein systems.	53
3.7.	Subunit pairs among dimerizing proteins.	55

4.1. POPG binds selectively to ELIC.	62
4.2. Enrichment of POPG among ELIC boundary phospholipids from coarse-grained simulations.	64
4.3. ELIC WT channel properties in giant liposomes composed of varying mole% POPG (n=3-5, \pm SD).	69
4.4. POPG selectively thermally stabilizes ELIC and decreases ELIC desensitization.	70
4.5. POPG selectively thermally stabilizes ELIC and decreases ELIC desensitization.	71
4.6. Mutations of five interfacial arginines reduce POPG binding. . . .	72
4.7. Density calculations of lipids in binary membranes and visualization of direct POPG-ELIC interactions at 10% POPG.	74
4.8. The effect of ELIC mutants on desensitization.	77
4.9. ELIC WT and mutant channel properties in giant liposomes composed of 25 mole% POPG (n=3-7, \pm SD).	79
4.10. The L240A mutant decreases desensitization and increases POPG binding.	81
4.11. Arginines involved in POPG binding and ELIC desensitization. . .	82
5.1. Binding site boundaries and distribution definitions.	109
5.2. A molecular perspective of coarse-grained simulation results . .	113
5.3. Lipid density enrichment around a central singular nAChR. . .	114
5.4. Density-threshold affinities organized to reveal site selectivity. .	115
5.5. Density-threshold affinities organized to reveal lipid preferences by site.	119
5.6. Cartoon of expected boundary lipids for the nAChR in a native membrane for both leaflets.	124

A1. nAChR as a model pLGIC structure and pLGICs in PUFA rich model domain forming membranes.	129
B1. Membrane domain formation and protein domain partitioning in small membranes.	131
B2. Alternate view of membrane from Figure 2.3A.	132
C1. MS1 spectra of lipid extract from purified ELIC in DDM and <i>E. coli</i> membranes.	135
C2. Representative deconvoluted spectra of 1 μ M ELIC in C10E5 with increasing concentration of POPG. Dashed line indicates mass of apo ELIC.	135
C3. Comparison of lipid binding at different charge states.	136
C4.	137
C4. Lipid binding data fit to binomial distributions.	138
C5. Relationship of the thermal stabilizing effect of POPG	138
C6. Channel properties of WT ELIC responses to cysteamine.	139
C7. Channel properties of ELIC WT and mutant responses to cysteamine in giant liposomes of 25 mole% POPG.	140
D1. Probability distributions of acyl-chain saturations, including cholesterol, and head group charge.	141
D2. Charged amino acids in or near the TMD of two pLGICs and corresponding anionic enrichment.	143

Chapter 1

Introduction

1.1 Pentameric Ligand-Gated Ion Channels

Ion channels are transmembrane proteins that passively transport ions across membranes. Pentameric ligand-gated ion channels (pLGICs) are ion channels made of five subunits and gated by various neurotransmitters, such as acetylcholine, glycine, gamma-aminobutyric acid, and serotonin. pLGICs are modulated by numerous drugs, such as alcohol [216] or nicotine [57], and anesthetics like propofol [63, 1], endogenous molecules like lipids [84, 185] and thyroid hormones [249, 181]. Mammalian pLGICs are essential proteins dedicated to neuronal function and are found in both the central and peripheral nervous system. pLGICs play various roles in neurological diseases related to inflammation [238, 74, 195, 258, 95], addiction [74], chronic pain [253], Alzheimer’s Disease [245, 201, 69, 138], spinal muscular atrophy [11], schizophrenia [120, 138] and neurological autoimmune diseases [154, 147].

pLGICs are found throughout the animal kingdom [132]. There are two categories of pLGICs: cationic and anionic. Cationic pLGICs, such as nicotinic acetylcholine receptors (nAChRs) and serotonin receptors (5-HT₃Rs), are responsible for stimulating action potential along axons. Anionic pLGICs, such as γ -aminobutyric acid type A receptors (GABA_ARs), and glycine receptors (GlyRs) are responsible for inhibiting action potentials.

Mammalian pLGICs contain three major domains: the extra-cellular domain (ECD), the transmembrane domain (TMD), and the poorly characterized inter-cellular domain (ICD), see Figure 1.1. The ECD is composed of beta-sheets,

with ligand binding pockets at the inter-subunit regions. The TMD spans the membrane. Each TMD contains four alpha-helices, M1 to M4. Alpha-helices M1 and M3 form the "body" of the TMD, M2 makes up the channel's pore, and M4 is exposed to the membrane and is in direct contact with lipids.

pLGIC function is modulated by the membrane lipid composition [214, 75, 66]. pLGIC-lipid interactions have been studied for more than 40 years, however the modulatory mechanism remains unclear [97, 218, 86, 236, 62, 231, 214, 150, 73]. One of the most well studied pLGICs is nAChR. When nAChRs are reconstituted in model membranes (synthetic membranes of 1 to 3 lipids) a minimum of 10–20% cholesterol is required to restore native function to the channel. Anionic phospholipids, with cholesterol, have also been shown to stabilize nAChR under very specific conditions [96, 103, 102, 135, 236, 82, 119, 83]. Yet it is not known where these lipids bind, with what affinity, or how they affect channel conformation.

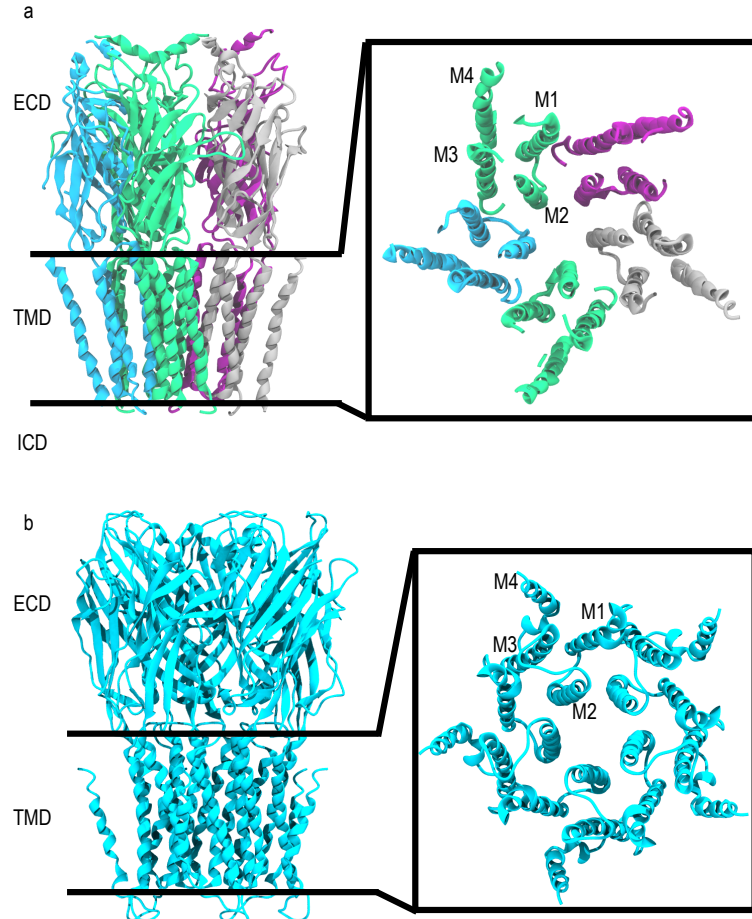


Figure 1.1: Protein structure of the nicotinic acetylcholine receptor and Erwinia ligand-gated ion channel. Visualization of the a) neuronal nicotinic acetylcholine receptor (nAChR) [242] and b) Erwinia ligand-gated ion channel (ELIC). Left: Structure shown from a side view. ECD is comprised of beta sheets. TMD are alpha helices. The ICD is disordered and not shown. nAChR colored: α : green, γ : blue, δ : grey, β : purple. ELIC colored in cyan. Right: The TMD looking down from the ECD. M4 directly interact with lipids, and provide the conical/star shape. M1 and M3 make up a cylindrical “body” of the channel. M2 lies the central pore.

1.2 Lipids and Membranes

Lipids are a wide class of small amphiphilic molecules used biologically as signaling molecules [114, 223], protein modulators [84, 185], and essential component of membranes [257]. Two sub-lipid groupings are phospholipids and sterols [51, 228, 226, 50, 257]. Phospholipids are molecular structures consisting of a zwitterionic head groups, like phosphatidylcholine, or charged head groups, like phosphoserine, a glycerol- or sphingosine-back bone, and two fatty acid hydrocarbon chains (acyl-chains) which vary in both length and saturation. Saturated acyl-chains, such as the medium length palmitic acid(C16:0), add order to the overall membrane. Unsaturated acyl-chains decrease overall membrane order and increase membrane permeability. Unsaturated acyl-chains can be monounsaturated (a single kink caused by a double bond) like Oleic acid (18:1), or polyunsaturated (multiple kinks caused by multiple double bonds). The quintessential polyunsaturated fatty acid (PUFA) is the n-3 PUFA docosahexaenoic acid (C22:6) (DHA). DHA plays a number of roles in membrane organization [234, 107], and neurological disorders [114, 89, 163, 174].

Sterols are a group of small rigid molecules with small neutral head groups and short rigid tails. Sterols are found throughout bacteria (hopanoids) [191], plants (phytosterols) [180], fungi (ergosterol)[221], and animals (cholesterol). Cholesterol is essential to hormone synthesis and signaling [50]. In membranes, it decreases membrane permeability and the average area per lipid and adds order to the bulk membrane [256]. Cholesterol is also an essential lipid to restore function to nAChR when reconstituted into model membranes.

Model membranes often contain cholesterol, saturated, and monounsaturated lipids, with neutral or anionic head groups. Synthesizing model membranes with cholesterol and homo-acidic saturated and unsaturated lipids can result in lipid domain formation. Domain formation is the de-mixing of ordered saturated lipids

and cholesterol from less ordered unsaturated lipids, forming liquid ordered (l_o) and liquid disordered (l_{do}) domains respectively[137, 158], see Figure 1.2. Domain formation, which requires spatial separation of saturated and unsaturated chains, is possible for mixtures of homo-acidic lipids, but not for hetero-acidic lipids containing both a saturated and unsaturated chain. Hetero-acidic lipids are more common in native membranes [78, 45, 18, 237, 208, 128, 160], so it is likely that well-defined domains are less common in such membranes. Model membranes are useful tools for developing predictive models, but they lack the lipid diversity and the physical traits of realistic membranes.

The native membrane of model organisms such as *Xenopus* oocytes may have more than thirty phospholipid species [106, 100] compared to the handful in model membranes. pLGIC native membranes, such as neuronal membranes or *Torpedo* electric organs have more than 30 species of phospholipid [78, 237, 45, 128, 18, 208]. When nAChR is studied in *Xenopus* oocytes, its current is reduced from native values but can be restored with lipid additives, such as asolectin [211] to conduct ions. This suggests lipid diversity is not sufficient for native function, and that there are specific lipids required for nAChR function not found in *Xenopus* oocytes or (not enough of these specific lipids to play a boundary role).

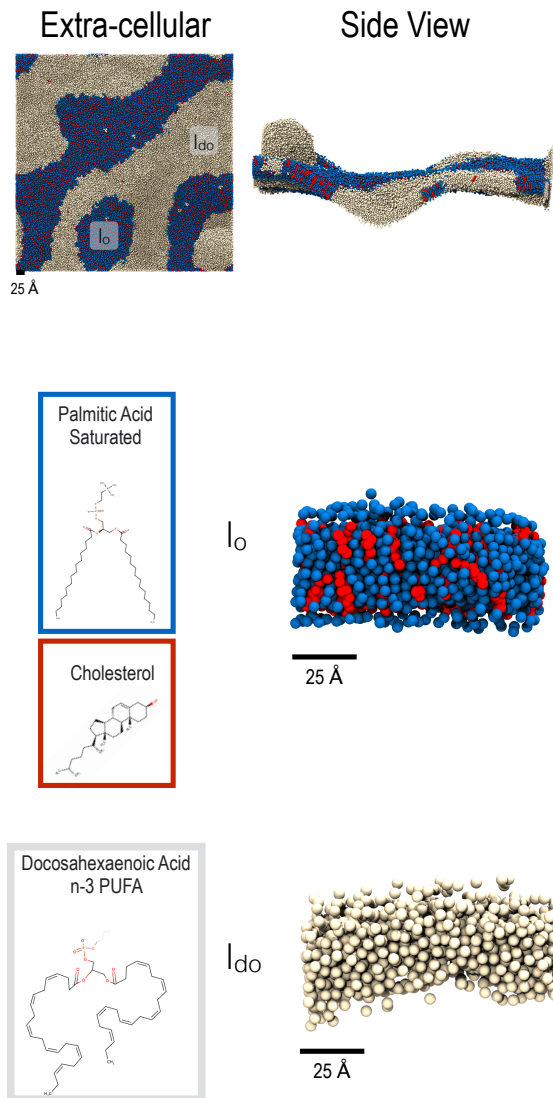


Figure 1.2: Domain formation in model PUFA rich domain forming membranes
 Membranes are $75 \times 75 \text{ nm}^2$ of 40:40:20 of n-3 PUFA:saturated:cholesterol, cream, blue, and white respectively. Row one shows the membrane from the extra-cellular domain and a side view. Row two shows a segment of a l_o domain. Row three shows a segment of a l_{do} domain.

1.3 Boundary Lipids

Boundary lipids are lipids in direct contact with a protein's TMD. In random mixtures, the boundary lipid distribution would reflect the bulk distribution,

but there is significant evidence that specific binding of lipids plays a key role in channel function. The most well studied pLGIC, nAChR, is functionally dependent on cholesterol and anionic lipids [86, 96, 80, 103, 102, 134, 236, 82], and many of these studies have demonstrated a role for direct interactions. Yet the precise location of lipid binding sites for pLGICs are still relatively unknown. Structural biology has detected cholesterol and fatty acid binding sites in pLGICs [3, 6, 150, 24, 122]. Brannigan et al 2008 [41] demonstrate cholesterol embedded within nAChR helped stabilize the protein's structure. Similarly Cheng et al 2009 [65] showed both cholesterol and anionic lipids with small head groups like phosphatidic acid (PA) could bind non-annularly to neuronal $\alpha 4\beta 2$ nAChR, and the anionic head group stabilizes the ECD during gating.

The M4 alpha helices have been shown to play a role in lipid sensing [121]. Basak et al [24] found DHA bound around the M4 region in GLIC. DHA is a highly flexible PUFA, and if it binds to M4 it may play a role in minimizing membrane deformation caused by M4.

pLGICs are structurally similar and it is likely that the distribution of acyl-chains and cholesterol is related across pLGIC sequences. Differences in pLGIC sequences may result in variation of charged lipid distribution. nAChR and GABA_AR have positive amino acids in the lower portion of their M4 alpha helices, while ELIC has positive amino acids at inter-subunit sites, see Figures D2. When boundary lipid requirements are not met, either by a complete absence or too few necessary lipid species, it is likely pLGICs will not maintain native current.

1.4 Approaches to Determining pLGIC Boundary Lipids

It is experimentally challenging to capture the boundary lipid composition and distribution for membrane channels. By nature lipids are small fluid molecules. Structural biology techniques such as cryogenic electron microscopy (cryo-EM)

and X-ray crystallography can demonstrate where lipids are binding [146, 122] but not the probability of lipid binding. Furthermore, determining which lipids have bound can be challenging as cryo-EM and x-ray crystallography require frozen or “solid” structures to image. Due to lipid’s fluid nature and multiple conformations, lipids introduce significant crystallographic disorder, which prevents identification lipid of species.

Mass spectrometry (MS) can be used to determine boundary lipid composition, including how many of a specific lipid reside around a protein. MS is not an imaging technique and can not provide protein structure or conformation information. Like cryo-EM and x-ray crystallography, MS cannot provide functional information [161].

Functional experiments, such as electrophysiology and fluorescence quenching, can predict lipid modulated function by varying the membrane lipid concentration [81]. However functional experiments cannot directly show if the lipids used affect the protein from the bulk, or from specific region of the protein. Mutagenesis may provide indirect information but is not straightforward to interpret.

MD simulations are an optimal approach to predicting protein boundary lipids. MD is inherently fluid with molecular resolution. Using crystal and cryo-EM structures embedded in membranes based on model or realistic membrane compositions, MD simulations can be used to visualize lipids occupying potential binding sites. Furthermore the ability to visualize protein-lipid interaction allows straight forward prediction of the interactions driving lipid binding. While not necessarily useful for predicting how lipids modulate protein function, MD can be run using open, closed, and desensitized states of channel proteins to track changes in the structural role lipids play.

MD comes in multiple forms, though two of the most widely used are all atomistic (AA) and coarse grained (CG). AAMD, modeled using all the atoms in a molecule, is limited by the molecular complexity, system size, and a time

step on the ~ 2 fs scale. Tracking lipid diffusion from the bulk to the protein is computationally expensive and not always a viable approach. CGMD reduces the resolution of a molecule, for instance, the MARTINI forcefield [168] combines ~ 4 atoms into a single bead. The reduced resolution allows for complex and large scale molecular systems at relatively larger time step (~ 10 fs scale), allowing lipids to diffuse from the bulk to a channel and back. This makes CGMD a powerful technique for predicting boundary lipids, membrane deformation, and protein-protein interactions within a membrane.

1.5 Goals of this Thesis

This thesis aims to identify specific lipid binding sites on pLGICs, as well as the effect of lipid topology and bulk membrane composition on occupancy of these sites. CGMD has been used for various small proteins in model to realistic membranes [127, 92, 194, 101, 157] but pLGICs had solely been simulated using AAMD in model membranes lacking many essential native lipids. AAMD simulations provide critical predictions of how lipids bind to specific sites around pLGICs and can predict how lipid are structurally important to proteins. CGMD allows complex lipid compositions to diffuse around one or more pLGICs and equilibrate to the most likely 1) boundary composition and 2) lipid distribution. Over four chapters, I will quantify the boundary lipids of pLGICs in a series of increasingly complex membranes, beginning with a simple model membrane and culminating in a quasi-native neuronal membrane.

Chapter 2 demonstrates neuromuscular nAChR-lipid [242] interaction in model PUFA rich domain forming membranes. I examine protein-membrane domain partitioning, boundary lipid distributions and present a potential explanation for PUFA- and cholesterol-nAChR interactions. Chapters 3 and 4 predict specific lipid occupancy sites around the TMD for lipid acyl-chain saturation and

head group charge. Chapter 3 expands on the work of chapter 2, comparing nAChR boundary lipid distributions in PUFA rich model membranes with and without domain formation. Chapter 4 does not consider PUFAs and focuses on the distribution of anionic lipids around ELIC [193] embedded in binary non-domain forming membranes. Chapter 5 unifies the elements of the previous chapters. Unlike the previous model membranes, we use a quasi-neuronal membrane of 36 different lipid species with both neutral and anionic head groups [128]. We determine boundary lipid distributions for nAChR, quantify specific binding using a new affinity calculation method, and compare to results from model membranes in chapters 2 to 4.

Chapter 2

Boundary lipids of the nicotinic acetylcholine receptor: spontaneous partitioning via coarse-grained molecular dynamics simulation

Originally published in: Biochimica et Biophysica Acta - Biomembranes, 2019,
vol. 1861, issue 4, pages 887-896

Liam Sharp¹ Reza Salari^{1,2} Grace Brannigan^{1,3} 1) Center for Computational and Integrative Biology, Rutgers University-Camden, Camden, NJ 2) Now at Washington University School of Medicine in St Louis 3) Department of Physics, Rutgers University-Camden, Camden, NJ

2.1 Abstract

Reconstituted nicotinic acetylcholine receptors (nAChRs) exhibit significant gain-of-function upon addition of cholesterol to reconstitution mixtures, and cholesterol affects organization of nAChRs within domain-forming membranes, but whether nAChR partitions to cholesterol-rich liquid-ordered (“raft” or l_o) domains or cholesterol-poor liquid-disordered (l_{do}) domains is unknown. We use coarse-grained molecular dynamics simulations to observe spontaneous interactions of cholesterol, saturated lipids, and polyunsaturated (PUFA) lipids with nAChRs. In binary Dipalmitoylphosphatidylcholine:Cholesterol (DPPC:CHOL) mixtures, both CHOL and DPPC acyl chains were observed spontaneously entering deep “non-annular” cavities in the nAChR TMD, particularly at the subunit interface and the β subunit center, facilitated by the low amino acid density in

the cryo-EM structure of nAChR in a native membrane. Cholesterol was highly enriched in the annulus around the TMD, but this effect extended over (at most) 5-10Å. In domain-forming ternary mixtures containing PUFAs, the presence of a single receptor did not significantly affect the likelihood of domain formation. nAChR partitioned to any cholesterol-poor l_{do} domain that was present, regardless of whether the l_{do} or l_o domain lipids had PC or PE headgroups. Enrichment of PUFAs among boundary lipids was positively correlated with their propensity for demixing from cholesterol-rich phases. Long $n - 3$ chains (tested here with Docosahexaenoic Acid, DHA) were highly enriched in annular and non-annular embedded sites, partially displacing cholesterol and completely displacing DPPC, and occupying sites even deeper within the bundle. Shorter $n - 6$ chains were far less effective at displacing cholesterol from non-annular sites.

2.2 Introduction

The nicotinic acetylcholine receptor (nAChR) is an excitatory pentameric ligand gated ion channel (pLGIC) commonly found in the neuronal post synaptic membrane and neuromuscular junction (NMJ) in mammals as well as the electric organs of the *Torpedo* electric ray. nAChRs play a fundamental role in rapid excitation within the central and peripheral nervous system, and neuronal nAChRs are also critical for cognition and memory [88, 59]. Acetylcholine is the orthosteric nAChR ligand, but numerous other exogenous and endogenous small molecules modulate nAChRs, including nicotine, general anesthetics, the tipped-arrow poison curare, phospholipids, cholesterol, and cholesterol-derived hormones.[142, 238] The larger pLGIC super family that includes nAChRs has been shown to play roles in numerous diseases related to inflammation, [195, 258, 74], addiction [74], chronic pain [253], Alzheimer's Disease [245, 201, 69], spinal muscular atrophy [11], schizophrenia [120] and neurological autoimmune diseases [154].

nAChRs are highly sensitive to the surrounding lipid environment[119, 14, 192, 19] for reasons that remain poorly understood. In the late 1970s it was observed that reconstituted nAChRs only exhibit native conductance if model phospholipid membranes contained at least 10-20% cholesterol [86, 79, 188]. Three generations of investigation into the mechanism have followed, with the first generation of studies[170, 86, 171, 79, 109, 176, 96, 188, 259, 46, 153, 178, 134, 135, 103, 177, 18, 235, 236, 184, 3, 72, 22] aiming to differentiate between the role of bulk, annular, and non-annular cholesterol. The second generation[15, 48, 165, 190, 196, 261, 14, 19, 22, 23, 31, 198, 248, 35, 243] of studies probed membrane-mediated effects on organization of multiple nAChRs, while the third generation[24, 6, 150, 262] has applied x-ray crystallography and high-resolution cryo electron microscopy to directly observe lipid binding modes.

Members of the pLGIC family other than nAChR are also lipid-sensitive,[94, 232, 13, 93] and lipids other than cholesterol can also modulate function[32, 64, 76, 76, 210, 248, 119], but these mechanisms have not been as extensively studied. The recent publication of several crystal and cryo-EM structures [24, 6, 150, 262] has confirmed that specific lipid-pLGIC interactions extend beyond cholesterol and nAChR. Such interactions are also well-established in other transmembrane proteins, including G-protein coupled receptors (GPCRs) and other ion channels, as reviewed in [51, 152, 206, 148, 229].

Even in the specific case of cholesterol-nAChR interactions, results from different approaches have suggested complex behavior and even contradictory interpretations. Results have indicated that both cholesterol enrichment[86, 79, 188] and cholesterol depletion[215] cause gain of function, that anionic phospholipids are unnecessary for native function[86, 79, 188] or must be[76, 85] included in a reconstitution mixture, that cholesterol increases nAChR clustering[196, 261, 19] and directly interacts with nAChR [153, 135], but nAChR does not consistently

partition into cholesterol-rich domains[30]. We suggest here that some of these apparent contradictions may be explained by competition between cholesterol and other lipids found in native membranes, primarily lipids with polyunsaturated fatty acyl chains (PUFAs).

Interactions of nAChR with PUFAs have not been systematically investigated experimentally, but a large amount of circumstantial experimental evidence suggests an important role for PUFAs in nAChR function. Clinically, long-chain $n - 3$ (commonly called “Omega-3” or $\omega - 3$) lipids have a neuroprotective role[202], and nAChR-associated pathologies can arise for patients with low levels of $n - 3$ PUFAs. $\alpha 7$ nAChRs are implicated in schizophrenia[120], and dietary supplementation with $n - 3$ fatty acids (usually through fish oil) can reduce the likelihood of psychosis, with dramatic effects in some individual cases[7].

In vitro, PUFA-rich asolectin[211, 189] is one of the most robust additives[79] for obtaining native nAChR function: restoration of native function by cholestryl hemisuccinate (CHS) is observed only over a narrow CHS concentration range in monounsaturated PE/PS membranes, but a much wider concentration range in asolectin[79]. The specific component(s) of asolectin that complement cholesterol in improving nAChR function have not been isolated. Long chained $n - 3$ PUFA lipids are abundant in two seemingly disparate nAChR native membranes: mammalian neuronal membranes[44, 78] and those of the *Torpedo* electric organ,[18, 208]. Both such membranes also have an abundance of phosphoethanolamine (PE) headgroups and saturated glycerophospholipids, and a scarcity of monounsaturated acyl chains and sphingomyelin compared to the *Xenopus* oocyte membranes [106] common in functional studies, or a “generalized” mammalian cell membrane [129].

Membranes composed of ternary mixtures of saturated lipids, unsaturated lipids, and cholesterol tend to demix into separate domains. Saturated lipids and cholesterol constitute a rigid liquid ordered phase (l_o) in which acyl chains remain

relatively straight. [99, 255, 68, 33] Unsaturated lipids form a more flexible liquid disordered phase (l_{d0}) in which the chains remain fully melted. l_o domains are often visualized as signaling “platforms”, restricting membrane proteins into high density “rafts” that diffuse within a fluid membrane [227, 228]. This conceptualization requires that l_o domains have a much smaller area than l_{d0} domains, and does not well-represent membranes that are over 30% cholesterol, such as neuronal membranes.

The first generation of studies into the mechanism underlying cholesterol-modulation of nAChR were conducted and interpreted in an era preceding the discovery of lipid-induced domain formation in membranes. The second generation explicitly considered potential interactions of nAChR with lipid domains, in part to determine the requirements for the extremely high density ($\sim 10^4 \mu^{-2}$) of nAChRs at the neuromuscular junction [43]. Since direct interaction between nAChR and cholesterol had been demonstrated in the first generation of studies, a sensible initial hypothesis was that nAChR persistently partitioned to l_o domains, retaining little contact with unsaturated chains. Tests of this hypothesis have yielded results that are inconclusive, contradictory, or highly sensitive to lipid composition.

Barrantes and colleagues[248] found that the addition of nAChRs to a domain-forming lipid mixture increased the size of Dipalmitoylphosphatidylcholine/Cholesterol (DPPC/Chol) lipid-ordered domains, which (combined with additional FRET data) was interpreted as indicating nAChR was embedded in liquid-ordered domains. Some studies [165, 233, 250] suggest that nAChRs are associated with microdomains independently of stimulation by other proteins associated with the neuromuscular junction. Other studies[261, 54] suggested that nAChRs require stimulation by a protein such as agrin to partition into microdomains. Formation and disassembly of the nAChR-rich microdomains is highly sensitive to cholesterol concentration.[19, 48, 165, 261, 207]

These studies suggested a role for cholesterol-induced phase separation, but did not confirm that nAChR partitions to the cholesterol-rich phase. To test for an intrinsic nAChR domain preference, Barrantes and co-workers checked for enrichment of nAChRs in the detergent resistant membrane (DRM). nAChRs were not enriched in the DRM of a model, domain-forming mixture (1:1:1 Chol: palmitoyloleylphosphatidylcholine(POPC): sphingomyelin) [30] but inducing compositional asymmetry across leaflets did yield nAChR enrichment in the DRM fraction [198]. While more precise and robust experimental methods for determining partitioning preference and specific boundary lipids such as mass spectrometry have been applied for other transmembrane proteins[115, 67], they have not been applied to complex heteromers like nAChR.

Fully atomistic molecular dynamics (MD) simulations[41, 65, 124, 56] have served as a natural complement to the third-generation structural biology approach, but are limited in their ability to resolve contradictions between first and second generation studies, because lipids are unable to diffuse over simulation time scales.[129, 34, 194, 110, 222]. Efficient lipid diffusion is a requirement for equilibrating domains or detecting protein-induced lipid sorting. Coarse-grained MD (CG-MD) has been used to great success in a number of simulations for both lipid-protein binding and membrane organization [34, 222, 194, 110, 131, 230]. Here we use CG-MD as a “computational microscope” to observe the equilibrium distribution of lipids local to the nAChR in a range of binary and ternary lipid mixtures inspired by native membranes. We observe a remarkable enrichment of polyunsaturated lipids among nAChR boundary lipids. To our knowledge, these are the first molecular simulations of the nAChR in non-randomly mixed membranes, and the first study to systematically investigate the likelihood of polyunsaturated lipids as nAChR boundary lipids.

2.3 Methods

2.3.1 System Composition

All simulations reported here used the coarse-grained MARTINI 2.2[167] topology and forcefield. nAChR coordinates were based on a cryo-EM structure of the $\alpha\beta\gamma\delta$ muscle-type receptor in native torpedo membrane (PDB 2BG9[242]). This is a medium resolution structure (4Å) and was further coarse-grained using the martinize.py script; medium resolution is sufficient for use in coarse-grained simulation, and the native lipid environment of the proteins used to construct 2BG9 is critical for the present study. The secondary, tertiary and quaternary structure in 2BG9 was preserved via soft backbone restraints during simulation as described below, so any inaccuracies in local residue-residue interactions would not cause instability in the global conformation.

Coarse-grained membranes were built using the Martini script insane.py, which was also used to embed the coarse-grained nAChR within the membrane. The insane.py script randomly places lipids throughout the inter- and extra-cellular leaflets, and each simulation presented in this manuscript was built separately. Binary mixed membranes were composed of one saturated lipid species (Dipalmitoylphosphatidylcholine (DPPC) or Dipalmitoylphosphatidylethanolamine (DPPE)) and cholesterol (CHOL), while ternary mixed membranes also included either two $n - 6$ PUFA acyl chains : Dilinoleoylphosphatidylcholine (dLA-PC) or Dilinoleoylphosphatidylethanolamine (dLA-PE) or two $n - 3$ PUFA acyl chains : Didocosahexaenoylphosphatidylethanolamine (dDHA-PE) or Didocosahexaenoylphosphatidylcholine (dDHA-PC). DHA-PC is not distributed with the MARTINI lipidome, but was constructed in-house using MARTINI DHA tails and PC headgroups). Multiple box sizes were used depending on the goal; “small” boxes were between $22 \times 22 \times 20$ nm³ and $25 \times 25 \times 25$ nm³, with about ~ 1400 total lipids and ~ 80000 total beads, and were used primarily to investigate composition

trends, “large” boxes were about $45 \times 45 \times 40$ nm³ with about $\sim 8,300$ total lipids and $\sim 820,000$ total beads, and were used primarily to investigate subunit specificity and long-range sorting, and “very large” boxes were $\sim 75 \times 75 \times 40$ nm³ with about $\sim 19,000$ total lipids and ~ 1.8 million total beads, and were used to verify that partitioning in the l_{do} phase did not reflect finite size effects.

2.3.2 Simulations

Molecular dynamics simulations were carried out using GROMACS[28]; small boxes used GROMACS 5.0.6 and large and very large boxes used GROMACS 5.1.2 or 5.1.4. All systems were run using van der Waals (vdW) and Electrostatics in shifted form with a dielectric constant of $\epsilon_r=15$. vdW cutoff lengths were between 0.9 and 1.2 nm, with electrostatic cutoff length at 1.2 nm.

Energy minimization was performed over 10000 to 21000 steps. Molecular dynamics were run using a time step of 25 fs, as recommended by MARTINI, for 2 μ s for small membranes, and 10 μ s for large and very large membranes. Simulations were conducted in the isothermal-isobaric (NPT) ensemble, by using a Berendsen thermostat set to 323 K with temperature coupling constant set to 1 ps, as well as isotropic pressure coupling with compressibility set to 3×10^{-5} bar⁻¹ and a pressure coupling constant set to 3.0 ps.

Secondary structures restraints consistent with MARTINI recommendations were constructed by the martinize.py [167] script and imposed by Gromacs[28]. Protein conformation was maintained in small systems via harmonic restraint (with a spring constant of 1000 kJ· mol⁻¹) on the position of backbone beads. nAChR conformation in large systems was preserved via harmonic bonds between backbone beads separated by less than 0.5 nm, calculated using the ElNe-Dyn algorithm [199] associated with MARTINI[167] with a coefficient of 900 kJ· mol⁻¹. These restraints limited the root-mean-squared-displacement (RMSD) of the backbone to less than 2.5 Å throughout the simulation.

The minimum equilibration time depended on the system size. Small systems typically began domain formation by 500 ns, with domains fully formed by 1000 ns. Large systems and very large simulations required about 5 μ s of equilibration for stabilization of metrics described below.

2.3.3 Analysis

Extent of domain formation within the membrane was tracked by

$$\begin{aligned} M_{A,B} &\equiv \frac{\langle n_{A,B} \rangle}{6x_B} - 1 \\ M_A &\equiv \frac{\langle n_{A,A} \rangle}{6x_A} - 1 \end{aligned} \quad (2.1)$$

where $n_{A,B}$ is the number of type B molecules among the 6 nearest neighbors for a given type A molecule, the average is over time and all molecules of type A, and the self-association metric is notated $M_A \equiv M_{A,A}$ for brevity. For a random mixture, $\langle n_{A,B} \rangle = 6x_B$, where x_B is the fraction of overall bulk lipids that are of type B. $M_A = 0$ indicates random mixing while $M_A > 0$ and $M_A < 0$ indicate demixing and excessive mixing respectively.

Extent of receptor partitioning within the l_o or l_{do} domain was tracked by counting the number b_{sat} of saturated annular boundary lipids and comparing with the expectation for a random mixture, via the order parameter Q_{sat} :

$$Q_{sat} \equiv \frac{1}{x_{sat}} \left\langle \frac{b_{sat}}{b_{tot}} \right\rangle - 1, \quad (2.2)$$

where b_{tot} is the total number of lipids in the annular boundary region and x_{sat} is the fraction of overall bulk lipids that are saturated phospholipids. $Q_{sat} < 0$ indicates depletion of saturated lipids among boundary lipids, as expected for partitioning into an l_{do} phase, while $Q_{sat} > 0$ indicates enrichment and likely partitioning into an l_o phase. Each frame, b_{tot} and b_{sat} were calculated by counting the number of total and saturated lipids, respectively, for which the phosphate bead fell within a distance of 1.0 nm to 3.5 nm from the M2 helices, projected onto the membrane plane.

Two-dimensional density distribution of the beads within a given lipid species B around the protein was calculated on a polar grid:

$$\rho_B(r_i, \theta_j) = \frac{\langle n_B(r_i, \theta_j) \rangle}{r_i \Delta r \Delta \theta} \quad (2.3)$$

where $r_i = i\Delta r$ is the projected distance of the bin center from the protein center, $\theta_j = j\Delta\theta$ is the polar angle associated with bin j , $\Delta r = 10\text{\AA}$ and $\Delta\theta = \frac{\pi}{15}$ radians are the bin widths in the radial and angular direction respectively, and $\langle n_B(r_i, \theta_j) \rangle$ is the time-averaged number of beads of lipid species B found within the bin centered around radius r_i and polar angle θ_j . In order to determine enrichment or depletion, the normalized density $\tilde{\rho}_B(r_i, \theta_j)$ is calculated by dividing by the approximate expected density of beads of lipid type B in a random mixture, $x_B s_B N_L / \langle L^2 \rangle$, where s_B is the number of beads in one lipid of species B , N_L is the total number of lipids in the system, and $\langle L^2 \rangle$ is the average projected box area:

$$\tilde{\rho}_B(r_i, \theta_j) = \frac{\rho_B(r_i, \theta_j)}{x_B s_B N_L / \langle L^2 \rangle} \quad (2.4)$$

This expression is approximate because it does not correct for the protein footprint or any undulation-induced deviations of the membrane area. The associated corrections are small compared to the membrane area and would shift the expected density for all species equally, without affecting the comparisons we perform here.

2.4 Results

Spontaneous association with cholesterol in binary membranes

Lipid sorting was characterized for nAChRs in binary DPPC:CHOL membranes (Figure 2.1A) using several metrics. Non-random lipid mixing (including domain formation) was quantified using the self-association metric M_A as defined in Equation 2.1. As expected, in simulated binary membranes containing only DPPC and 0-40% cholesterol, minimal demixing was observed, with values of M_{DPPC} (Fig

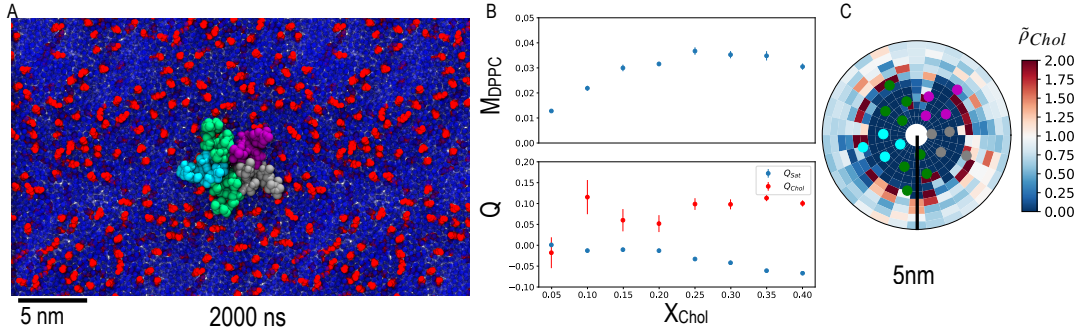


Figure 2.1: nAChR boundary lipids in binary mixtures of DPPC and CHOL. A: Representative frame from a simulated trajectory of a single nAChR embedded in a small membrane, colored by subunit (α :green, β :purple, δ :gray, γ :cyan) in a 4:1 DPPC (blue):Chol (red) mixture. B: Extent of demixing (M_{DPPC} defined in Eq. 2.1) and depletion of saturated lipids from the boundary (Q_{sat} defined in Eq.2.2) in small binary membranes. In this binary system, cholesterol depletion/enrichment is directly related to the saturated lipid depletion/enrichment: $Q_{chol} = -x_{sat}Q_{sat}/x_{Chol}$. Error bars represent standard error for a blocking average over 50 ns. C: Average normalized density (Eq. 5.2) of cholesterol for the system in A. Data is equivalent to that in Figure 2.5: Binary Mixture “Chol” row.

2.1B) rising slightly for higher cholesterol concentrations but remaining persistently below 0.05.

Depletion of saturated lipids among nAChR boundary lipids (relative to those expected for a random mixture) was quantified using the metric Q_{sat} defined in equation 2.2. Negative and positive values of Q_{sat} reflect depletion or enrichment of saturated lipids in the nAChR boundary, respectively. In binary systems containing cholesterol and saturated lipids, depletion of saturated lipids corresponds directly to enrichment of cholesterol: $Q_{chol} = -Q_{sat}x_{sat}/x_{Chol}$.

In binary DPPC:CHOL mixtures, Q_{sat} was very slightly negative for $x_{Chol} <$

20%, but decreased steadily for higher concentrations. This trend indicates some depletion of DPPC (and enrichment of cholesterol) among nAChR boundary lipids (Figure 2.1B). Typically, between 10 and 20% cholesterol has been required in reconstitution mixtures to restore native function [103, 86, 79] and a phase transition at about 20% cholesterol in binary DPPC:CHOL model membranes is indicated by differential scanning calorimetry.[169]

Spontaneous binding of cholesterol to non-annular or “embedded” sites, similar to what we previously proposed[41], was observed in these CG-simulations, and penetration of the TMD bundle by DPPC acyl chains was also observed at lower cholesterol concentrations (Fig 2.1A). Distribution of density for embedded lipids is further discussed in Section 3.4.

Annular cholesterol (enrichment of cholesterol at the protein-lipid interface), is visible for the binary systems via a ring of high (red) cholesterol density just around the protein in Figure 2.1C. Enrichment of cholesterol near the protein is highly localized with a ring that is less than 5 Å wide. This is in general agreement with evidence for annular cholesterol in randomly-mixed binary membranes. [23]

2.4.1 Domains formed in PUFA-containing ternary membranes are not affected by introduction of an nAChR

In order to test whether nAChR affected domain formation in domain-forming membranes, we characterized M_{PUFA} for systems containing DPPC, Cholesterol, and PE or PC with either n-3 (DHA) or n-6 (LA) acyl chains. Addition of phospholipids with unsaturated acyl chains to systems containing a saturated lipid and cholesterol is well-established to induce domain formation, and polyunsaturated phospholipids make these domains more well-defined[155]. As expected, we observed that addition of PUFAs to DPPC/CHOL bilayers did induce domain formation over a range of compositions, and values for M_{PUFA} are shown as filled

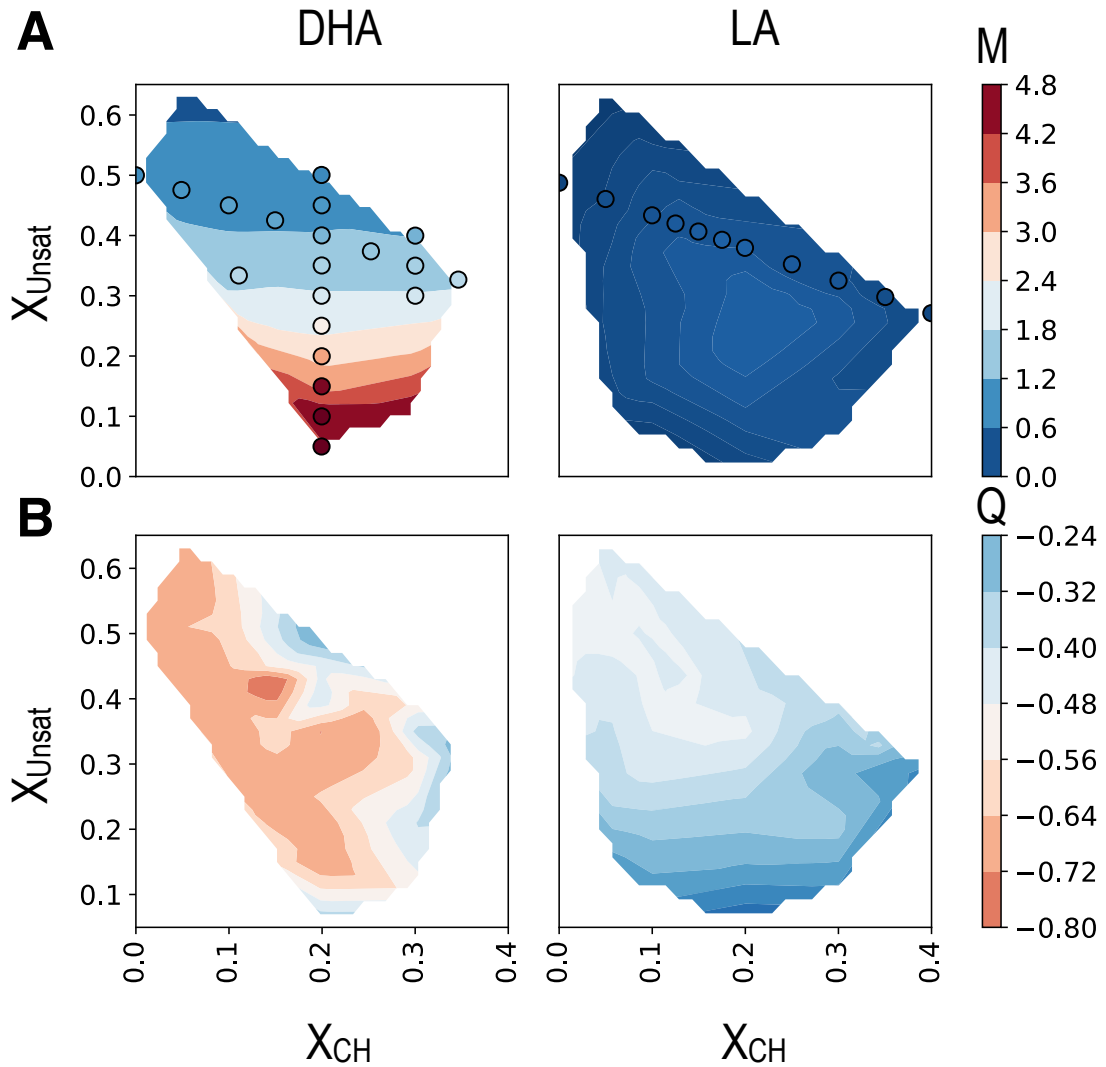


Figure 2.2: Quantitative analysis of bulk membrane mixing and nAChR boundary lipid composition across small membranes containing DPPC, Cholesterol, and either dDHA-PE or dLA-PC. Shaded contours were constructed based on 40 individual simulations with dDHA-PE and 30 with dLA-PC. A: M_{PUFA} , defined in eq 2.1. Circles represent mixing of systems with the same lipid composition but no nAChR. B: Q_{sat} , defined in Eq 2.2.

symbols in Figure 2.2 A.

Introducing a single nAChR to these same systems did not significantly affect

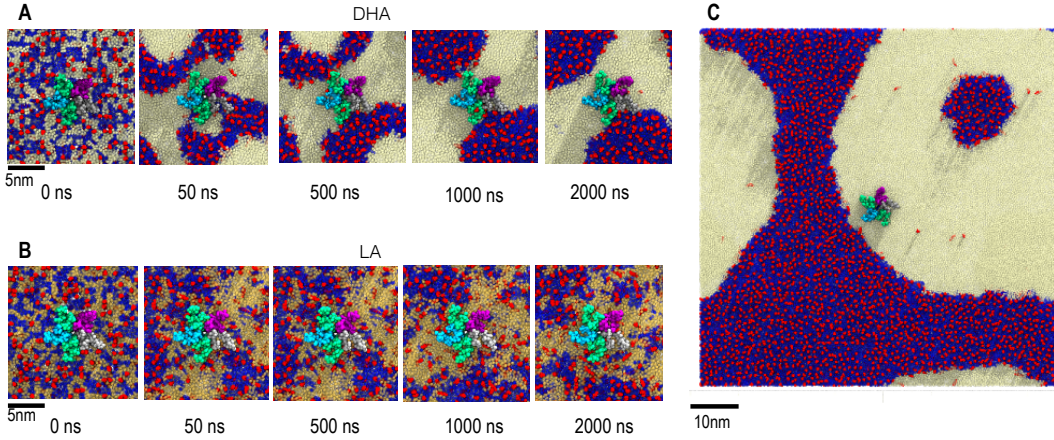


Figure 2.3: Trajectories of ternary mixtures at ratios of 2:2:1 DPPC:PUFA:Chol. A and B: Trajectories of simulation systems with a single nAChR embedded within small membranes, using lipids containing DHA acyl chains or LA acyl chains. Both simulations were run for 2 μ s. C: Final snapshot of 4 μ s trajectory of a system within a large $\sim 75 \times 75$ nm 2 membrane with the same composition as in A. Subunits are colored: α : green, β : purple, δ : gray, γ : cyan. Lipids are colored: Chol: red, DPPC: blue, dDHA-PE: white, dLA-PC: tan.

domain formation. M_{DHA} was determined for an isolated nAChR in ternary mixed membranes with over 40 different combinations of DHA, DPPC, and Cholesterol (Figure 2.2A, shaded contours). Its effect on membrane organization is represented by the difference in color of the circular symbol and the shaded contour at the same composition. Introducing a single nAChR into the DHA-containing systems does slightly reduce the amount of DHA required to obtain a given value of M_{DHA} . This subtle trend may reflect increased likelihood of DHA-DHA interactions due to nucleation of DHA-containing lipids around the protein (Figure 2.3).

Across ternary mixtures with two long $n - 3$ PUFA chains (DHA) and a PE headgroup, maximum values of M_{DHA} approached 5 (Figure 2.2A), and were significantly reduced (to less than 0.5) when DHA chains were replaced with

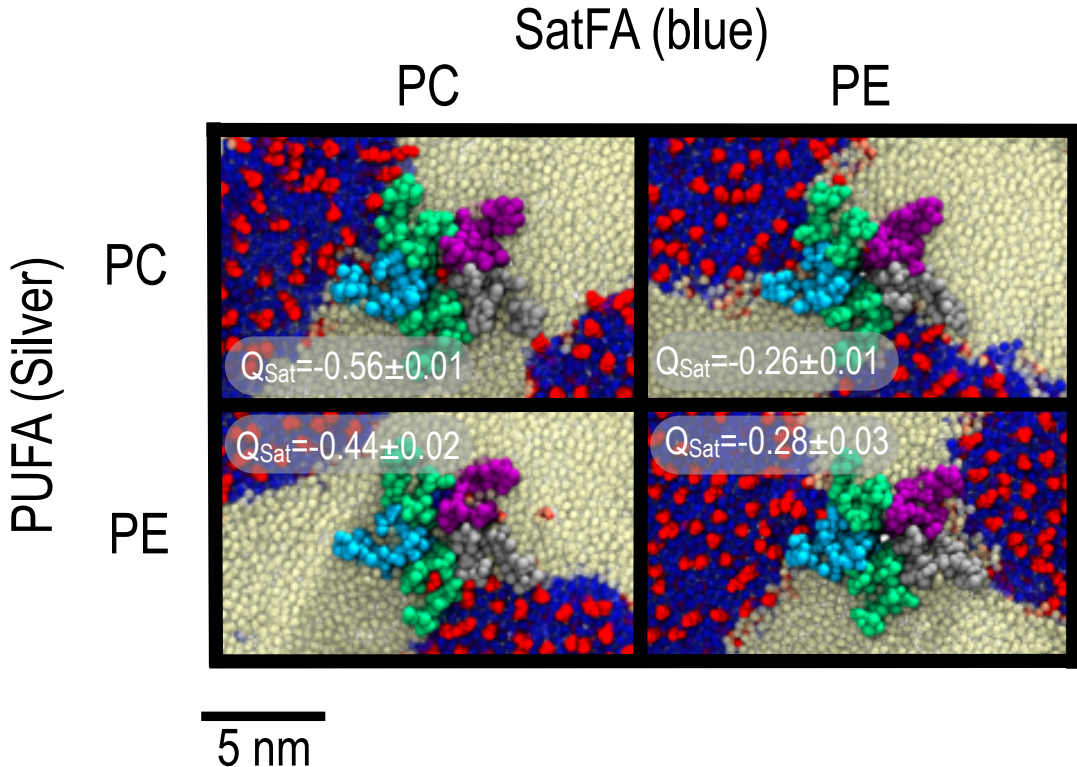


Figure 2.4: Comparison of nAChR partitioning based on lipid headgroups (PC and PE). All images represent last frame of $2\mu\text{s}$ simulations of small membranes with composition 2:2:1 Sat:PUFA:Cholesterol. Rows represent the head-group for the PUFA-containing lipid, while columns represent the head-group of the saturate lipid. Each image includes Q_{sat} values related to individual systems with errors across averaging 50 ns blocks.

linoleic acyl (LA) chains. This result is consistent with a previously-observed significant increase in miscibility temperature upon supplementation of plasma membranes with $n - 3$ lipids. [155]

Substantial lipid demixing in DHA-containing mixtures was observed even at low cholesterol concentrations. Over the range we tested, M_{DHA} was not sensitive to cholesterol concentration x_{Chol} , as shown by the horizontal contours for DHA in Figure 2.2A.

2.4.2 nAChR consistently partitions to the liquid disordered domain

For more than 70 lipid compositions tested, nAChR always partitioned into a PUFA-rich l_{do} phase if such a phase was present. We never observed nAChR partitioning to an l_o phase. Representative frames from trajectories of domain formation in the presence of nAChR are shown in Figure 2.3. This observation includes all tested concentrations of the ternary mixtures, regardless of whether the zwitterionic headgroup was PC or PE (Figure 2.4), or whether DPPC was replaced by dioleoylphosphatidylcholine (DOPC) (di-18:1), Palmitoyloleoylphosphatidylcholine (POPC) (16:0,18:1), or dilauroylphosphatidylcholine (DLPC) (di-14:0), as shown in Figure S1.

These results are quantified for nAChR embedded in ternary membranes containing DPPC, CHOL, and either dDHA-PE or dLA-PC in Figure 2.2 B, using the metric Q_{sat} defined in equation 2.2. In all systems studied here, $Q_{sat} < 0$, indicating depletion of saturated lipids as boundary lipids, consistent with observed partitioning to the l_{do} domain in Figure 2.3. Furthermore, depletion was much stronger in systems containing DHA ($Q_{sat}^{DHA} \ll Q_{sat}^{LA}$), consistent with the more well-defined DHA domains ($M_{DHA} \gg M_{LA}$).

The nAChR annulus is highly enriched in DHA: DHA-PE constitute nearly 100% of the local lipids even in membranes with very low DHA concentrations. This strong signal could indicate multiple high affinity sites for DHA chains across the transmembrane protein surface. At another extreme, DHA enrichment could be driven by a very slight preference for DHA in a highly non-ideal bulk: since DHA is found in well-defined domains without protein, even one DHA molecule that binds to the protein surface could stabilize the rest of the l_{do} domain nearby. Comparing boundary lipid and domain formation trends can help distinguish between these two scenarios. If boundary lipid enrichment is determined purely by

how well-defined domains are (the latter scenario), we would expect similar trends for M_{DHA} and Q_{sat} in the DHA column of Figure 2.2. In contrast, Figure 2.2 shows that while domain formation in DHA-containing systems is only weakly sensitive to cholesterol content (horizontal contours), composition of boundary lipids is highly sensitive to cholesterol content (diagonal contours). These results suggest that direct interactions between multiple favorable sites on nAChR and DHA-containing lipids dominate the observed enrichment of DHA among boundary lipids.

The simulations represented in Figure 2.2 do compare the effects of two unsaturated lipids that also have different headgroups. DHA is far more commonly paired with PE in native membranes, while LA is more commonly found with PC. We found no qualitative differences in nAChR domain partitioning or significant quantitative effect on Q_{sat} upon switching PC and PE headgroups on the PUFA lipid. We did observe a quantitative effect of *saturated* lipid headgroup on boundary lipid composition: Q_{sat} was reduced by half when saturated PE was used instead of saturated PC. (Figure 2.4). As shown in Figure 2.4, nAChR is bordered by l_o domains on two opposing faces when saturated PE is used, compared to only one face if PC is used. The particular domain topology shown in Figure 2.4 is an artifact of the periodic boundary conditions, but still indicates more favorable interactions of nAChR with an l_o domain composed of DPPE vs DPPC. This may reflect a difference in the lipid shape (wedge-shaped DPPE vs cylindrical-shaped DPPC) and the associated monolayer spontaneous curvature. For PUFA lipids in flexible l_{do} domains, lipid shape is less likely to play a significant role in determining partitioning. The dramatic difference in domain flexibility is apparent in Figure B2.

2.4.3 Spontaneous integration of lipids into nAChR TMD bundle

The nAChR structure used for these simulations was determined in a native membrane with a high fraction of polyunsaturated lipids. While we previously [41] proposed that unresolved density in this structure could be embedded cholesterol, the possibility of occupation by phospholipids other than POPC was not investigated. Furthermore, we did not consider possible asymmetry across subunits in binding previously. Here we do observe penetration of both the intersubunit (“type B”) and the intrasubunit (“type A/C”) sites previously proposed[41], by both phospholipids and cholesterol, but with a high degree of subunit specificity.

Two dimensional density distributions of DPPC, PUFAs, and cholesterol over short and long length scales were measured for two ternary mixtures and one binary mixture (Figure 2.5). In binary DPPC/cholesterol membranes, DPPC was more likely than cholesterol to occupy intrasubunit sites. DPPC binds shallowly in the α subunit and more deeply in the β subunit. Introducing PUFAs resulted in displacement of both cholesterol and DPPC from intrasubunit sites, except for the β intrasubunit site, which became more likely to be occupied by cholesterol. The interior of the β subunit TMD has the largest amount of available volume, could sequester cholesterol (but not DPPC) from the PUFA lipids in the annulus, and filling the interior with a PUFA chain may be entropically costly. PUFA chains did occupy other intrasubunit sites, but remained fluid, as shown in Figure 5.6.

Intersubunit sites were rarely occupied by DPPC, with the exception of the $\beta+$ $/\alpha-$ site in the binary system (Figure 2.5). Intersubunit sites were more likely to bind cholesterol, particularly the $\beta+/ \alpha-$, $\alpha+/ \gamma-$, and $\alpha+/ \delta-$ subunit interfaces. Occupation of the $\alpha+/ \delta-$ interface is consistent with cryo-EM observations[243] of enhanced cholesterol density around the $\alpha+/ \delta-$ site. Intersubunit sites that were not significantly occupied by cholesterol ($\delta+/ \beta-$ and $\gamma-/ \alpha+$) did show

significant and deep occupation by DHA, which tended to enter from the adjacent intrasubunit site rather than from the membrane. Even those intersubunit sites with significant cholesterol occupancy can simultaneously bind part of a DHA chain, yielding non-vanishing DHA density.

2.4.4 Lipid sorting over the 5-20 nm range is associated with larger domains

We also calculated density distributions of each lipid species at distances beyond the “annular” ring, over the 5-20 nm range. As shown in Figure 2.5 (left column), observed sorting of lipids within 5-20 nm of the nAChR is dependent on the overall composition of the membrane. For all compositions shown, cholesterol is depleted within 5-20 nm and enriched even farther from the protein. Within the binary systems this effect is minor ($\tilde{\rho}_{CHOL} \sim 1$), but it becomes stronger in the moderately demixed LA systems ($\tilde{\rho}_{CHOL} \sim 0.5$) and substantial ($\tilde{\rho}_{CHOL} \sim 0.25$) for the highly-segregated DHA containing systems. A similar pattern is observed for DPPC, which suggests that “sorting” over the 5-20 nm range is primarily driven by intrinsic differences in membrane organization that would be observed without the receptor. PUFAs are also most highly enriched at intermediate distances : the deepest red band is found at about 5 nm in LA-containing systems and about 8 nm in DHA-containing systems. This would be expected when nAChR partitions near a curved domain boundary, as in Figure 2.4.

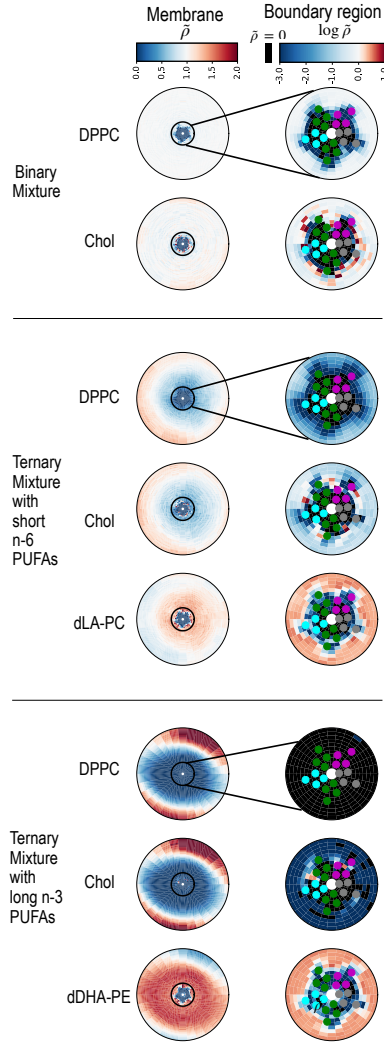


Figure 2.5: Lipid density enrichment or depletion around a single central nAChR. Heatmaps are colored according to the normalized density $\tilde{\rho}_a$ (left, defined in eq 5.2) or $\ln \tilde{\rho}_a$ (right), averaged over the final $5\mu s$ of a $10\mu s$ simulation. Membrane column (left) depicts density across the simulated membrane; $\tilde{\rho}_a < 1$ indicates depletion compared to a random mixture, while $\tilde{\rho}_a > 1$ indicates enrichment. Boundary column (right) shows a zoomed-in region around the protein, with circles corresponding to average position of the protein helices, colored as in Figure 2.1, and black indicating no detected lipid density. If no non-annular or embedded lipid binding was observed, the entire protein footprint would be black for all lipids. Binary mixture contains 4:1 DPPC:CHOL as in Figure 2.1, while both ternary mixtures contain 2:2:1 DPPC:PUFA:Chol.

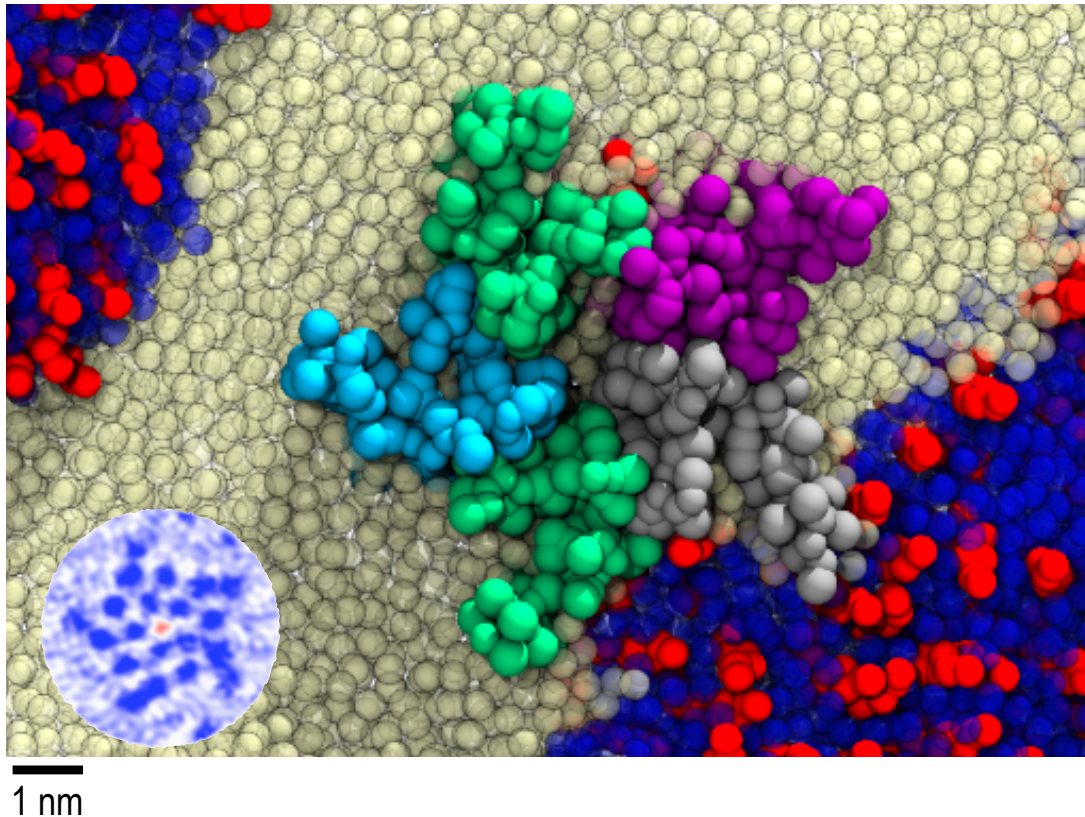


Figure 2.6: Embedded lipids in the nAChR. Main image: Representative frame from equilibrated small membrane simulation of nAChR in 2:2:1 DPPC:DHA-PE:CHOL. Backbone beads of the TMD helices are colored by subunit as in Figure 2.2; side-chain beads are not shown. Both DHA-PE (white) and cholesterol (red) equilibrate to embedded sites in the subunit center and subunit interfaces, although most cholesterol is found in the l_o phase with DPPC (blue). Inset : Cryo-EM density of nAChR from [179] as rendered in [41]; dark blue indicates high density, white is medium density, and red is low density.

2.5 Discussion

In this work we used coarse-grained simulations to predict the local lipid composition around the nicotinic acetylcholine receptor, in a range of domain forming membranes. We observed nAChR partitioning to the liquid-disordered phase in all systems for which such a phase was present. This is inconsistent with the model of lipid rafts as platforms that contain a high density of nAChRs, and unexpected in light of the established cholesterol dependence of nAChR. As shown in these simulations, partitioning to the l_{do} phase does not prevent nAChR from accessing cholesterol.

The simulations presented here involve only one receptor per system. Using the present results only, the simplest extrapolation to multiple receptors would assume that receptors are simply distributed randomly across the l_{do} domain. The local receptor area density would be the number of receptors divided by the total area of l_{do} domains.

In the model membranes used here, as well as in native nAChR membranes, the lipid composition would be expected to yield l_{do} phases that were about the same size as l_{o} phases. The l_{o} “raft” in an l_{do} “sea” analogy is not representative when over 50% of the membrane is in the “raft” phase. A more representative analogy would be receptors as boats, floating on an l_{do} lake within an l_{o} rigid land mass. Filling in the lake by adding to the coastline would force any boats in the lake closer together. Similarly, any process that decreased total l_{do} area while keeping the number of receptors constant would increase the local receptor density. In this model, observing increased nAChR density by adding membrane cholesterol (as in [22, 21, 48, 165, 190, 196, 261, 19, 248, 35]) would be consistent with nAChR partitioning to the cholesterol-poor phase rather than the cholesterol-rich phase.

This extrapolation from a single receptor assumes that introduction of additional receptors does not change partitioning behavior. We do still find reliable partitioning to the l_{do} phase upon adding more receptors, and we will characterize systems with multiple receptors in a future publication. Due to receptor dimerization and trimerization, distribution of individual receptors within the l_{do} phase will not be random. This would not change the expected trend of density increasing with added cholesterol, however. This interpretation also assumes that cholesterol is randomly mixed within the l_o phase, while results from atomistic simulations[230, 131] have suggested that cholesterol may preferentially partition to the boundary between l_o phases and l_{do} phases composed of monounsaturated lipids. Similar studies in which the l_{do} domain is composed of PUFAAs and the interface is much more compact have not been reported. In the present coarse-grained simulations, we did observe random mixing of cholesterol within l_o phases, rather than at the boundary with the PUFA-rich l_{do} phase.

Observed partitioning into the l_{do} phase could be considered inconsistent with interpretations of some experiments, [30, 198] which suggest minimal nAChR partitioning preference in symmetric model membranes or an actual preference for an l_o phase in asymmetric model membranes. These experiments used only monounsaturated acyl chains, and may have had less well-defined domains. They further relied on detergent resistant membrane (DRM) methods, which are sensitive to the choice of detergent [47] and could be unable to distinguish between proteins with no partitioning preference vs proteins that persistently partition to one side of a boundary.

The origin of preferential partitioning observed in these simulations for the l_{do} domain is still unclear, but may reflect different elastic properties of the l_{do} and l_o domains. In general, proteins embedded in membranes will introduce a boundary condition on the membrane shape, such that (1) the thickness of the membrane matches the thickness of the transmembrane domain[10, 133, 39]

and (2) interfacial lipids are parallel to the protein surface.[113]. Transmembrane proteins with hydrophobic mismatch with the surrounding membrane may deform the membrane thickness to satisfy constraint (1), while cone-shaped proteins like pLGICs must also introduce a “tilt” deformation to satisfy (2). Each leaflet of the membrane has an elastic resistance to bending away from its spontaneous curvature, and satisfying these constraints is energetically costly.

Continuum theories based on the Helfrich Hamiltonian have been used to predict shape deformations around protein inclusions in homogeneous membranes [113, 10, 38]. In mixed membranes, minimization of the protein-deformation free energy may also induce lipid sorting. Two distinct sorting mechanisms could minimize the bending free energy: sorting that A) reduces the required bending deformation, by selecting boundary lipids with a specific thickness, leaflet asymmetry, or shape or B) reduces the free energy cost of the bending deformation, by selecting for flexible boundary lipids. Mechanism (B) is the most generally applicable approach, and would stabilize partitioning to the most flexible domains, consistent with our observations (Figure B2). In some cases, mechanism (A) may also contribute to partitioning or lipid-sorting, and could explain why nAChR tends to attract saturated PE over saturated PC, or how leaflet asymmetry can promote partitioning to more rigid phases as observed in [198] .

We previously [41] proposed unresolved density in the cryo-EM structure of nAChR in the *Torpedo* membrane could be embedded cholesterol, based on gain of function caused by cholesterol in reconstitution mixtures[103, 235, 118, 53, 32, 102, 25, 85], but we did not consider the possibility of occupation by polyunsaturated chains. Here we observe spontaneous binding of cholesterol to coarse-grained embedded sites, but long-chain PUFA tails displace cholesterol in some binding sites. Long acyl chains may penetrate far into the TMD bundle without requiring the entire head group also be incorporated, and long-chain PUFAs may do

so without as substantial an entropic penalty as long saturated chains. Cholesterol (like phosphatidic acid, another lipid known to cause gain of function under some preparations[53, 32, 102, 26, 85]) has a much smaller headgroup than PC or PE. It can become fully incorporated into the TMD without the TMD needing to accommodate the bulky headgroup. These complex associations underlie the challenges of predicting local lipid environment in heterogeneous, highly non-ideal mixtures.

All simulations reported here contain lipids with di-saturated tails or di-PUFA tails. While lipid species with two identical acyl chains do exist in the native membrane, they are far less common than hybrid lipids with heterogeneous acyl chains. Including hybrid lipids would reduce the potential for formation of large domains, while increasing the length of the domain interface. Incorporation of hybrid lipids would also reduce the nAChR-local concentration of PUFA chains. Even 5-10% DHA is a saturating concentration for nAChR cavities, however, so we expect occupation of cavities to be minimally affected by replacement of di-DHA lipids with twice the number of hybrid lipids.

None of the three generations of experimental studies into the effects of cholesterol and lipid headgroup on nAChR function have systematically considered the effects of lipid polyunsaturation. We predict that first-generation-style functional studies would find that nAChRs reconstituted in model membranes are sensitive to replacement of even a small fraction of saturated or mono/diunsaturated acyl chains with $n = 6$ and (especially) $n = 3$ PUFAs. Within domain forming membranes common to second-generation studies, systematically varying polyunsaturation and phospholipid topology could help untangle the effect of direct interactions vs organization, as we discussed in [37]. Third-generation structural biology techniques are the most promising approaches for detecting subunit-specific interactions. While it is unlikely that polyunsaturated acyl chains could be resolved, lipids could be chosen such that particular chains also had a unique and

resolvable headgroups. In general, modular lipid topology allows for numerous strategically-designed experiments to isolate the role of head-group versus acyl chain in determining boundary lipids.

Chapter 3

Untangling direct and domain-mediated interactions between nicotinic acetylcholine receptors in DHA-rich membranes

Originally published in: Journal of Membrane Biology, 2019, vol. 252, pages 385-396

Kristen Woods^{*1}, Liam Sharp^{*1}, Grace Brannigan^{1,2} 1) Center for Computational and Integrative Biology, Rutgers University-Camden, Camden, NJ 2) Department of Physics, Rutgers University-Camden, Camden, NJ *These authors contributed equally.

3.1 Abstract

Lipid composition of the membrane can strongly modulate both function and organization of the nicotinic acetylcholine receptor (nAChR). Previously we conducted coarse-grained molecular simulations of a single nAChR from the electric ray *torpedo* in mixed membranes, and observed that lipids containing long chain polyunsaturated fatty acids (PUFAs) like docosahexaenoic acid (DHA) were abundant among nAChR boundary lipids. Using a similar approach to investigate the role of lipid topology and lipid domain formation, here

3.2 Introduction

The muscle-derived nicotinic acetylcholine receptor (nAChR) (PDB 2BG9) [242] is the most abundant neurotransmitter receptor at the neuromuscular junction (NMJ) in most vertebrates, including humans [5]. Within the postsynaptic membrane, nAChRs cluster in high densities (10,000 per μm^2) to properly activate the skeletal muscle [209, 43]. As a major transmembrane protein, nAChR depends upon a highly specific lipid environment to maintain functionality. Lipids influence nAChR activity by affecting both function and organization. It is essential to understand how changes in lipid environment impact nAChR's structure and activity, given that lipids can change in response to aging and disease [254], and also vary across tissue and organism.

Over the past few decades, considerable progress has been made in uncovering lipid sensitivities associated with nAChR [79]. In a majority of experiments, researchers have prioritized studying cholesterol over other membrane lipids. Early studies revealed that, when reconstituted into membrane mixtures, nAChR failed to conduct cations across the lipid bilayer unless cholesterol was present [103, 235, 53, 102, 76]. More recently, researchers have examined the effects of membrane dynamics on nAChR organization [15, 48, 165, 190, 196, 261, 14, 19, 22, 31, 23, 198, 248, 35, 243]. In-vitro studies [19, 23] indicate that nAChRs form larger aggregates upon cholesterol depletion. Experimental evidence suggest that cholesterol-rich lipid domains, known as lipid rafts, facilitate clustering of nAChRs [54, 165, 196]. More specifically, after disrupting lipid raft formation, Zhu et al. observed a significant loss of nAChR clusters in-vitro [261]. In the mature neuromuscular membrane, nAChRs are linked by the intracellular anchoring protein, rapsyn, which bridges receptors together at their bases [264]. According to fluorescent studies [165], lipid rafts mediate the association between rapsyn and neighboring nAChR molecules. In the mid-2000's, Willmann et al.

and Stetzkowski-Marden et al. proposed that lipid rafts can stabilize receptor networks and may even provide a localized environment for nAChR [250, 233].

Domain formation occurs when a membrane is comprised of at least three lipid types: cholesterol, unsaturated fatty acids, and a molecule that interacts closely with cholesterol such as saturated fatty acids or sphingomyelin [99, 255]. The membrane separates into at least two domains, a liquid-ordered or “raft” phase containing cholesterol and saturated lipids/sphingomyelin, and a liquid-disordered phase containing unsaturated lipids. Polyunsaturated phospholipids make these domains more well-defined [155]. Some results from atomistic simulations [230, 131] indicate that cholesterol may preferentially partition to the boundary between liquid-ordered phases and liquid-disordered phases composed of monounsaturated lipids. In neuromuscular membranes, intrinsic domain formation is dependent upon several lipid species, including the widely influential omega-3 (ω -3) fatty acids. One ω -3 in particular, Docosahexaenoic acid (DHA), is prevalent in the native neuromuscular membrane and is strongly associated with flexible and well-defined domains [241, 224]. Additionally, DHA is a major contributor to brain functioning, motor activity, and cardiac health; however, its specific effects on neuromuscular health are poorly understood [149, 246, 108].

Characterizing such complex lipid-protein interactions requires detailed information on each molecular structure. The nAChR is a member of a family of ion channels, known as pentameric ligand-gated ion channels (pLGICs), which has a number of recent structures [151, 150, 172, 6, 125, 182, 13, 77, 186, 204, 217]; however, only single structures have been determined, rather than dimers. pLGICs are composed of five subunits; each subunit is composed of an extracellular domain for ligand binding, a transmembrane domain (TMD), and an intracellular domain (ICD) (Figure 1A). The TMD is the embedded portion of pLGICs that interacts most often with surrounding membrane lipids; this region of pLGICs is composed of four alpha-helices, M1-M4, with the innermost, M2 helices forming

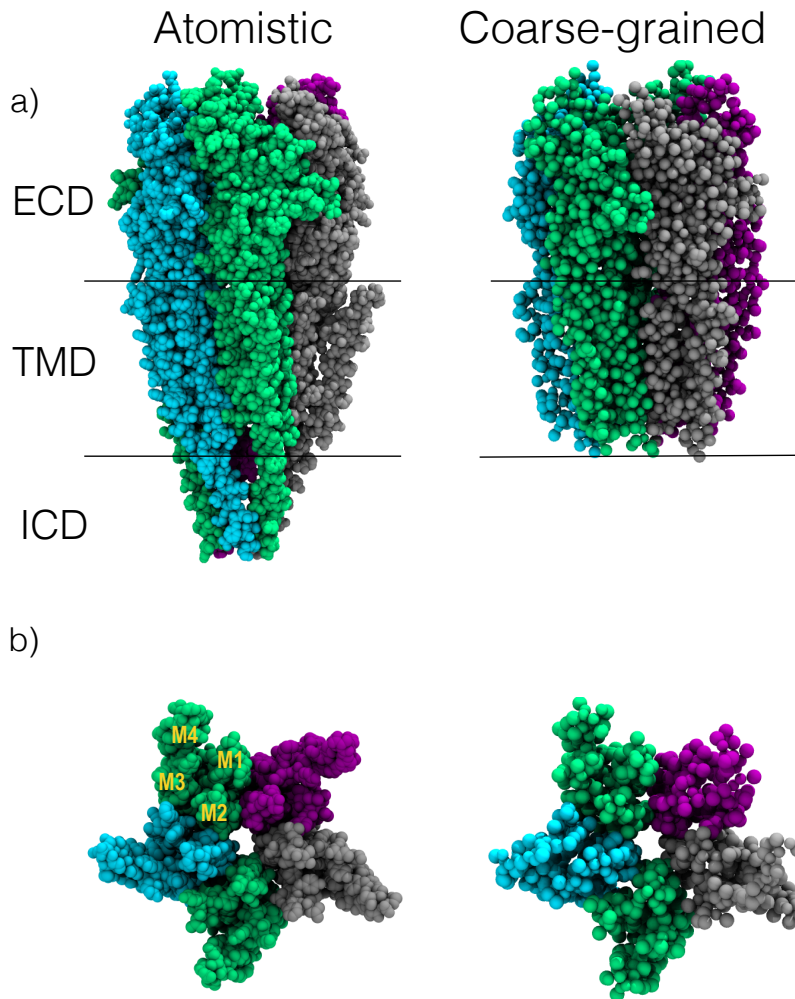


Figure 3.1: Nicotinic acetylcholine receptor (nAChR) structure. a) Atomistic and coarse-grained representations of Unwin et al's cryo-EM structure, PDB 2BG9. The nAChR is colored by subunit (α : green, β : purple, δ : gray, γ : cyan) and labeled by structure. The extracellular domain (ECD) is located above the bilayer and is critical for ligand-binding. The transmembrane domain (TMD) is positioned within the lipid bilayer, and the intracellular domain (ICD) is located in the cytoplasm. The coarse-grained model omits the ICD since it is poorly resolved and not necessary for this study. b) TMD from the extracellular perspective, with its four alpha helices labelled in a single α subunit. The outermost M4 helices closely interact with surrounding membrane lipids, while the M2 helices outline the ion pore; the M1 and M3 helices make up the body of the transmembrane domain [242].

the ion pore. The ICD, or cytoplasmic domain, is highly disordered, making it challenging to obtain information on its structure. Currently, there are two structures of nAChR pentamers resolved from x-ray crystallography (neuronal type) and cryo-electron microscopy (muscle-type) [182, 242].

Other closely related channels have been resolved with bound lipids. In 2017, the inhibitory neurotransmitter receptor, the gamma-aminobutyric acid (GABA_A) receptor, was crystallized with a cholesterol molecule protruding between its M1 and M3 helices [150], similar to our previous prediction [124]. Interestingly, x-ray structures of the glutamate-gated chloride channel (GluCl) revealed embedded POPC phospholipids in the same location [6]. Together, these data provide evidence for lipid-based modulation of pLGICs, which can potentially be applied to the gating of nAChR.

Structural information alone, however, is insufficient for answering questions about native cell membranes. For one, most structures are obtained under artificial conditions, using detergents or nanodisks with non-native lipid composition. Additionally, current structures do not represent oligomers, particularly in a liquid state. Fully atomistic molecular dynamics (MD) simulations [42, 65, 124, 56] have complemented experimental investigations of pLGICs interacting with lipids, but they are limited in their ability to capture domain formation since atomistic lipids cannot diffuse over typical simulation microsecond time scales [129, 34, 194, 110, 222]. Furthermore, it is unfeasible to incorporate multiple nAChRs in simulations with atomistic resolution. Coarse-grained MD (CG-MD) simulations are run over longer length and time scales, making them suitable for exploring complex model membranes. CG-MD is widely applied in simulations of both lipid-protein binding and domain formation [34, 222, 194, 110]. Additionally, CG-MD can capture large-scale membrane phenomenon such as protein self-assembly and lipid-mediated oligomerization [105, 12].

Recently, we [225] conducted CG-MD simulations of a single nAChR from

the electric ray *Torpedo* in mixed membranes. Contrary to expectations, nAChR consistently preferred a local lipid environment rich in PUFAs rather than cholesterol, especially long-chained ω -3s, such as DHA. While cholesterol occupied the transmembrane gaps of nAChR, PUFAs were even more likely to be embedded, regardless of their phospholipid headgroup.

The present study adopts a similar approach, with a particular focus on nAChR-associated clustering. Through molecular dynamics simulations, we investigate nAChR lipid preferences and clustering behavior in membranes with and without domains. For this study, we tested three major hypotheses: 1) Membrane organization affects nAChR boundary lipid specificity: when PUFA chains are prevented from forming PUFA rich domains, their prevalence among nAChR boundary lipids will be significantly reduced. 2) Domain formation will indirectly facilitate the clustering of nAChRs, by inducing partitioning preferences and restricting diffusion within the membrane. 3) Within a dimer, we will observe sequence preferences in facing subunits.

3.3 Methods

3.3.1 System setup

In order to isolate the role of lipid domain formation on nAChR-based lipid sorting and clustering, our simulations compared two different membranes with distinct phospholipid topology. Each membrane had 30% cholesterol and 70% phospholipids. The phospholipids all had phosphatidylcholine (PC) headgroups, and half the total number of acyl chains were saturated (16:0) chains, while the other half were polyunsaturated (22:6) chains. For homoacid membranes, all phospholipids had either two polyunsaturated acyl chains (didocosahexaenoylphosphatidylcholine or dDHA-PC) or two saturated chains (dipalmitoylphosphatidylcholine or DPPC), facilitating domain-formation. In the heteroacid membranes,

all phospholipids were hybrid lipids with one polyunsaturated acyl chain and one saturated chain (1-palmitoyl- 2-docosahexaenoyl- phosphatidylcholine or PDPC), which are topologically unable to separate into PUFA-rich and PUFA-poor domains.

Lipids and proteins were modeled using the coarse-grained (CG) Martini 2.2 force field [167]. Systems included between 1-4 nAChR molecules, derived from the Torpedo electric organ [242] (PDB 2BG9). This structure is the only pLGIC structure obtained in a native membrane.

We converted protein structures into CG models using the Martini script "martinize.py", mapping four non-hydrogen atoms to one CG interaction. We constructed and assembled our protein-bilayer systems using the Martini script, "insane.py", using a box sizes of 29x29x21 nm³ for one-to-two proteins, 40x40x20 nm³ for three proteins, and 44x44x22 nm³ for four protein systems, respectively [168]. Initially, the proteins were in a circle of about 13 nm. The receptors were evenly spaced, and their δ subunits were facing the same direction. Once simulations started, nAChRs shifted from their initial orientations. We ran 24 CG-MD simulations containing 1-4 nAChRs (3 replicas per system).

3.3.2 Simulation details

Simulations were run using the Martini 2.2 force field parameters and the Gromacs 5.1.2 simulation package, [168, 205] as in our previous work, [225]. Each simulation consisted of two steps: energy minimization and molecular dynamics. For each system, we ran two consecutive energy minimizations for 10,000 steps. Harmonic restraints between backbone atoms were imposed to preserve nAChR conformation. More specifically, we applied an elastic force constant of 750 kJ/mol and set lower and upper bounds on the bond with using a bond length of 0.7 nm [168, 205]. The molecular dynamics simulations ran for 10-20 μ s at a 0.025 ps time-step. Simulation temperature and pressure were kept constant at

values of 323 K and a reference pressure of 1 bar. The isotropic pressure coupling compressibility constant was maintained at 3.0×10^{-5} bar $^{-1}$.

3.3.3 Analysis

For a given nAChR, n_{emb}^{α} is the total number of embedded lipids of lipid species α , where embedded lipids satisfy the following criteria: the headgroup (in the case of cholesterol) or the terminal bead on the acyl chains (in the case of phospholipids) are within 10 Å of the M2 helices. Visual inspection indicated any lipids outside of this range were also outside of the TMD bundle.

Similarly, n_{ann}^{α} is the total number of annular lipids of lipid species α , where annular lipids satisfy the following criteria: headgroup or the terminal bead on the acyl chains is between 10 Å and 35 Å of the M2 helices. This range of lipids corresponded to the third lipidation shell around nAChR.

(For phospholipids, each acyl chain was counted separately as a half-lipid, so it was possible for e.g. the sn-1 chain to be embedded and the sn-2 chain to be annular.)

Boundary lipid fractions for a given species α are defined as

$$f_{\text{emb}}^{\alpha} \equiv \frac{n_{\text{emb}}^{\alpha}}{n_{\text{emb}}}, \quad (3.1)$$

$$f_{\text{ann}}^{\alpha} \equiv \frac{n_{\text{ann}}^{\alpha}}{n_{\text{ann}}} \quad (3.2)$$

where n_{emb} and n_{ann} are the total number of embedded and annular lipids, respectively.

Two dimensional density distributions of boundary acyl chain species (B), $\tilde{\rho}_B(r_i, \theta_j)$ were calculated, as a function of radius, r_i , and angle θ_j projected onto the membrane.

$$\rho_B(r_i, \theta_j) = \frac{\langle n_B(r_i, \theta_j) \rangle}{r_i \Delta r \Delta \theta} \quad (3.3)$$

where $r_i = i\Delta r$ is the distance from the origin to the center of bin i , Δr is the radial bin width, and $\Delta\theta$ is the angular bin width. $\langle n_B(r_i, \theta_j) \rangle$ is the time-averaged number of acyl chain beads of species B within bin i .

To quantify enrichment or depletion of a given acyl chain with respect to random distribution, the normalized density, $\tilde{\rho}_B(r_i, \theta_j)$, was calculated.

$$\tilde{\rho}_B(r_i, \theta_j) = \frac{\rho_B(r_i, \theta_j)}{x_B s_B N_L / \langle L^2 \rangle} \quad (3.4)$$

where s_B is the number of beads of lipid species B, N_L is total number of lipids in a system, and $\langle L^2 \rangle$ is the average projected box area, and x_B is lipid B concentration. The expression does not take into consideration the protein footprint or undulations present within the system, and as such is an approximation.

The radial distribution function $g(r)$ of multiple nAChRs was calculated using the three dimensional distance r between the centers of mass of the receptors for each of the 8000 frames, evenly distributed through the simulation. It was derived from the distribution of pairwise separations, $P(r)$, by dividing by the expected separations in a random distribution : $g(r) = \frac{P(r)}{r} \frac{dr}{dr} \times \int_0^R r dr$. The height of the $g(r)$ peak corresponds to the amount of enrichment in probability for a given distance; for example, if $g(10 \text{ nm}) = 50$, it is 50 times more probable that two monomers will be 10 nm apart than expected in a random distribution.

The total number of observed dimers n_d is given by the number of pairs (across all analyzed proteins) where $r < 100 \text{ \AA}$. For each observed dimer, the closest subunit pair was determined, and the enrichment calculated as $F_{x,y}$:

$$F_{x,y} = \frac{25}{n_d} (n_{x,y} + n_{y,x}), \quad (3.5)$$

where $n_{x,y}$ represents the number of dimers in which subunits x and y form the closest pair, and 1/25 is the expectation for a random distribution.

We visualized and imaged all simulation results using Visual Molecular Dynamics (VMD) [126].

3.4 Results

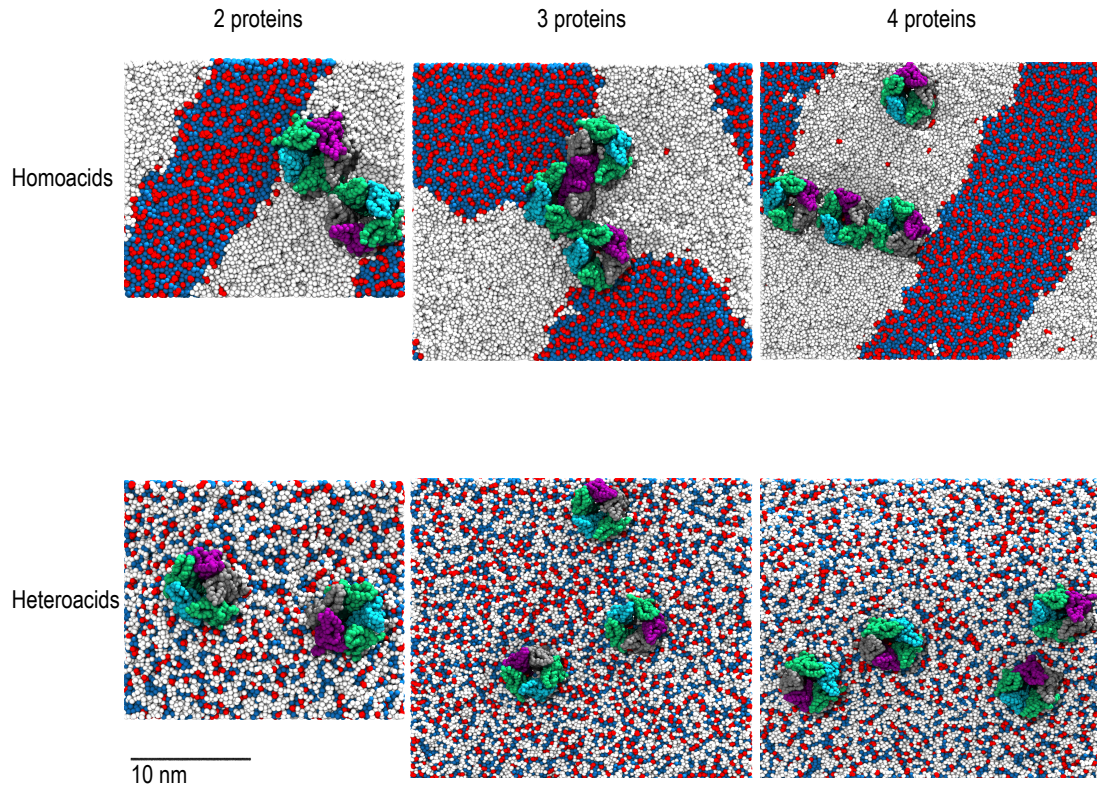


Figure 3.2: Protein clustering in domain-forming (top row) and hybrid (bottom row) membranes. View of the membrane from the extracellular region at the final frame of $10 \mu s$ simulations. nAChRs were colored by subunit (α : green, β : purple, δ : gray, γ : cyan), and lipids by acyl chain (DHA: white, saturated: blue, and cholesterol: red). Clustering of nAChRs on the borders of lipid rafts is visible in the domain-forming membranes.

3.4.1 nAChR boundary lipid preferences

	mean embedded fraction		mean annular fraction		bulk
	homoacid	heteroacid	homoacid	heteroacid	
cholesterol	0.29 (0.02)	0.42 (0.04)	0.23 (0.02)	0.31 (0.01)	0.30
PUFA	0.61 (0.01)	0.39 (0.04)	0.52 (0.02)	0.32 (0.01)	0.35
saturated	0.10 (0.05)	0.19 (0.01)	0.25 (0.02)	0.37 (0.01)	0.35

Table 3.1: Composition of nAChR Boundary Lipid chains in domain forming (homoacidic) and non-domain forming (heteroacidic) membranes. Embedded and Annular chains are determined as described in Methods. Averages are across systems, and across proteins in multi-protein systems. Each protein is treated as a separate replica ($n=30$) and standard errors are shown in parentheses.

In order to determine the significance of domain formation on enrichment of polyunsaturated acyl chains among boundary lipids, we calculated the fraction of embedded and annular boundary lipids in two types of membranes with equal amounts of cholesterol and saturated and polyunsaturated acyl chains. In the domain-forming membranes, all phospholipids had either two polyunsaturated acyl chains or two saturated chains (homoacids), while in the non-domain forming membranes, all phospholipids had one polyunsaturated acyl chain and one saturated chain (heteroacids).

Distributions for f_{emb} and f_{ann} are shown in Figure 3.3 in heteroacids compositions without domains and in Figure 3.4 for homoacids compositions with domains, while mean values are given in Table 3.1. For heteroacids, PUFA chains are slightly enriched among embedded chains and slightly depleted among annular chains, while the reverse trend is observed for saturated lipids. Saturated chains are significantly depleted from the embedded lipids, but due to the topology of

these lipids, a fully embedded polyunsaturated acyl chain must also contribute a saturated chain to the protein annulus. Distributions were remarkably consistent across simulations containing 1,2,3, or 4 proteins.

Figure 3.4 shows the results of the same analysis for homoacidic membranes. Replacing heteroacids with homoacids substantially increases the fraction of polyunsaturated chains among both embedded and annular lipids, with the peak of the distribution shifting further to the right as more proteins are included (Figure 3.4).

Together, these results are consistent with our previous [225] observation that polyunsaturated chains can displace cholesterol from embedded sites. For heteroacids, embedding a PUFA constrained the linked saturated chain to the nAChR annulus. In this case, cholesterol (which introduces no such constraint) was enriched among embedded lipids. For homoacids, embedded PUFAs constrained a corresponding PUFA chain to the nAChR annulus, and here cholesterol was not enriched among embedded lipids.

The fraction of embedded chains that were polyunsaturated increased as more proteins were added to the homoacidic membrane. This could be consistent with each nAChR monomer in an oligomer blocking access to embedded lipid binding sites in the other monomers: flexible PUFA chains have multiple routes to access an embedded site, and rigid lipids have only one or two.

The two dimensional density distribution of each lipid species from the center of a single nAChR is shown in Figure 3.5. For all three lipids, there was a five-fold symmetry of densities surrounding nAChR, with lipid preferences determined by transmembrane helix, rather than by subunit. In heteroacid mixtures, cholesterol is enriched near the subunit interfaces, and even buried more deeply within the γ/α interface, with saturated acyl chains packed just outside cholesterol. The outermost M4 helices, however, were packed with PUFAs; PUFA chains also diffused throughout the TMD bundle. In homoacid membranes, saturated lipids

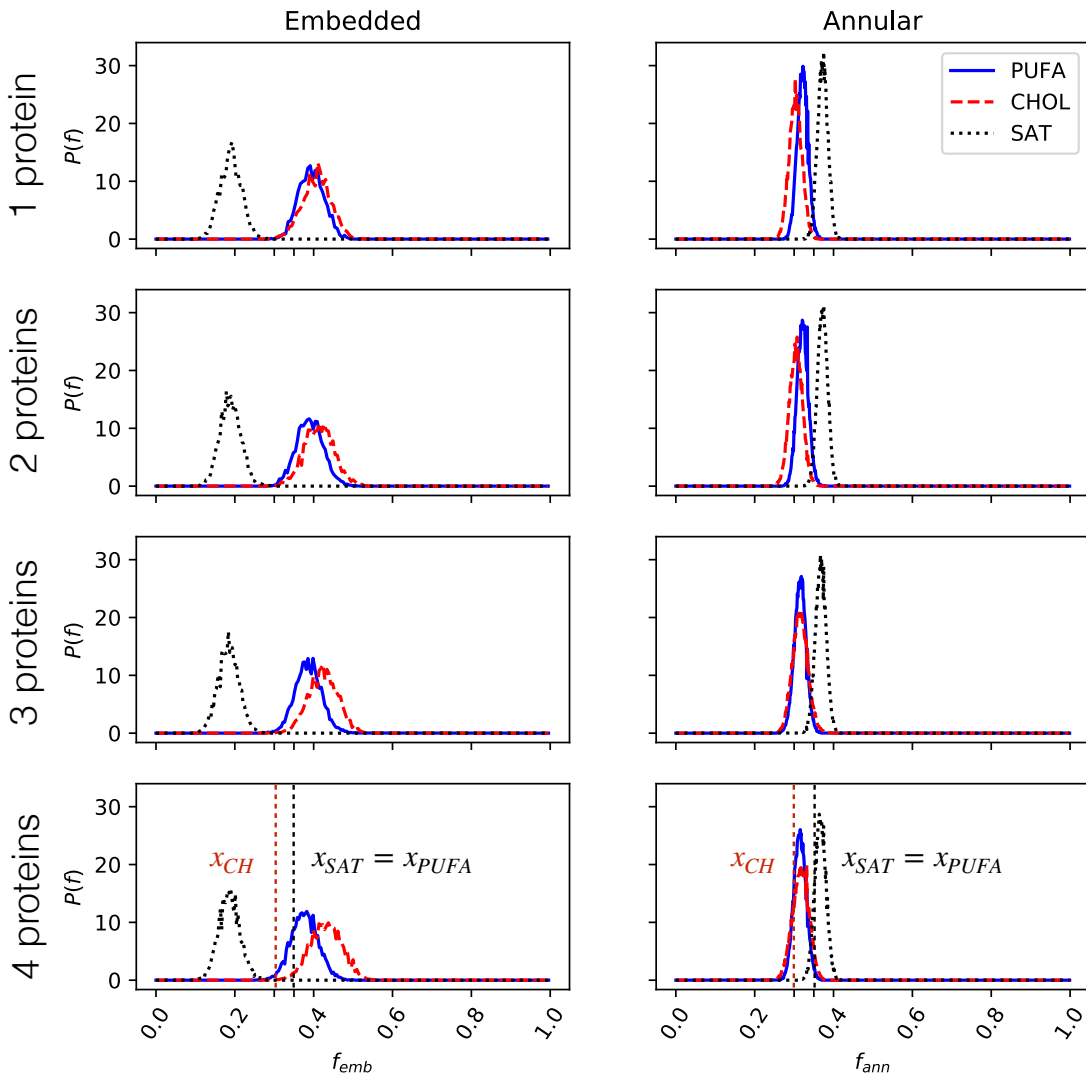


Figure 3.3: Distribution of nAChR boundary cholesterol or acyl chain fractions in mixed membranes containing homoacidic phospholipids. Probability density distribution of fraction of embedded (f_{emb}) or annular lipids (f_{ann}) as defined in Eq. 3.2 are shown for 1 to 4 proteins. Dashed lines represent expected boundary ratios for a randomly-mixed membrane, based on bulk lipid composition ($x_{CH} = 0.3$, $x_{SAT} = x_{PUFA} = 0.35$).

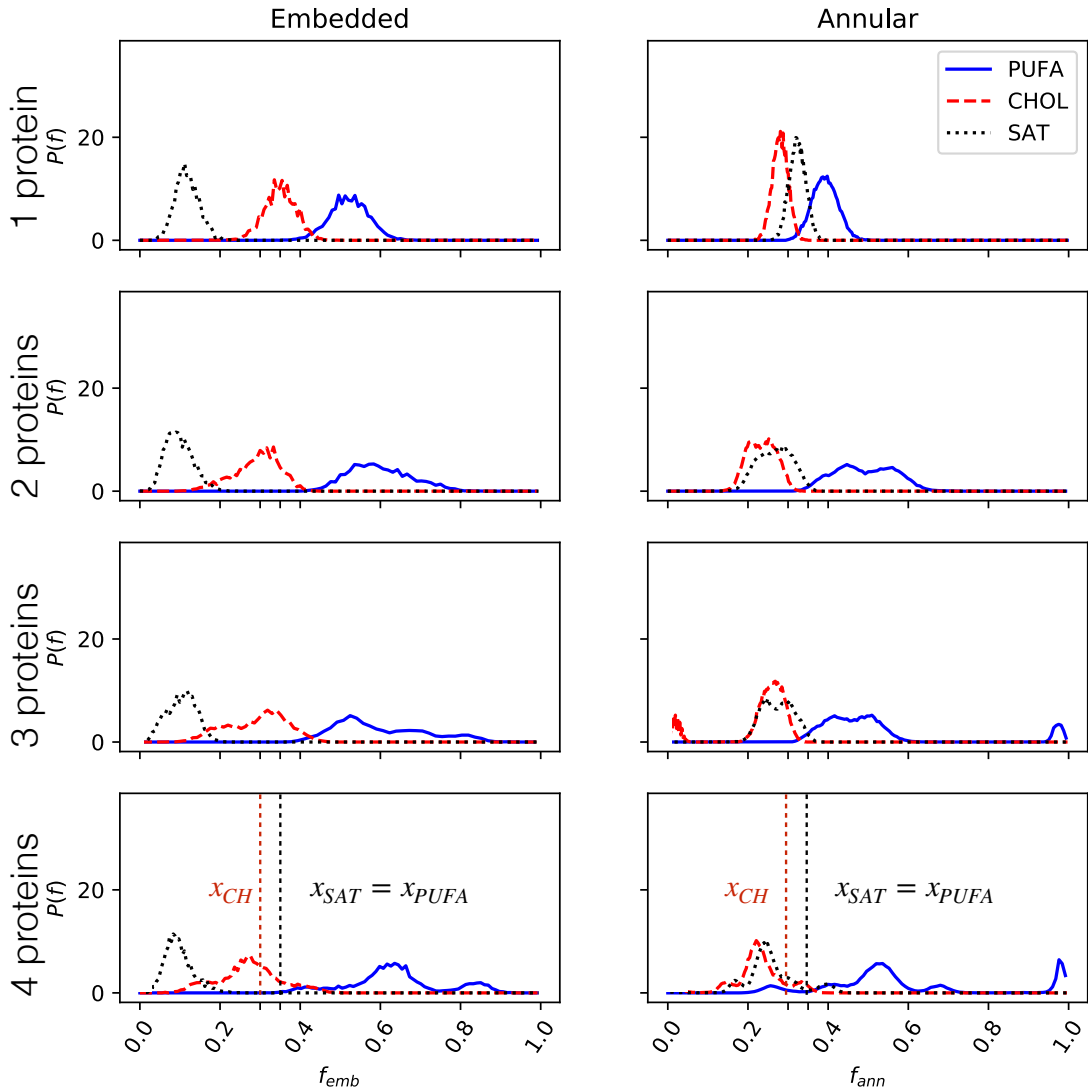


Figure 3.4: Distribution of nAChR boundary cholesterol or acyl chain fractions in mixed membranes containing heteroacidic phospholipids. Probability density distribution of fraction of embedded (f_{emb}) or annular lipids (f_{ann}) as defined in Eq. 3.2 are shown for 1 to 4 proteins. Dashed lines represent expected boundary ratios for a randomly-mixed membrane, based on bulk lipid composition ($x_{CH} = 0.3$, $x_{SAT} = x_{PUFA} = 0.35$).

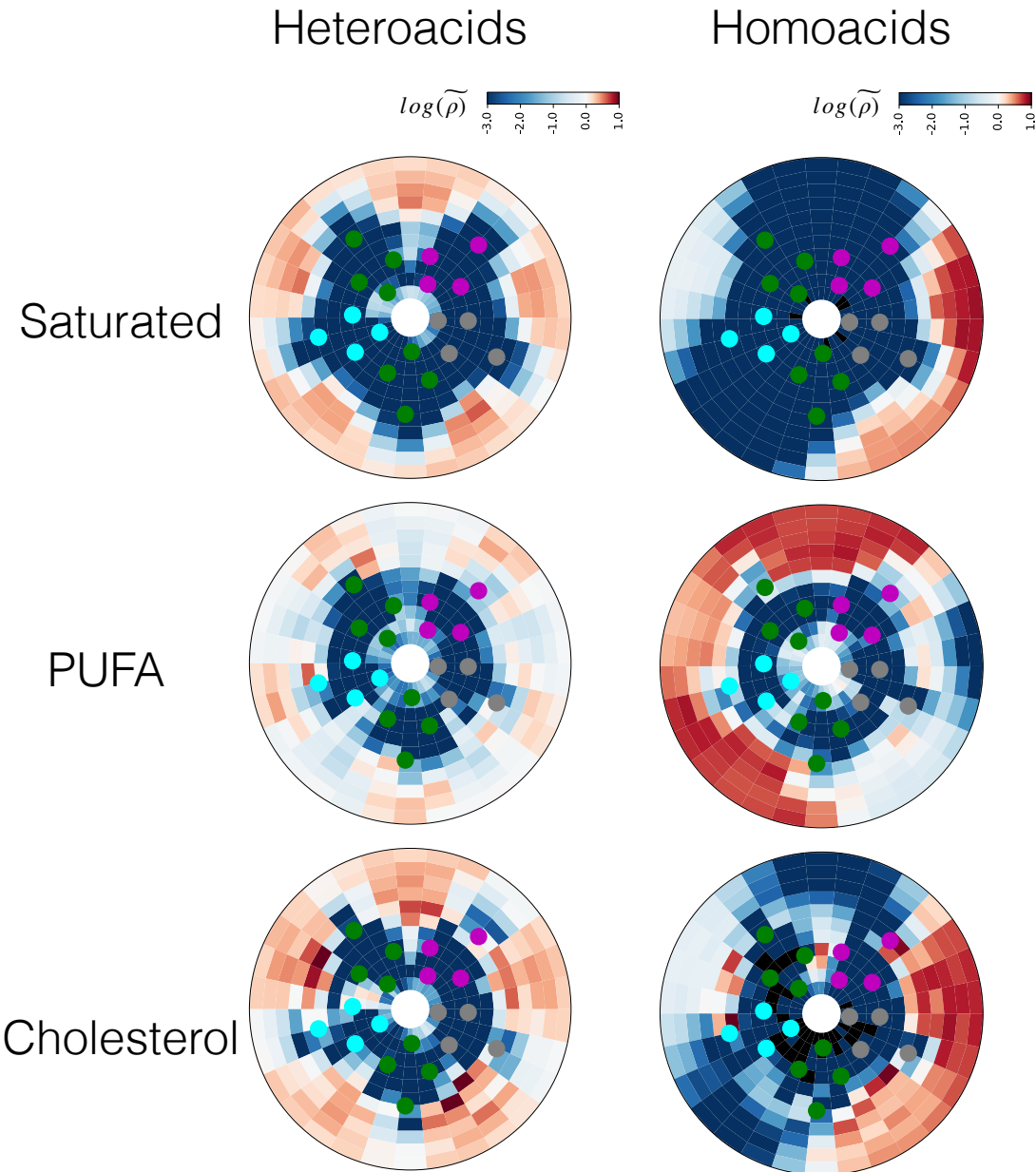


Figure 3.5: Enrichment or depletion of lipid species surrounding a single nAChR. Heatmaps represent normalized lipid densities ($\tilde{\rho}_B(r_i, \theta_j)$) as defined in Eq. 5.2, on a scale of -3 (blue, indicating depletion) to 1 (red, indicating enrichment). Densities were averaged over the last 8 μs of the 10 μs simulations and across three replicas.

and cholesterol were depleted among embedded lipids, but they maintained the same helix association observed in heteroacid membranes. PUFAs were especially enriched in domain-forming membranes, with high densities around all four transmembrane helices.

3.4.2 nAChR clustering in the presence and absence of lipid domains

Here, we repeatedly observed spontaneous formation of receptor dimers in the simulations containing multiple proteins (Figure 3.4). To investigate the role of lipid domain formation in driving nAChR oligomerization, we calculated the radial distribution function for the pairwise distances between centers of mass, as shown in Figure 3.6. For both heteroacid and homoacid membranes, we observed a peak at $r \sim 7.5$ nm, corresponding to dimerization. The differences in profiles between domain and non-domain forming membranes were primarily quantitative: most significantly, the peak corresponding to dimers was substantially higher for 2 and 3 proteins in homoacids than in heteroacids. For two proteins, the distribution for homoacids was shifted to the left, relative to the distribution for heteroacids, indicating that the peak for dimerization was at a shorter distance in domain-forming membranes. This difference is consistent with results indicating a role for domain formation in aggregation and clustering of nAChRs [19, 190, 196]. The simplest explanation of this difference is the higher effective concentration of proteins when domains are present: all nAChRs are corralled in a single liquid-disordered domain, with approximately half the area of the overall membrane.

3.4.3 Closest subunits across dimerizing proteins

In order to determine whether nAChR dimers were more likely to form with specific subunit interactions, we determined the closest interacting subunit pair

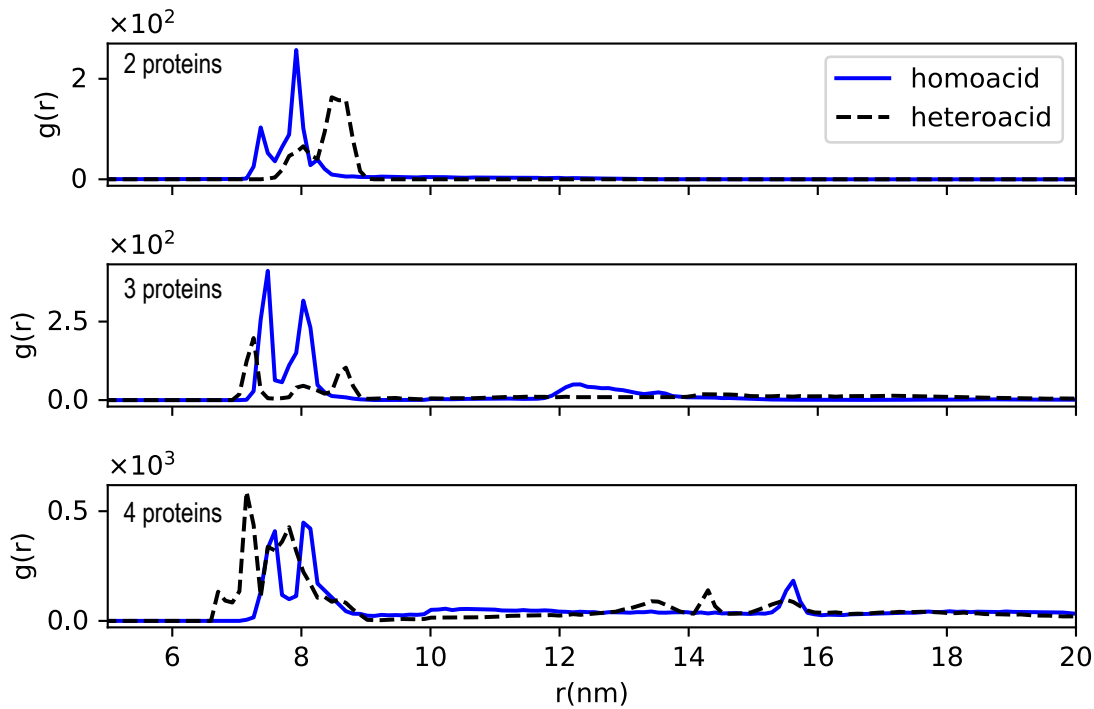


Figure 3.6: Pairwise distance distribution across multi-protein systems. Radial distribution function $g(r)$ of pairwise protein center-of-mass distances, across multi-protein systems. Data collection began at $2 \mu s$ into each trajectory and ended at $10 \mu s$, respectively. The peak between 7-10 nm corresponds to dimer formation.

for nAChR dimers within each frame. To ensure that dimers, rather than larger oligomers, were being analyzed, we excluded trimers and tetramers from the analysis and only considered two protein systems, with increased sampling. Figure 3.4.3 shows the amount of enrichment for each possible subunit pairing, relative to an expected random distribution. Results were very sensitive to the use of domain-forming compositions. In heteroacidic membranes, the α_δ subunit formed a monomer-monomer interaction with the β subunit, while the α_γ most favorably interacted with the δ subunit. In domain-forming membranes, the $\delta - \alpha_\delta - \gamma$ interface was two to five times as likely to pair with a α_δ subunit compared to a random distribution, but substantially more dispersion was detected than in non-domain forming membranes. This difference suggests that nAChRs have preferred dimerization orientations, but membrane organization can reorient receptors. Although δ subunits are linked by a disulfide bond at the NMJ [58], our simulations suggest that without this link, δ subunits do not form the closest pair among dimerizing proteins.

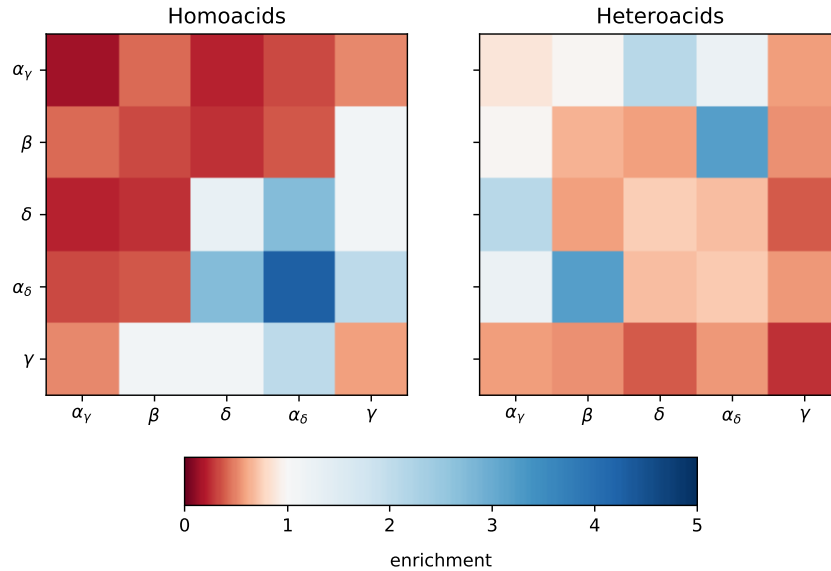


Figure 3.7: Subunit pairs among dimerizing proteins. Most probable subunit pairs among dimerizing proteins. Heat-map showing the likelihood that two subunits were closest together among dimerizing proteins (100 Å threshold). Distinct subunits are each expected to form the closest pair 8 % of the time, while identical subunits are each expected to dimerize only 4 % of the time. Each color on the heatmap represents multiplicative depletion or enrichment relative to the pair's expectation value, ranging from complete depletion (red) to no enrichment (white) to five-fold enrichment (blue).

3.5 Discussion

The nAChR is one of the most well-studied, fundamental pLGICs for understanding human cognition, memory, and muscle contraction [111]. As an integral membrane protein, the function and organization of nAChR is strongly dictated by its surrounding lipid environment. DHA is an ω -3 polyunsaturated fatty acid abundant in synaptic membranes and the Torpedo electric organs, which are both native nAChR membranes. With its six double bonds, DHA is considered highly disordered and can induce domain formation in membranes [246]. We previously observed [225] favorable interactions between a single nAChR and DHA-rich, cholesterol-poor domains using coarse-grained simulations. Here, we have extended this approach to investigate the role of lipid topology and domain-formation on boundary lipids of individual nAChRs. We have also conducted the first simulations containing multiple nAChRs, which has allowed us to observe spontaneous dimerization.

While DHA is implicated in human health and disease, [149] experimental studies considering its interactions with nAChR have exclusively considered its free-fatty acid form (FFA), [9] rather than as an acyl chain component of a phospholipid. Application of $\omega - 3$ FFAs causes a significant reduction in open times observed through single-channel recordings [36]. Here, we observe a substantial effect of lipid topology on both embedded and annular lipids: DHA chains in homoacidic phospholipids are far more likely to be found as either annular or embedded boundary lipids. We previously observed only quantitative effects of swapping PE with PC on partitioning, but the headgroup does serve to anchor the lipid at the membrane/protein interface [225]. DHA in its FFA form (without a headgroup) may diffuse into an open nAChR pore, blocking the channel.

We find that, consistent with coarse-grained MD simulations using one nAChR [225], multiple nAChRs continue to prefer the liquid-disordered phase containing

long-chain ω -3 fatty acids. While the number of nAChRs in the system did not affect the partitioning profile in these simulations, it did affect the composition of embedded lipids. Our results are consistent with each nAChR monomer in an oligomer blocking access to embedded lipid binding sites in the other monomers, suggesting an intriguing coupling between specific binding and membrane organization.

Interestingly, upon removing membrane organization, embedded lipids cluster around specific transmembrane helices in a five-fold symmetry around nAChR. This finding suggests that intrinsic lipid preferences are primarily helix dependent, rather than subunit dependent. In homoacid membranes, a lipid preference for DHA was observed across all transmembrane helices, with shells of PUFAs found even at the border of the liquid-ordered phase. Although saturated acyl chains and cholesterol were generally depleted around nAChR, the highest densities for both lipids were found around the M1 and M3 helices, as seen in heteroacid membranes.

In native membranes, nAChR dimers can be stabilized by a disulfide bond between δ subunits [58]. An early controversy [8, 212, 263, 219] concerned whether the disulfide bond was necessary for dimer formation. There is no mechanism for covalent bonds between monomers in these coarse-grained simulations. All dimers were stabilized by non-covalent interactions, consistent with the results of [212, 219]. We observed far more stable dimers in the homoacid mixtures than the heteroacid mixtures, which would be consistent with high sensitivity to experimental conditions. We did not observe a consistent $\delta - \delta$ preference for interfacing subunits in either homoacid or heteroacid mixtures. Schindler *et al* (1984) observed an apparent gain-of-function for single-channels within dimers relative to monomers, regardless of disulfide linking [219], suggesting that lipid modulation of oligomerization could also provide a pathway for modulating single channel function.

Chapter 4

Direct binding of phosphatidylglycerol at specific sites modulates desensitization of a ligand-gated ion channel

Originally published in: eLife, 2019, vol 8, pages 1-23

Ailing Tong¹, John T. Petroff II¹, Fong-Fu Hsu², Philipp A. M. Schmidpeter³, Crina M. Nimigean³, Liam Sharp⁴, Grace Brannigan^{4,5}, Wayland W. L. Cheng^{1,*}

From the Departments of ¹Anesthesiology, and ²Internal Medicine, Mass Spectrometry Resource, Division of Endocrinology, Diabetes, Metabolism, and Lipid Research, Washington University in St. Louis, MO, USA, ³Departments of Anesthesiology, and Physiology and Biophysics, Weill Cornell Medicine, NY, USA, and the ⁴Center for Computational and Integrative Biology and ⁵Department of Physics, Rutgers University, Camden, NJ, USA.

*To whom correspondence should be addressed: Professor Wayland W. L. Cheng, Department of Anesthesiology, Washington University School of Medicine, Campus Box 8054, St. Louis, MO 63110. Telephone: (314)273-7958; E-mail: wayland.cheng@wustl.edu

4.1 Abstract

Pentameric ligand-gated ion channels (pLGICs) are essential determinants of synaptic transmission, and are modulated by specific lipids including anionic phospholipids. The exact modulatory effect of anionic phospholipids in pLGICs

and the mechanism of this effect are not well understood. Using native mass spectrometry, coarse-grained molecular dynamics simulations and functional assays, we show that the anionic phospholipid, 1-palmitoyl-2-oleyl-phosphatidylglycerol (POPG), preferentially binds to and stabilizes the pLGIC, *Erwinia* ligand-gated ion channel (ELIC), and decreases ELIC desensitization. Mutations of five arginines located in the interfacial regions of the transmembrane domain (TMD) reduce POPG binding, and a subset of these mutations increase ELIC desensitization. In contrast, the L240A mutant increases POPG binding and decreases ELIC desensitization. The results support a mechanism by which POPG stabilizes the open state of ELIC relative to the desensitized state by direct binding at specific sites.

4.2 Introduction

Pentameric ligand-gated ion channels (pLGICs) are essential determinants of synaptic transmission, and the targets of many allosteric modulators including general anesthetics and anti-epileptics (1). These ion channels are embedded in a heterogeneous and dynamic lipid environment (2), and the presence of specific lipids fine-tunes the function of pLGICs and may play a role in regulating neuronal excitability and drug sensitivity (3-5). One nearly ubiquitous example is that of anionic phospholipids, which are known to modulate pentameric ligand-gated ion channels (pLGICs) such as the nicotinic acetylcholine receptor (nAChR) (6), as well as inward rectifying potassium channels (7), K(2P) channels (8), voltage-gated potassium channels (9, 10), and cyclic nucleotide-gated channels (11). In pLGICs, anionic phospholipids have been shown to shift the conformational equilibrium of the channel from an uncoupled or desensitized state to a resting state, in which agonist binding is effectively coupled to channel activation (12-14).

Studies of lipid modulation of ion channel function including modulation of

pLGICs have focused on two central questions: 1) what is the exact effect of the lipid on channel function and structure, and 2) is the effect attributable to direct binding of the lipid at specific sites? *Torpedo* nAChR channel activity measured from flux assays (6, 15, 16) and agonist-induced conformational changes (13, 17) depend on anionic phospholipids. However, few studies have employed fast solution changes to measure current responses of pLGICs in model membranes (18), which is necessary to distinguish the effect of lipids on channel gating, specifically transitions between resting, open and desensitized states. With regard to lipid binding, early studies using electron paramagnetic resonance (EPR) of spin-labeled lipids or lipid-induced modification of fluorescent probes revealed an immobilized layer of lipids surrounding nAchRs that is enriched for certain phospholipids (19, 20) with lipids occupying specific sites (21, 22). These approaches are, however, an indirect means to examine lipid binding to ion channels. More recently, crystal structures of the pLGIC, *Gloeo*bacter ligand-gated ion channel (GLIC), revealed bound, co-purified phospholipids in a putative open structure, and the absence of one of these phospholipids in a locally-closed structure (23, 24). Similarly, a putative desensitized structure of GLIC with a bound polyunsaturated fatty acid showed loss of the aforementioned phospholipid density that is bound to the open state (25). Both of these studies suggest that bound phospholipids at specific sites stabilize the open state of the channel, although the identity of these lipids remains unknown. Furthermore, the absence of a lipid density in a crystal structure is not necessarily an indication of lack of binding.

Native mass spectrometry (MS) has proven to be a powerful tool to directly measure binding of endogenous and exogenous lipids to membrane proteins (26, 27), although this approach has yet to be used to examine pLGIC-lipid interactions. In addition, coarse-grained molecular dynamics (MD) simulations provide a complementary approach to examine lipid interactions with

membrane-embedded pLGICs at time scales that allow equilibration of lipid binding sites (28, 29). We sought to determine whether phospholipids bind directly and selectively to a pLGIC by native MS and coarse-grained MD simulations, and whether specific binding interactions modulate channel function by patch-clamp recordings and stopped-flow ion flux measurements from liposomes of defined lipid composition. *Erwinia* ligand-gated ion channel (ELIC), a prototypical pLGIC and biochemically tractable target, is also sensitive to its lipid environment. ELIC was found to be inactive when reconstituted in 1-palmitoyl-2-oleyl-phosphatidylcholine (POPC) membranes fused to *Xenopus* oocyte membranes, similar to the nAChR (30). After optimizing native MS for ELIC, we demonstrate that phospholipids directly bind to ELIC, with more binding observed for the anionic phospholipid, POPG compared to zwitterionic phospholipids, 1-palmitoyl-2-oleyl-phosphatidylethanolamine (POPE) and POPC. Consistent with this finding, coarse-grained simulations of ELIC in a lipid bilayer show enrichment of annular POPG compared to POPC or POPE phospholipids. In addition, POPG selectively stabilizes ELIC against thermal denaturation indicative of a specific binding interaction, and reduces channel desensitization. Mutations of five arginines at the transmembrane domain (TMD) intracellular and extracellular interfaces decrease PG binding while a subset of these mutations increase desensitization. Likewise, the L240A mutant, which reduces desensitization, increases PG binding. The results support the long-standing hypothesis that anionic phospholipids stabilize the open state of pLGICs by direct binding to sites in the TMD adjacent to the lipid-facing transmembrane helix 4 (TM4) (3).

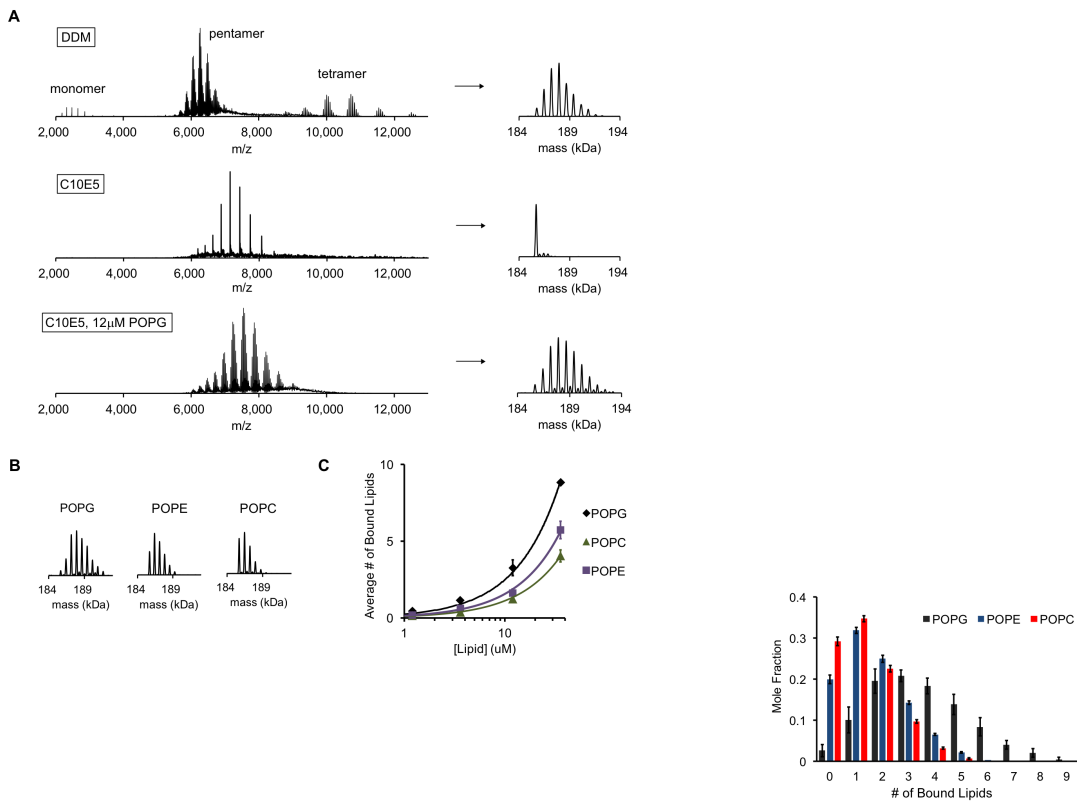


Figure 4.1: POPG binds selectively to ELIC. (A) Native MS spectra of ELIC in DDM, C10E5, and C10E5 with 12 μ M POPG. Left shows full spectra and right shows deconvoluted spectra. (B) Deconvoluted spectra of ELIC in 12 μ M of the indicated phospholipid. (C) Plot of the average number of bound phospholipids per pentamer at varying concentrations of POPG, POPE and POPC ($n=3-6$, $\pm SD$). Data are fit to a sigmoid binding curve.

4.3 Results

4.3.1 Selective binding of phospholipids to ELIC

Native MS of ELIC purified in dodecyl maltoside (DDM) was optimized on a Q-Exactive EMR mass spectrometer as previously described (27). Optimal desolvation of the pentamer required activation energies that resulted in some dissociation into tetramer and monomer (Fig. 4.1A). Nevertheless, both the pentamer and tetramer species showed multiple bound small molecules of ~750 Da, likely corresponding to co-purified phospholipids (up to 8 and 6 lipids per multimer were observed for the pentamer and tetramer, respectively) (Fig. 4.1A). To determine the identity of these lipids, we performed a lipid extraction from the purified ELIC preparation, and analyzed the sample using tandem MS. This revealed multiple PE and PG phospholipids with different acyl chains that mirror the phospholipids extracted from *E. coli* membranes (Table C1). Quantification of the MS intensities for PG relative to PE species yielded a higher relative abundance of PG co-purified with ELIC compared to *E. coli* membranes, suggesting that ELIC preferentially binds PG in its native environment (Fig. C1, Table C1).

To examine direct binding of exogenous phospholipids to ELIC, we performed a detergent screen to delipidate ELIC focusing on detergents that are also superior for native MS measurements (31). The polyethylene glycol-based detergent, C10E5, proved best for this application, yielding a stable, delipidated pentamer by native MS with lower charge states and no dissociation of the pentamer (Fig. 4.1A). This observation is consistent with previous reports for this detergent in other membrane proteins (31, 32). Addition of varying concentrations of the anionic phospholipid, POPG, to 1 μ M ELIC showed concentration dependent binding (Fig. C2). We quantified this binding by calculating the average number of bound phospholipids at each concentration. For example, at 12 μ M POPG, native MS spectra revealed up to 9 bound POPG and an average of 2.9 POPG per

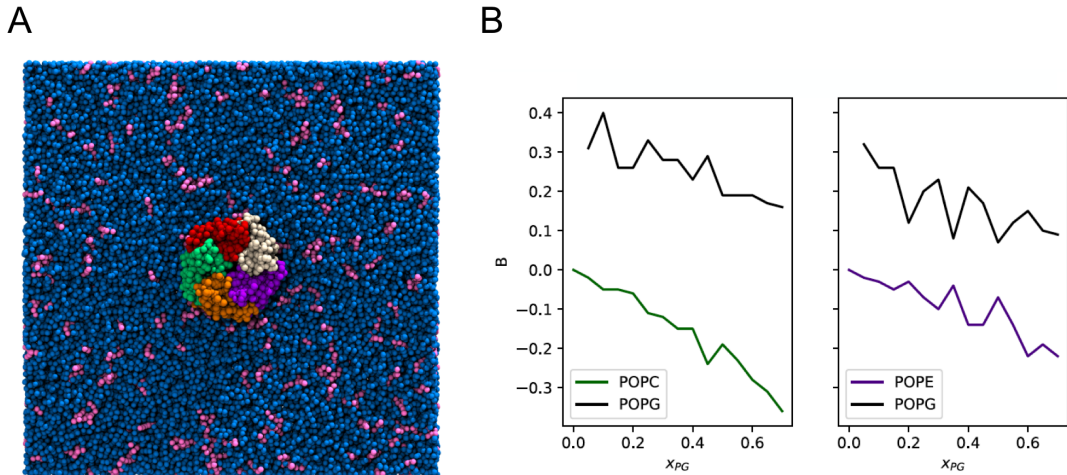


Figure 4.2: Enrichment of POPG among ELIC boundary phospholipids from coarse-grained simulations. (A) Image of the simulation model of ELIC embedded in a membrane consisting of 10% POPG (pink) and 90% POPC (blue). The view is from the extracellular side of ELIC perpendicular to the membrane. (B) The boundary enrichment metric, B , is shown for phospholipid species in POPC/POPG membranes (left) or POPE/POPG membranes (right) over a range of POPG mole fractions (x_{PG}). B is defined in Equation 4.3 (see Methods) and reflects the fractional difference between the amount of a lipid species found in the boundary and the bulk membrane: $B>0$ indicates enrichment, $B<0$ indicates depletion, and $B=0$ indicates no difference in mole fraction between the bulk and the boundary.

pentamer (Fig. 4.1B and 1C). The average number of bound POPG was equivalent for most charge states, and decreased modestly at charge states higher than +26 likely due to electrostatic repulsion within the ELIC-POPG complexes (Fig. C3); therefore, deconvolution was performed for charge states +26 and lower. Less binding was observed for the neutral phospholipids, POPE and POPC (Fig. 4.1B and 1C), indicating that the anionic phospholipid, POPG, either binds with higher affinity or at a greater number of sites.

To further examine phospholipid interactions with ELIC using a molecular model, coarse-grained MD simulations were performed on binary POPG/POPC and POPG/POPE model membranes containing a single ELIC pentamer (Fig. 4.2 A). Unlike fully-atomistic simulations, coarse-grained simulations permit significant diffusion of lipids over simulation time scales. The boundary lipid composition can thus equilibrate over the simulation time, even if it varies significantly from the bulk membrane composition. The POPG fraction was varied between 0 and 70%. Enrichment or depletion of POPG among boundary lipids for each concentration was quantified using the boundary lipid metric B (Equation 4.3, see Methods). For a given lipid species, $B > 0$ reflects enrichment, $B < 0$ reflects depletion, and $B = 0$ reflects random mixing. For POPG, $B > 0$ for all compositions tested (Fig. 4.2B). This result indicates that if POPG is present in the membrane, it is enriched among boundary lipids. This enrichment is strongest for lower amounts of POPG (i.e. lower x_{POPG}), consistent with specific binding of POPG to ELIC.

The average number of boundary phospholipids was 31.6 ± 2.5 across all compositions, and the total did not vary systematically with membrane composition. Assuming, therefore, that the stoichiometries of binding for these phospholipids to ELIC are similar, we fit the native MS binding data for each phospholipid to a binomial distribution binding model that assumes 32 binding sites of equivalent affinity (see Methods). While this is an oversimplification of phospholipid binding

to ELIC in a membrane, it provides a reasonable approximation to the MS data, and reveals that POPG binds to ELIC with ~1.9x and 2.8x higher affinity than POPE and POPC, respectively (Fig. C4). Overall, we conclude that POPG binds to ELIC with higher affinity than POPE or POPC, resulting in POPG enrichment of annular phospholipids as seen in the coarse-grained MD simulations.

4.3.2 Selective effect of POPG on ELIC stability and function

To determine the effect of POPG binding on ELIC, we first tested the stability of purified, delipidated ELIC in C10E5 against thermal denaturation in the absence and presence of POPG (33). ELIC was heated to a temperature that resulted in 85% decrease in the amplitude of the pentamer peak as assessed by size exclusion chromatography (32 °C for 15 min). POPG significantly increased the thermal stability of 1 μ M ELIC with an EC₅₀ (concentration of POPG for 50% effect) of 52 μ M (Fig. 4.4A). The thermal stabilizing effect of a phospholipid was defined as the ratio of the pentamer peak height after heating with lipid versus no lipid. In contrast, POPE and POPC had no effect on ELIC stability (Fig. 4.4A), indicating that POPG binding selectively stabilizes the structure of ELIC. Having performed our POPG binding experiment and thermal stability assay under the same conditions, it is possible to relate the average number of bound POPG to its stabilizing effect. 36 μ M POPG was the highest concentration for which the average number of bound POPG could be determined due to the overlapping of charge states from lipid-bound species (Fig.4.1A, Fig. C2). Although POPG binding does not approach saturation at this concentration, extrapolation of POPG binding and relating this extrapolation to the thermal stabilizing effect provides an approximation of the number of bound POPG needed to stabilize

ELIC against thermal denaturation. Supplementary Figure 5 shows a relationship between the number of bound POPG and the stabilizing effect, which was derived by equating the POPG concentration from the functions of POPG binding (Fig. 4.1C) and thermal stability data (Fig. 4.4A). The relationship estimates that 32 POPG (number of annular lipids in ELIC from MD simulations) yields ~82% of the thermal stabilizing effect (Fig. C5).

Next, we assessed the effect of POPG on ELIC function by reconstituting the channel in giant liposomes. Optimal formation of giant liposomes was achieved using a 2:1:1 ratio of POPC:POPE:POPG (i.e. 25 mole% POPG). In this lipid membrane composition, robust ELIC currents were elicited with excised patch-clamp recordings using the agonist, cysteamine, with a peak dose response EC₅₀ of 5.1 mM (Fig. 4.4B, Fig. 4.3, Fig. C6A). Patch-clamp recordings were performed with 0.5 mM BaCl₂ in the pipette and bath, which is predicted to result in an increase in the EC₅₀ of cysteamine response (34). Near saturating currents were achieved at 30 mM cysteamine at which ELIC activated and desensitized with time constants of 134 ms and 1.9 s, respectively (Fig. 4.4C and 3D, Fig. 4.3, Fig. C6B). These values are comparable to previous reports of outside-out patch-clamp recordings in HEK cells or oocytes (35, 36). ELIC desensitization showed complex kinetics where the majority of recordings were best fit with a double exponential and some by a single exponential. To combine data from all traces, weighted average time constants from double exponential fits were averaged with time constants from single exponential fits. The extent of desensitization was examined by measuring currents after 20 s of cysteamine application. To examine the effect of POPG on ELIC gating, excised patch-clamp recordings were performed in liposomes containing 12%, 25%, and 40% POPG. Increasing the mole% of POPG had no significant effect on cysteamine EC₅₀ values or activation kinetics (Fig. 4.4B, Fig. 4.3, Fig. C6), but reduced the rate and extent of desensitization (Fig. 4.4C and 4.4D, Fig. 4.3).

Table 4.1: ELIC WT activation and desensitization rate constants derived from a double exponential fit to the time course of flux in Fig. 4.4F (n=3, \pm SD).

	Activation Rate Constant	Desensitization Rate Constant
POPC	$24 \pm 8 \text{ s}^{-1}$	$2.4 \pm 0.08 \text{ s}^{-1}$
POPC:POPE:POPG (2:1:1)	$75 \pm 22 \text{ s}^{-1}$	$0.11 \pm 0.04 \text{ s}^{-1}$

To examine ELIC activity in the absence of POPG, a fluorescence-based stopped-flow flux assay was performed (37). ELIC was reconstituted into either POPC-alone or 2:1:1 POPC:POPE:POPG liposomes encapsulating the fluorophore ANTS (8-Aminonaphthalene-1,3,6-Trisulfonic acid). In a first mixing step, liposomes were incubated with 5 mM cysteamine to activate the channel for different amounts of time (10 ms to 25 s) after which a second mixing step was performed with Tl⁺ containing buffer. Tl⁺ can permeate through activated channels into the liposome and thus quenches ANTS fluorescence. The quenching kinetics are a measure of the channel activity upon cysteamine exposure for defined incubation times (Fig. 4.4E). In POPC liposomes, ELIC showed less cysteamine-elicited ion flux compared to ELIC in POPC:POPE:POPG liposomes (Fig. 4.4E and 4.4F, Table 4.1), as estimated from the overall rate of Tl⁺ flux. The rate of activation was modestly faster in POPC:POPE:POPG liposomes compared to POPC (Fig. 4.4F, Table 4.1). More strikingly, the rate of desensitization was greater than 20-fold faster in POPC liposomes, leading to a decrease in the lifetime of the open state (Fig. 4.4E and 4.4F, Table 4.1).

In summary, POPG selectively increases the thermal stability of ELIC, and modulates channel activity by stabilizing the open relative to the desensitized state. We hypothesize that POPG decreases receptor desensitization by direct binding at specific sites.

POPG	Desensitization		Activation	Dose Response
	Weighted τ (s)	Norm Current at 20s	τ (ms)	EC₅₀ (mM cysteamine)
12%	0.93 ± 0.32	0.05 ± 0.02	112 ± 29	5.3 ± 1.0
25%	1.95 ± 0.47	0.10 ± 0.04	134 ± 50	5.1 ± 1.2
40%	2.98 ± 0.24	0.21 ± 0.03	133 ± 66	6.5 ± 1.3

Figure 4.3: ELIC WT channel properties in giant liposomes composed of varying mole% POPG ($n=3-5$, $\pm SD$). The rate and extent of desensitization are reported as weighted time constants (τ), and the current after 20 s of 30 mM cysteamine application normalized to peak response. Also shown are activation time constants (τ) in response to 30 mM cysteamine and EC₅₀s for cysteamine activation.

4.3.3 Five interfacial arginines contribute to POPG binding

In other ion channels, guanidine groups from interfacial arginine side chains are thought to mediate binding of anionic phospholipids by charge interactions with the phospholipid headgroup (9, 38). To test the hypothesis that this mechanism is present in a pLGIC, we mutated all five arginines in the inner and outer interfacial regions of the ELIC TMD to glutamine (Fig. 4.6A). Phospholipid binding was then assessed by delipidating each mutant in C10E5, and measuring binding of POPG by native MS. While R123Q, R286Q, and R299Q could be stably delipidated, R117Q and R301Q aggregated (Fig. 4.6B). However, we found that double mutants with R299Q (i.e. R117Q/R299Q and R301Q/R299Q) could be stably delipidated. Thus, double mutants of all arginine mutants in combination with R299Q were expressed and delipidated (Fig. 4.6B). In the presence of 12 μ M POPG, the single mutants showed moderate decreases (13-18%) in the average number of bound POPG compared to WT (Fig. 4.6B). This decrease was not statistically significant. However, all double mutants significantly decreased the average number of bound POPG relative to WT by 38-41% and relative to

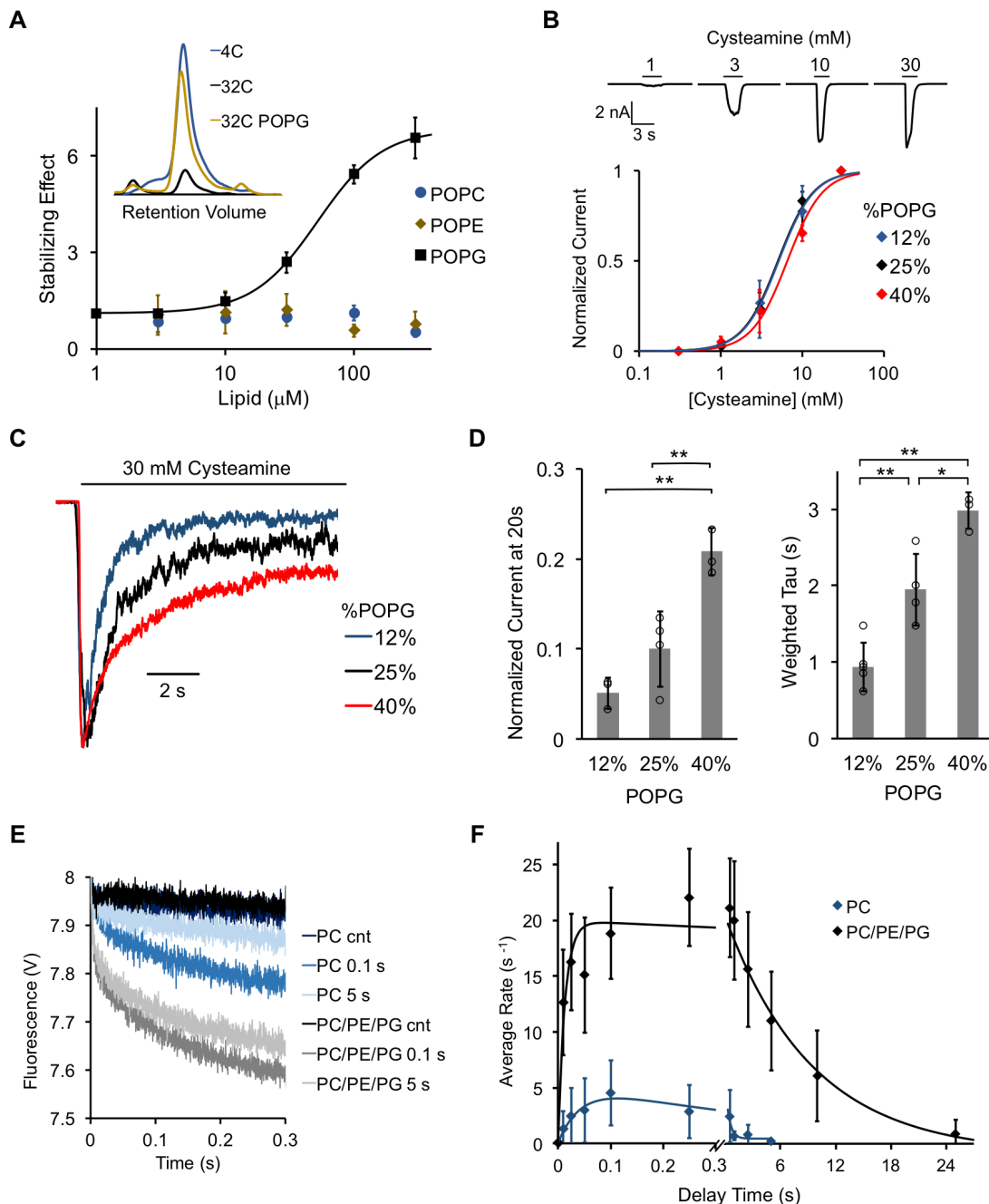


Figure 4.4: POPG selectively thermally stabilizes ELIC and decreases ELIC desensitization. Continued on the next page.

Figure 4.5: POPG selectively thermally stabilizes ELIC and decreases ELIC desensitization. (A) Plot of stabilizing effect (defined as the ELIC pentamer peak height with phospholipid relative to control after heating) versus phospholipid concentration ($n=3$, $\pm SD$; EC₅₀ = 52 μM , Hill $n = 1.7$). Inset shows size exclusion chromatography (SEC) profile in absorbance units of the ELIC pentamer treated at 4°C, 32°C, and 32°C with 100 μM POPG. (B) Top: Representative ELIC current responses to 30 mM cysteamine in 25 mole% POPG liposomes. Bottom: Normalized plots of peak current responses of ELIC to cysteamine in giant liposomes with varying mole% POPG ($n=3-5$, $\pm SD$). Data are fit to Hill equation with $n=2$. (C) Representative ELIC currents in response to 30 mM cysteamine in liposomes with varying mole% POPG. (D) Left: ELIC currents 20 s after application of 30 mM cysteamine normalized to peak response at varying mole% POPG ($n=4-5$, $\pm SD$, ** $p<0.01$). Right: Weighted tau (time constants) of ELIC desensitization at varying mole% POPG ($n=3-5$, $\pm SD$, ** $p<0.01$, * $p<0.05$). (E) Representative fluorescence-quench time courses from sequential mixing stopped-flow experiments of ELIC in POPC liposomes or 2:1:1 POPC:POPE:POPG liposomes. Proteoliposomes were mixed with no cysteamine (cnt) or 5 mM cysteamine with a 0.1 or 5 s delay prior to mixing with Tl+. Note that the control traces are superimposed. (F) Rate constants extracted from quench kinetics as shown in (E) as a function of the incubation time with cysteamine. Data are fit with a double exponential yielding activation and desensitization time constants ($n=3$, $\pm SD$).

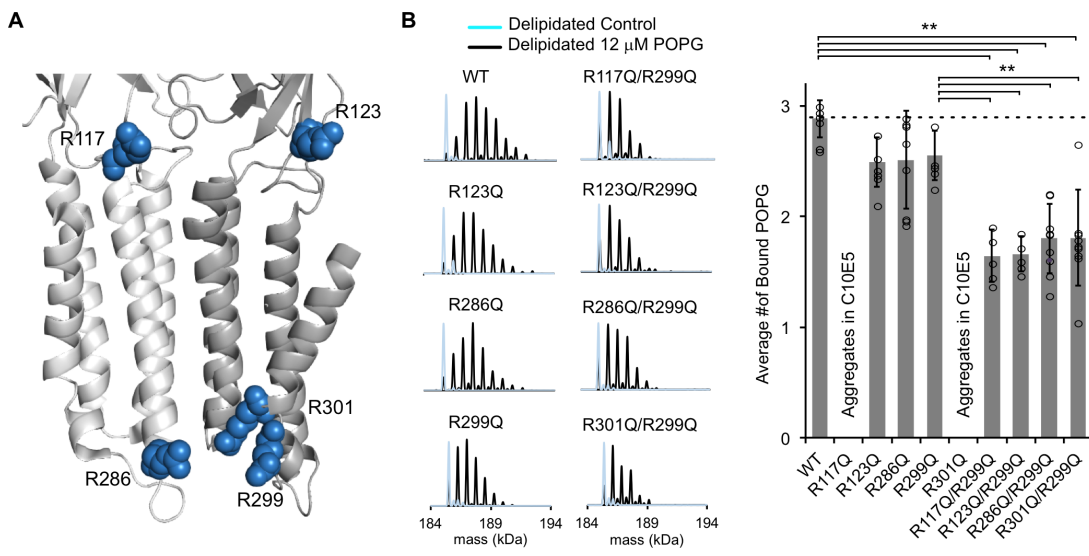


Figure 4.6: Mutations of five interfacial arginines reduce POPG binding.(A) Structure of ELIC showing two adjacent subunits and five arginine side chains that were mutated to glutamine. (B) Left: Representative deconvoluted spectra of ELIC WT and indicated mutants. Blue indicates spectra of delipidated ELIC in C10E5. Black indicates spectra of delipidated ELIC in C10E5 with 12 μ M POPG. Right: Plot of average number of bound POPG for ELIC WT and mutants, delipidated in C10E5, with 12 μ M POPG (n=5-8, \pm SD, **p<0.01).

R299Q by 27-32% (Fig. 4.6B). These results indicate that each interfacial arginine contributes approximately equally to POPG binding in ELIC. It is likely that significant decreases in binding could only be appreciated in the double mutants because of the variability in the data.

We further examined these sites of interaction using our coarse-grained MD simulations. To identify whether boundary POPG were localized around specific helices or residues, two-dimensional densities of the negatively-charged headgroup bead were calculated. The distributions are separated by leaflet where each leaflet contained 10% POPG. As shown in Fig. 4.7A, POPG was more likely to interact with ELIC in the inner leaflet than the outer leaflet, consistent with three out of five interfacial arginines residues being located on the intracellular interface of the ELIC TMD. These three arginines are located on TM3 (R286) and TM4 (R299 and R301). Contacts between POPG and all three of these residues are also visible in individual frames of the simulation (Fig. 4.7B). Moreover, POPG is more likely to be contacting the interfacial residues in TM4 (such as R299 and R301) than accessible interfacial residues in any other helices (Fig. 4.7A). The remaining two arginine residues are located at the TMD-ECD interface (R117 and R123). POPG density in the outer leaflet localized to these residues at intrasubunit sites between TM4 and TM1 or TM4 and TM3 (Fig. 4.7A), and contacts between these residues and POPG headgroups in the outer leaflet were also observed in snapshots from the MD simulations (Fig. 4.7B). In summary, the native MS data and coarse-grained MD simulations demonstrate that five interfacial arginines contribute to specific POPG binding sites in the inner and outer leaflets adjacent to TM4.

4.3.4 Specific interfacial arginines mediate POPG effect

Having established that ELIC selectively binds POPG over neutral phospholipids, and that binding is mediated by five interfacial arginines, we examined the role

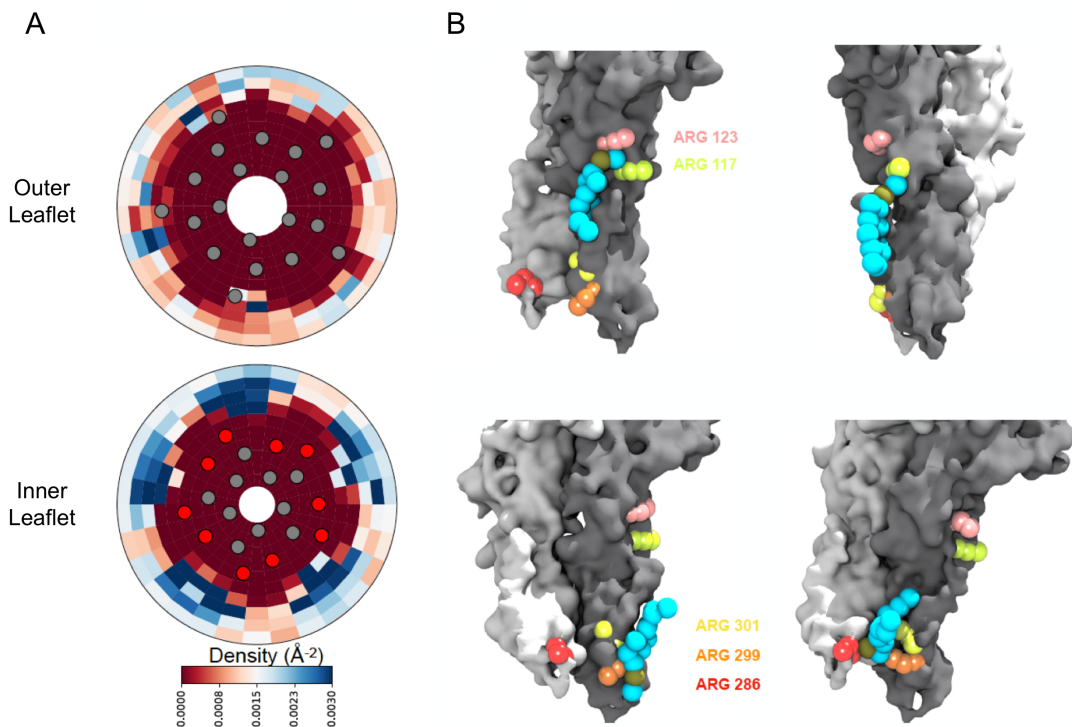


Figure 4.7: Density calculations of lipids in binary membranes and visualization of direct POPG-ELIC interactions at 10% POPG. (A) Distribution of POPG density in a POPG-POPC membrane, within 40 Å from the ELIC pore over the last half of a 15 μ s simulation, for both the outer leaflet (top) and the inner leaflet (bottom). Density is colored according to the color bar, where red and blue represent low and high POPG density, respectively. Circles represent the ELIC transmembrane backbone center of mass, with the helices containing the interfacial arginines colored in red (B) Representative frames after 9 μ s of simulation, showing multiple POPG binding modes associated with high density areas in (A). Two adjacent subunits of ELIC are shown in grey and white, while arginine side chains of interest are colored in peach, lime-yellow, orange, yellow, and red. POPG phosphate is colored in tan with the rest of the lipid in cyan.

of these binding sites on ELIC desensitization. We reconstituted each single mutant into giant liposomes composed of a 2:1:1 ratio of POPC:POPE:POPG (25% POPG) to test channel function by excised patch-clamping. We hypothesized that since increasing mole% POPG decreases ELIC desensitization, certain arginine mutants, which disrupt POPG binding, may increase ELIC desensitization. Indeed, all five single arginine mutants showed variable increases in the rate or extent of desensitization; however, these differences were generally small and statistically insignificant except for R301Q (Fig. 4.8, Fig. 4.9). We also tested the double mutants, which showed significant decreases in POPG binding. Three double mutants (R117Q/R299Q, R123Q/R299Q, R301Q/R299Q) showed a significant increase in the extent of desensitization while two (R117Q/R299Q, R301Q/R299Q) also showed a significant increase in the rate of desensitization (Fig. 4.8, Fig. 4.9). The effects observed in the double mutants approximate the sum of effects observed in the single mutants. Only R286Q/R299Q did not affect the extent or rate of desensitization (Fig. 4.8, Fig. 4.9). The EC₅₀ of cysteamine response and activation kinetics were also measured for all mutants; only R117Q and R117Q/R299Q showed significantly lower EC₅₀ and activation tau values compared to WT (Fig. 4.9, Fig. C7). Overall, these data indicate that four of five interfacial arginine residues that reduce POPG binding (i.e. R117, R123, R299, R301) also increase the rate and/or extent of ELIC desensitization.

4.3.5 L240A reduces desensitization and enhances POPG binding

If mutations that disrupt POPG binding increase receptor desensitization, then a mutation that decreases desensitization may enhance POPG binding. Mutation of a conserved pore-facing 9' TM2 leucine residue is known to slow desensitization in ELIC (L240A) (36) and other pLGICs. To confirm this finding in our system, we

reconstituted ELIC L240A into giant liposomes for patch-clamping and observed a significant reduction in the extent and rate of desensitization (Fig. 4.10A). To examine POPG binding, L240A was then de-lipidated in C10E5 for native MS. Interestingly, L240A significantly increased POPG binding compared to WT at 12 μ M POPG (\sim 1.7x increase in average number of POPG bound) (Fig. 4.10B).

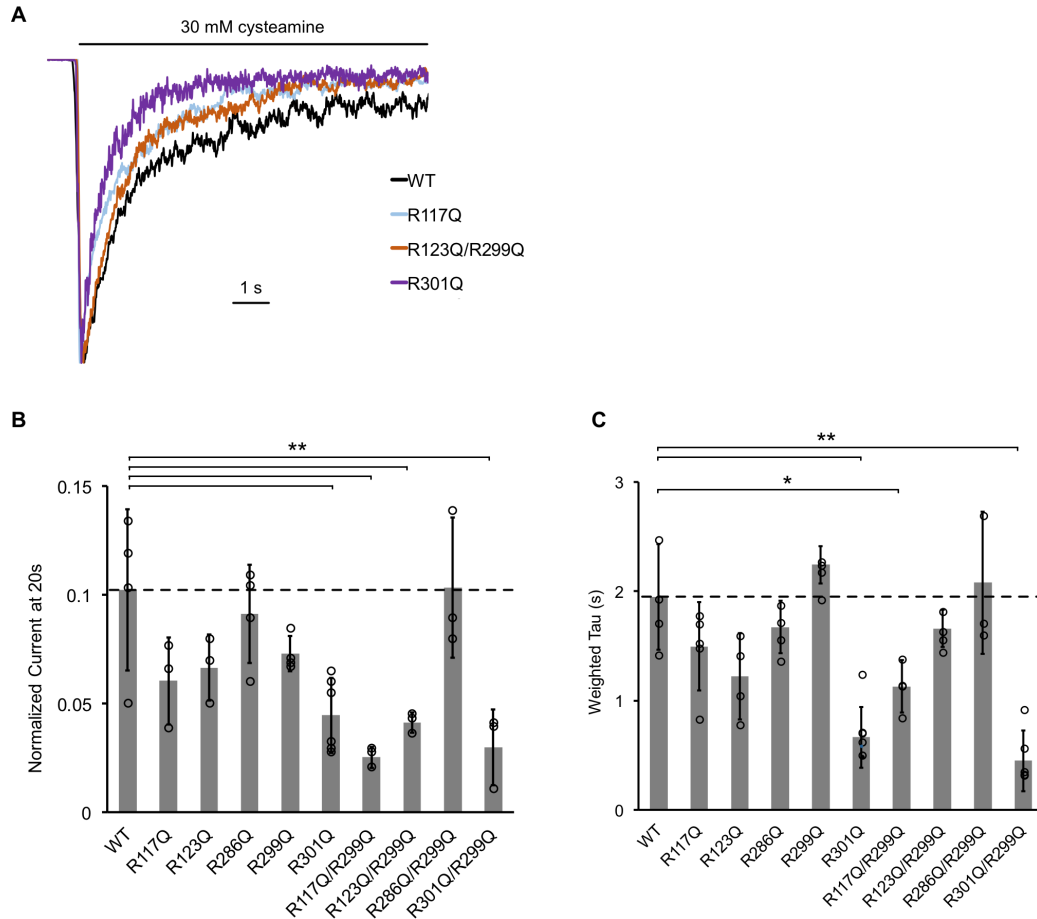


Figure 4.8: The effect of ELIC mutants on desensitization. (A) Normalized ELIC WT and mutant current responses to 30 mM cysteamine in 25% POPG liposomes. (B) Graph of ELIC WT and mutant currents 20 s after application of 30 mM cysteamine normalized to peak response in 25 mole% POPG liposomes ($n=3-7$, $\pm SD$, $^{**}p<0.01$, $^*p<0.05$). (C) Same as (B) for weighted tau (time constants) of desensitization.

4.4 Discussion

Recent structural and computational evidence suggests that lipids bind to pLGICs at specific sites within the TMD (24, 25, 39-41). However, there is a scarcity of evidence showing that changes in direct lipid binding are correlated with functional effects (25). We show that the anionic phospholipid, POPG, selectively binds to ELIC using native MS, thermally stabilizes the channel, and decreases receptor desensitization. Overall, these data support the idea that lipid binding directly affects receptor stability and function. Further, mutations of arginine residues that reduce POPG binding also increase ELIC desensitization to varying degrees. While it is possible that these arginine mutations increase desensitization through a mechanism other than their effect on POPG binding, the correlation between binding and desensitization, and the finding that the L240A mutation, which reduces desensitization, increases POPG binding affinity supports this conclusion. Remarkably, the L240A mutation, which is located in the channel pore and remote from the lipid interface (Fig. 4.11), appears to allosterically alter the affinity of ELIC for POPG. It is expected that a mutation that stabilizes a higher affinity state of the receptor (e.g. active over desensitized) would also enhance binding. Lipids may modulate ion channel activity through indirect effects on the physical properties of the membrane or through direct binding interactions (42, 43). The lipid binding data presented in this study using native MS provides evidence that direct binding of anionic phospholipids allosterically stabilizes the open state of a pLGIC relative to the desensitized state.

Membrane proteins including pLGICs are thought to determine their lipid microenvironment by specific binding interactions (28, 44). Our native MS measurements provide unique insights into phospholipid interaction with a pLGIC. First, we find that more POPG binds to ELIC compared to POPE or POPC at equivalent concentrations, suggesting that POPG binds to ELIC with higher

	Desensitization		Activation	Cysteamine Response
	Weighted τ (s)	Norm Current at 20s	τ (ms)	EC ₅₀ (mM cysteamine)
WT	1.95 ± 0.48	0.100 ± 0.041	134 ± 50	5.1 ± 1.2
R117Q	1.49 ± 0.40	0.060 ± 0.020	54 ± 40 *	3.3 ± 0.9 *
R123Q	1.20 ± 0.39	0.067 ± 0.015	112 ± 65	3.7 ± 0.9
R286Q	1.67 ± 0.24	0.091 ± 0.023	106 ± 34	4.3 ± 0.4
R299Q	2.2 ± 0.17	0.074 ± 0.008	71 ± 27	4.7 ± 0.3
R301Q	0.66 ± 0.28 **	0.045 ± 0.017 **	72 ± 15	5.2 ± 0.8
R117Q/R299Q	1.13 ± 0.24 *	0.025 ± 0.004 **	54 ± 26 *	2.4 ± 0.7 **
R123Q/R299Q	1.66 ± 0.17	0.041 ± 0.005 **	74 ± 35	3.7 ± 0.6
R286Q/R299Q	2.08 ± 0.65	0.103 ± 0.032	92 ± 27	4.7 ± 1.5
R301Q/R299Q	0.45 ± 0.28 **	0.030 ± 0.017 **	71 ± 21	3.9 ± 0.9

Figure 4.9: ELIC WT and mutant channel properties in giant liposomes composed of 25 mole% POPG (n=3-7, ±SD). Shown are weighted time constants (τ) for desensitization and currents 20 s after application of 30 mM cysteamine normalized to peak response. Also shown are activation time constants and EC₅₀ of cysteamine response. Light gray indicates mutant values which are significantly different from WT (dark gray) (** p<0.01, * p<0.05).

affinity. This is supported by enrichment of POPG compared to POPE in phospholipids that are co-purified with ELIC, and coarse-grained simulations which show enrichment of POPG among the boundary phospholipids of ELIC. Second, native MS also allows determination of the stoichiometry and sites of lipid binding (32, 45). By relating binding stoichiometry and thermal stability, the data estimate that 32 POPG lipids, which is the average predicted number of annular lipids in ELIC from MD simulations, results in greater than 80% of the stabilizing effect against thermal denaturation (Fig. C5), suggesting that maximal thermal stability is achieved when the entire ELIC transmembrane domain (TMD) is surrounded by POPG. Although five interfacial arginine residues were identified to contribute to POPG binding in ELIC (25 arginines total), it is conceivable that each arginine side chain may interact with more than one phospholipid headgroup or that other sites exist.

To quantify the effect of the ELIC double mutants on specific POPG binding

sites, we also fit the native MS binding data for the double mutants to a binomial binding model using the dissociation constant for POPG binding to WT and varying the number of available sites. POPG binding to the double mutants was best fit with a reduction in the number of available sites from 32 in WT to 18-21 in the mutants (Fig. C4). Given the ~35-45% decrease in bound phospholipid with each double mutant (mutation of two out of five arginines), we conclude that phospholipid binding at these residues constitute the highest affinity sites. This is indeed consistent with the POPG densities from the coarse-grained simulations, which show discrete enrichment of POPG lipids adjacent these residues. Disruption of binding sites by mutation of these arginines may not prevent the occupancy of lipids at these sites per se, but may alter the lipid binding modes or occupancy times at these sites.

Previous studies examining the effects of lipids on pLGIC function found that nAChR and ELIC are inactive in POPC-only membranes (6, 15, 30), and it was proposed that this is due to uncoupling of agonist binding to channel activation (46). To examine ELIC channel activity in liposomes lacking anionic phospholipid, we utilized a stopped-flow flux assay, and demonstrated cysteamine-elicited flux by ELIC in POPC-only liposomes. The high sensitivity of this assay may be the reason ELIC activity could be detected, contrary to a prior study in which ELIC in POPC liposomes were injected into *Xenopus* oocytes (30). However, the ELIC activity was significantly decreased compared to POPC:POPE:POPG (2:1:1) liposomes. The low protein concentration used in this assay does not allow us to assess the reconstitution efficiencies. Thus, the overall lower flux rates and smaller amplitudes in POPC could stem from lower protein reconstitution. However, the faster desensitization kinetics in POPC liposomes can be resolved reliably, and are consistent with the patch-clamp measurements. The results substantiate the role of POPG in stabilizing the open state relative to the desensitized state, and demonstrate the utility of measuring pLGIC activity

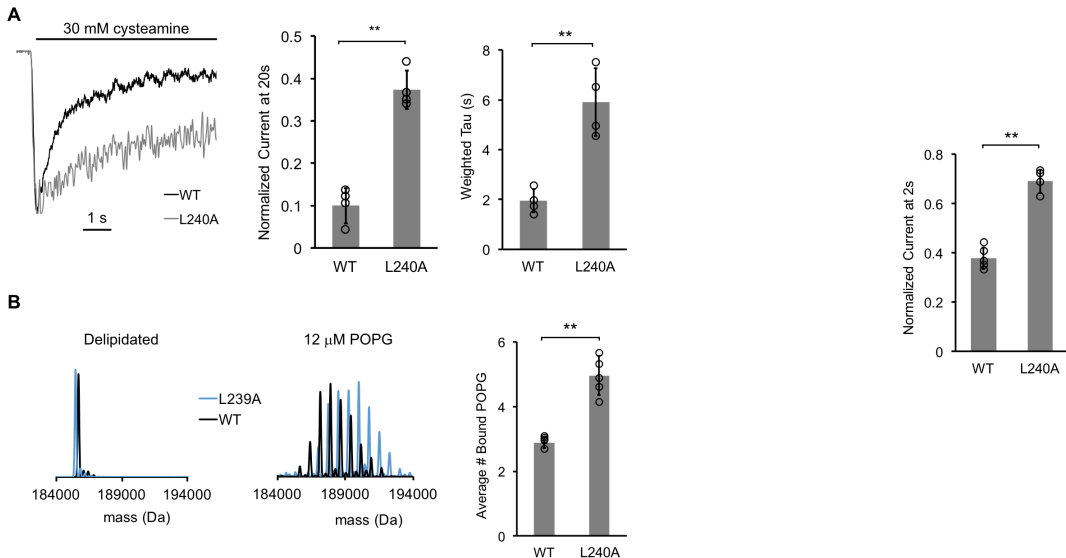


Figure 4.10: The L240A mutant decreases desensitization and increases POPG binding. (A) Left: Normalized ELIC WT and L240A current responses to 30 mM cysteamine in 25% POPG liposomes. Middle: ELIC WT and L240A currents 20 s after application of 30 mM cysteamine normalized to peak response at 25 mole% POPG ($n=4-5$, $\pm SD$, $**p<0.01$). Right: Weighted tau (time constants) of ELIC WT and L240A desensitization time courses at 25 mole% POPG ($n=4-5$, $\pm SD$, $**p<0.01$). (B) Left: Representative deconvoluted spectra of ELIC WT (black) and L240A (blue) showing ELIC delipidated in C10E5 without and with 12 μ M POPG. Right: Graph of average number of bound POPG for ELIC WT and L240A, delipidated in C10E5, with 12 μ M POPG ($n=4-5$, $\pm SD$, $**p<0.01$).

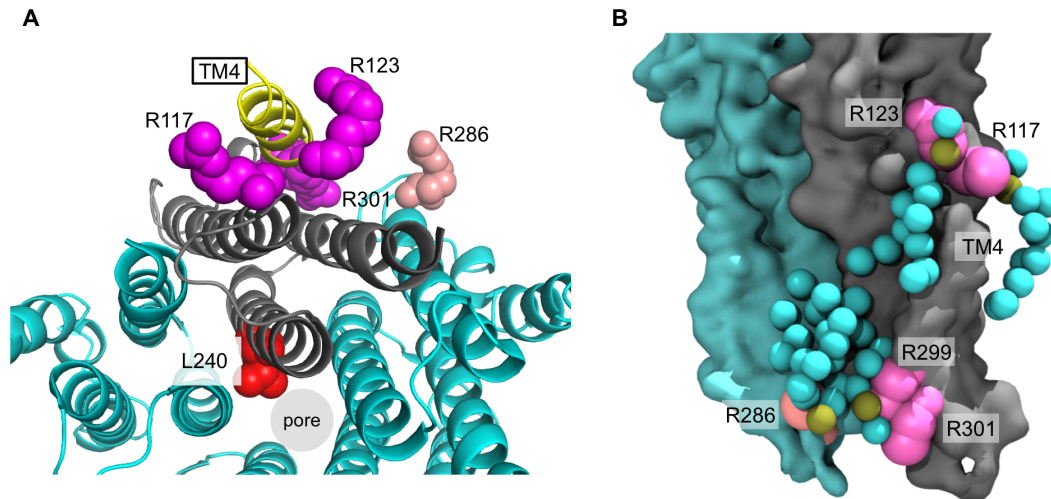


Figure 4.11: Arginines involved in POPG binding and ELIC desensitization. (A) Top view of ELIC highlighting TM4 (yellow) and showing the side chains of R117, R123 and R301 (magenta) adjacent to TM4, which increase ELIC desensitization, and R286 at the subunit interface (salmon), which has no effect on desensitization. L240 (red) faces the pore. (B) Image from coarse-grained simulations with 50% POPG showing two adjacent ELIC subunits and the mutated arginine side chains (R117, R123, R299 and R301 in magenta; R286 in salmon). Also, shown are all POPG lipids making contacts with the TMD in this snapshot.

in liposomes of defined lipid composition using complementary patch-clamp and stopped-flow flux techniques.

While pLGICs are known to be sensitive to their lipid environment, the binding sites that mediate lipid modulation are not well defined. It has been proposed that TM4 is a lipid sensing structure in pLGICs due to its proximity to the lipid membrane and sensitivity to mutagenesis (41, 47-49). Furthermore, crystal structures of GLIC show bound lipids within intrasubunit grooves between TM4-TM1 and TM4-TM3 (23), which have been proposed to be important determinants of channel opening (24, 25). Photolabeling studies have also identified intra-subunit neurosteroid binding sites adjacent to TM4 that mediate neurosteroid

modulatory effects (50, 51). We show that POPG binding at multiple interfacial arginine residues, including R117, R124, R299 and R301 which are localized to the extracellular and intracellular sides of TM4 (Fig. 4.11), are likely important in mediating the effect of POPG on ELIC desensitization. Examination of boundary POPG from coarse-grained simulations with high POPG mole% (50%) at 15 μ s shows POPG headgroups making contacts with all of these arginine side chains, and illustrates potential binding modes for the acyl chains (Fig. 4.11B). For example, boundary POPG with headgroups that interact with R301 or R299 have acyl chains that make contacts with intrasubunit sites along the intracellular side of TM4 (Fig. 4.11B and 5B). R301, which has the largest effect on desensitization when mutated, is conserved among many mammalian pLGICs including GABA_AR and nAChR isoforms, and R299 is adjacent to R301 at the bottom of TM4. Mutations in this region of TM4 have profound effects on pLGIC desensitization (48, 49, 52, 53). R117 and R123 are located at the extracellular end of TM4, and boundary POPG with headgroups that interact with these residues have acyl chains that make contacts with intrasubunit sites on both sides of TM4 (Fig. 4.11B and 5B). Sites equivalent to R117 and R123 in GLIC were previously found to be occupied by a phospholipid and docosahexaenoic acid (DHA), respectively (24, 25). The polyunsaturated fatty acid, DHA, was found to increase desensitization in GLIC (25). Therefore, it is possible that the exact lipid structure occupying these sites results in different effects. Our results raise the hypothesis that lipids with polyunsaturated acyl chains or certain sterols (54) exert the opposite effect of activating phospholipids by acting as competitive antagonists.

In summary, the anionic phospholipid, POPG, decreases desensitization in the pLGIC, ELIC. POPG specifically binds to and stabilizes ELIC by interacting with interfacial arginine residues. Our results strongly suggest that binding of POPG at specific sites modulates receptor desensitization.

4.5 Methods

4.5.1 Mutagenesis, expression and purification of ELIC

pET26-MBP-ELIC was a gift from Raimund Dutzler (Addgene plasmid # 39239) and was used for WT ELIC expression and generation of mutants. Site-directed mutagenesis was performed by the standard Quikchange approach, and confirmed by Sanger sequencing (Genewiz, Plainfield, NJ). WT and mutant ELIC was expressed as previously described (25, 55) in OverExpressTM C43 (D3) *E. coli* (Lucigen, Middleton, WI). Cultures were grown in Terrific Broth (Sigma, St. Louis, MO) and induced with 0.1 mM IPTG for ~16 hours at 18 °C. Pelleted cells were resuspended in Buffer A (20 mM Tris pH 7.5, 100 mM NaCl) with cOmplete EDTA-free protease inhibitor (Roche, Indianapolis, IN), and lysed using an Avestin C5 emulsifier at ~15,000 psi. Membranes were collected by ultracentrifugation, resuspended in Buffer A, solubilized in 1 % DDM (Anatrace, Maumee, OH), and incubated with amylose resin (New England Biolabs, Ipswich, MA) for 2 hours. The resin was washed with 20 bed volumes of Buffer A, 0.02% DDM, 0.5 mM tris(2-carboxyethyl)phosphine (TCEP) and 1 mM EDTA, and eluted with Buffer A, 0.02% DDM, 0.05 mM TCEP, and 40 mM maltose. Eluted protein was digested overnight with HRV-3C protease (Thermo Fisher, Waltham, MA) (10 units per mg ELIC) at 4 °C, and injected on a Sephadex 200 10/300 (GE Healthcare Life Sciences, Pittsburgh, PA) size exclusion column in Buffer A, 0.02% DDM.

4.5.2 Native MS measurements

Native MS analysis was similar to previous descriptions for other membrane proteins (27). For analysis of ELIC in DDM, 30 μ l of purified protein in 0.02% DDM at ~1 mg/ml was buffer exchanged into 200 mM ammonium acetate pH

7.5 and 0.02% DDM using Biospin 6 gel filtration spin columns (Bio-Rad, Hercules, CA). 2 μ l of buffer exchanged ELIC was loaded into a borosilicate capillary emitter (Thermo Scientific, Waltham, MA), and analyzed by static nanospray on a Thermo QExactive EMR mass spectrometer. The following parameters were used to resolve the ELIC pentamer and minimize dissociation into tetramer and monomer: capillary voltage of 1.2 kV, capillary temperature of 200 °C, ion transfer optics set with the injection flatapole, inter-flatapole lens, bent flatapole, transfer multiple as 8, 7, 6, 4 V, respectively, resolution 8,750, AGC target 3 x 10⁶, trap pressure set to maximum, CID 200 V, and CE 100 V. For analysis of ELIC in C10E5, ELIC delipidated by injecting 300 μ g onto a Sephadex 200 10/300 column (GE Healthcare) at 0.5 ml/min pre-equilibrated with Buffer A, 10% glycerol, and 0.06% C10E5 (Anatrace). 30 μ l aliquots were then buffer exchanged to 100 mM ammonium acetate pH 7.5, 0.06% C10E5 using Biospin 6 columns, and diluted to 0.2 mg/ml. MS measurements on the QExactive EMR were performed with the parameters listed above except: capillary temperature 100 °C, CID 75 V and CE 200 V. For lipid binding measurements, stocks of POPG lipid were prepared at 2x the concentration of POPG being tested in 100 mM ammonium acetate pH 7.5 and 0.06% C10E5. Lipid stocks were then mixed with 0.4 mg/ml ELIC in a 1:1 volume ratio for a final concentration of 1 μ M ELIC, and samples were analyzed after >5 min incubation.

MS spectra were deconvoluted using UniDec (56); deconvolution of spectra with bound lipid was restricted to the +26 to +22 charge states (Fig. C3). Peak heights of apo and lipid-bound species were extracted from UniDec, and analyzed by two approaches. The average number of bound lipids was determined by the following relationship:

$$\text{Average number bound lipid} = \frac{\sum_{n=0}^k n \cdot I_n}{\sum_{n=0}^k I_n} \quad (4.1)$$

where n is the number of bound lipids and I_n is the deconvoluted peak height of ELIC with n bound lipids. Peak heights of apo and lipid-bound species were

also plotted as mole fraction versus the number of bound lipids (Fig. C4). These data were fit with a binomial binding model, which assumes that there are N sites each with equal affinity, K. The probability, p, that a site is occupied at the concentration of a given lipid, A, is defined as:

$$p = \frac{[A]}{[A] + K} \quad (4.2)$$

Then, the probability (B) that q sites are occupied out of N total sites is given by the binomial probability function:

$$B(q) = \frac{N!}{q!(N-q)!} p^q (1-p)^{N-q} \quad (4.3)$$

B(q) was used to determine the mole fraction of each lipid-bound species at a given [A], which was used to fit the native MS data in Excel across all [A] by setting K constant and varying N or vice versa.

4.5.3 Thermal stability assay

Purified WT ELIC in C10E5 (Buffer A, 0.06% C10E5) was diluted to 1 μM in the absence or presence of various concentrations of phospholipid. Samples were analyzed without and with heating in the absence or presence of phospholipid. Analysis of protein thermal stability was performed by injecting 90 μl of sample on a size exclusion column (Sephadex 200 10/300), and measuring the amplitude of the pentamer peak as previously described (57, 58). Heating was performed for 15 min at 32 °C, which resulted in a ~85% decrease in the pentamer amplitude compared to 4°C. The stabilizing effect of a phospholipid was quantified as the pentamer amplitude in the presence of phospholipid (heated) divided by control (heated).

4.5.4 Excised patch-clamp recordings from giant liposomes

ELIC WT and mutants were reconstituted into giant liposomes as previously described with some modifications (59). Three liposome preparations were used in this study: 1) 25% POPG (consists of 50% POPC/ 25% POPE/ 25% POPG), 2) 12% POPG (consists of 60% POPC/ 28% POPE/ 12% POPG), and 3) 40% POPG (consists of 35% POPC/ 25% POPE/ 40% POPG). These liposome compositions were chosen to vary POPG mole% while optimizing lipid mixtures to obtain ideal giant liposomes for patch-clamping. This was achieved by varying POPG mole% and POPC mole% inversely. Condition #1 was used for WT and all mutants, and conditions #2 and #3 were used in WT. Liposomes were prepared by drying 15-20 mg of lipid mixtures in chloroform using N₂ in a round bottom flask and then overnight in a vacuum dessicator. Dried lipids were rehydrated at 5 mg/ml in 10 mM MOPS pH 7, and 150 mM NaCl (MOPS buffer), subjected to ten freeze-thaw cycles ten, and then small unilamellar liposomes were formed by extrusion using a 400 nm filter (Avanti Lipids, Alabaster, AL) and bath sonication (30 sec x 5). 5 mg of liposomes in 1 ml were destabilized by adding DDM to 0.2% and rotating for 1 hour at room temperature followed by 0.3-0.5 mg of ELIC WT or mutants at ~4-5 mg/ml and incubation for 30 min. To remove DDM, SM-2 Bio-beads (Bio-Rad) were added in five batches (30, 30, 50, 100, and 100 mg). The first three batches were added each hour along with 1 ml of MOPS buffer to make a final volume of 4 ml while rotating at room temperature. After adding the first 100 mg batch, the proteoliposomes were rotated overnight at 4 °C, followed by the last 100 mg the next day for 3 hours at room temperature. Proteoliposomes were harvested by ultracentrifugation at 150,000 x g for 1 hour at 4 °C, and the pellet resuspended with 80 µl of MOPS buffer for a lipid concentration of ~50 mg/ml. Giant liposomes were formed by drying 10 µl of proteoliposomes on a glass coverslip in a desiccator for 3-5 hours at 4 °C followed by rehydration with 60 µl of MOPS buffer overnight at 4 °C and at least

2 hours at room temperature the next day. Giant liposomes were resuspended by pipetting and then applied to a petri dish with MOPS buffer.

Patch-clamp recordings were performed using borosilicate glass pipettes pulled to $\sim 2 - 3 \text{ M}\Omega$ using a P-2000 puller (Sutter instruments, Novato, CA). Pipettes were filled with 10 mM MOPS pH 7, 150 mM NaCl, and 0.5 mM BaCl₂. Excised patches (the orientation of ELIC in the liposomes is not known; therefore, these patches are not defined as outside-out or inside-out) were held at -60 mV, and bath solutions consisted of 10 mM MOPS pH 7, 150 mM NaCl, 0.5 mM BaCl₂, 1 mM DTT, and varying concentrations of cysteamine. DTT was added to the bath solution to prevent cysteamine oxidation. Rapid solution exchange was achieved with a three-barreled flowpipe mounted and adjusted by to a SF-77B fast perfusion system (Warner Instrument Corporation, Hamden, CT). Liquid junction current at the open pipette tip demonstrated 10-90% exchange times of <10 ms. Data was collected at 20 kHz using an Axopatch 200B amplifier (Molecular Devices, San Jose, CA) and a Digidata 1322A (Molecular Devices) with Axopatch software, and a low pass Bessel filter of 10 kHz was applied to the currents. Analysis of currents was performed with Clampfit 10.4.2 (Molecular Devices). Activation currents were fit to a single exponential equation, and desensitization currents were fit to both single and double exponential equations. The majority of desensitization currents were best fit with a double exponential, and weighted time constants were derived using the following calculation:

$$Weighted\tau = \frac{(A1 \cdot \tau1) + (A2 \cdot \tau2)}{A1 + A2} \quad (4.4)$$

where A1 and A2 are the weighted coefficients of the first and second exponential components. The reported weighted average time constants are averages of weighted time constants from double exponential fits and time constants from single exponential fits. Peak cysteamine dose response curves were fit to a Hill equation, keeping n constant at 2, which provided a reasonable fit for all data

sets. All statistical comparisons were made using a one-way ANOVA with post-hoc Tukey HSD test.

4.5.5 Stopped-flow fluorescence recordings

The fluorescence-based sequential-mixing stopped-flow assay was carried out with an SX20 stopped-flow spectrofluorimeter (Applied Photophysics, Leatherhead, UK) at 25 °C. To reconstitute ELIC into large unilamellar vesicles (LUVs), 15 mg of lipids (POPC or POPC:POPE:POPG 2:1:1) were dried in glass vials to a thin film under a constant N₂ stream. Lipids were further dried under vacuum overnight. The next day, lipids were rehydrated in reconstitution buffer (1114 μ l of 15 mM Hepes, 150 mM NaNO₃, pH 7). 33 mg CHAPS were added stepwise while sonicating lipids in a bath sonicator until the solution was clear. 1057 μ l of a 75 mM ANTS stock solution (in ddH₂O, pH 7) was added together with purified ELIC (1 μ g/mg lipid), mixed and incubated for 20 min. Detergent removal was initiated by addition of 0.7 g SM-2 BioBeads (BioRad) in assay buffer (10 mM Hepes, 140 mM NaNO₃, pH 7). The reconstitution mix was incubated for 2.5 h at 21 °C under gentle agitation. The liposome-containing supernatant was transferred to a new glass tube and stored overnight at 13 °C. The liposome solution was sonicated in a bath sonicator for 30 s and extruded through a 0.1 μ m membrane (Whatman) using a mini-extruder (Avanti Polar lipids). Extra-vesicular ANTS were removed with a 10 ml desalting column (PD-10, GE Lifesciences). Right before the assay, liposomes were diluted 5-fold in assay buffer to ensure a good signal to noise ratio.

For the assay, ELIC-containing liposomes were mixed 1:1 with pre-mix buffer (assay buffer supplemented with 10 mM cysteamine to reach 5 mM after mixing) and incubated for defined amounts of time (10 ms – 25 s). A second 1:1 mixing step was performed with quenching buffer (10 mM Hepes, 90 mM NaNO₃, 50 mM TlNO₃, pH 7). ANTS fluorescence was excited at 360 nm and the integral

fluorescence above 420 nm was recorded for 1 s. For each delay time, at least 8 repeats under identical conditions were performed.

To analyze the data, each repeat was visually inspected and outliers were removed. Each remaining repeat was then fitted to a stretched exponential (Equation 4.1) and the rate of Tl⁺ influx was determined at 2 ms (Equation 4.2).

$$F_t = F_\infty + (F_0 - F_\infty) \cdot e^{\left\{-\left(\frac{t}{\tau}\right)^\beta\right\}} \quad (4.5)$$

$$k_t = \left(\frac{\beta}{\tau}\right) \cdot \left(\frac{2 \text{ ms}}{\tau}\right)^{(\beta-1)} \quad (4.6)$$

with F_t , F_∞ , F_0 being the fluorescence at time t , the final fluorescence and the initial fluorescence, respectively. t is the time (in s), τ the time constant (in s) and β the stretched exponential factor. k_t is the calculated rate (in s^{-1}) of Thallium influx at 2 ms.

The rate constants were averaged and the mean and standard deviations (S.D.) were determined and plotted (Fig 2F). The experiments were repeated for each lipid composition using three independent reconstitutions. The rates and S.D. were averaged and plotted as function of the delay time. The time course was fitted according to a double-exponential function to obtain the rates of activation and desensitization, respectively.

4.5.6 Lipid extraction and MS analysis

Lipids were extracted using a Bligh-Dyer extraction (60). Briefly, 100 μg of purified ELIC in DDM and 150 μg of *E. coli* membranes derived from cell cultures transformed and induced for ELIC expression, respectively, were mixed with 1 ml chloroform, 2 ml methanol and 0.8 ml water, and vortexed for 1 min, followed by an additional 1 ml chloroform and 1 ml water, and vortex for 3 min. The samples were centrifuged for 3 min at 500 $\times g$, and the lower organic phase removed for analysis, using a Thermo Scientific LTQ Orbitrap Velos mass spectrometer. Lipid extracts were loop injected (1.5 $\mu\text{l}/\text{min}$) using a syringe pump that delivered a

continuous flow of methanol at 15 $\mu\text{l}/\text{min}$ into the ESI source. High resolution ($R = 100,000$ at m/z 400) MS and MS/MS analyses were performed in negative ion mode. The skimmer of the ESI source was set at ground potential, electrospray voltage 4 kV, capillary temperature 300 °C, AGC target 5×10^4 , and maximum injection time 50 ms. MS^n experiments for identification of lipid structures were carried out with an optimized relative collision energy of 32%, activation q value of 0.25, activation time of 10 ms, and mass selection window of 1 Da.

4.5.7 Coarse-grained simulations of ELIC

All simulations reported here used the MARTINI 2.2 (61) coarse-grained topology and force field. The crystal structure of ELIC (PDB 3RQW) (62) was coarse-grained using MARTINI martinize.py script. Secondary structural restraints were constructed using martinize.py while imposed through Gromacs (63). Conformational restraints were preserved through harmonic bonds between backbone beads less than 0.5 nm apart with a coefficient of 900 kJ mol^{-1} . Pairs were determined using the ElNeDyn algorithm (64). Membranes were constructed using the MARTINI script insane.py (61). The insane.py script randomly places lipids throughout both inner and outer membranes and embeds selected proteins into the membrane. Two series of simulations were developed, the first using POPE and POPG, and the second POPC and POPG. Box sizes were about 30 x 30 x 25 nm³ and each simulation box contained about 3000 lipids.

Molecular dynamics simulations were carried out using GROMACS 5.1.4 (63). All systems were run using van der Waals (vdW) and electrostatics in cutoff and reaction-field, respectively, with a dielectric constant of $\epsilon = 15$. vdW and electrostatics used a cutoff length of 1.1 nm as defined in current MARTINI build specifications. Energy minimizations were performed for about 30,000 steps. All systems were run for short equilibration steps. Canonical ensembles (NVT) were run for 100 ps using Berendsen thermostat set to 323 K with the temperature

coupling constant set to 1 ps. Isothermal-Isobaric ensemble (NPT) equilibration was run for 5000 ps using Berendsen thermostat and barostat. The thermostat was set to 323 K with the temperature coupling constant set to 1 ps, and the barostat was set to a pressure coupling constant of 3 ps with a compressibility of 3×10^{-5} bar⁻¹ holding at 1 bar. Molecular dynamics were carried out using NPT ensemble and were simulated for 15 μ s with a time step of 0.015 ps using v-rescale thermostat set to 323 K and a temperature coupling constant of 1 ps. Membranes consisting of POPE used the Parrinello-Rahman barostat, and membranes consisting of POPC used the Berendsen barostat, both under semi-isotropic coupling. The reference pressure was set to 1 bar, the compressibility 3×10^{-4} bar⁻¹, and the pressure coupling constant 1 ps.

Annular lipids were determined using the annular lipid metric B:

$$B_i = \left\langle \frac{b_i}{b_{\text{tot}}} \right\rangle \frac{1}{x_i} - 1 \quad (4.7)$$

where b_i is the instantaneous number of boundary lipids of species i , b_{tot} is the instantaneous total number of boundary lipids, x_i is the overall (bulk) fraction of species i and the brackets represent an average over time and replicas. $B_i < 0$ and $B_i > 0$ indicate enrichment and depletion of species i , respectively, relative to the abundance in the bulk membrane. A given lipid was counted as a boundary lipid if it was within 6 Å of the ELIC transmembrane domain.

Two dimensional lipid density distributions around a central ELIC pentamer were calculated for each leaflet using polar coordinates (28). For every sampled frame, all lipids of species i were separated into leaflets. For all i lipids in a given leaflet, the vector separating the phosphate beads from ELIC center was calculated and projected onto the membrane plane. The two-dimensional separation vector was then used to assign the lipid to the appropriate polar bin of radial bin width 4 Å and angular bin width $\frac{\pi}{15}$. The area density in each bin was averaged over time and replicas.

Acknowledgements

We are grateful to Alex Evers, Joe Henry Steinbach, Christopher Lingle and Gustav Akk for helpful discussions and edits regarding this study and the preparation of the manuscript. We also acknowledge Arthur Laganowsky and Yang Liu for guidance with regard to sample preparation of ELIC for native MS measurements. We are indebted to Michael Gross at the Washington University NIH/NIGMS-supported biomedical mass spectrometry resource for use of the Thermo QExactive EMR mass spectrometer, and Christopher Lingle for use of a patch-clamp rig for electrophysiology recordings.

Competing Interests

The authors declare that no competing interests exist.

4.6 Reference

1. Corringer PJ, Poitevin F, Prevost MS, Sauguet L, Delarue M, Changeux JP. Structure and pharmacology of pentameric receptor channels: from bacteria to brain. *Structure*. 2012;20(6):941-56.
2. Allen JA, Halverson-Tamboli RA, Rasenick MM. Lipid raft microdomains and neurotransmitter signalling. *Nat Rev Neurosci*. 2007;8(2):128-40.
3. Baenziger JE, Henault CM, Therien JP, Sun J. Nicotinic acetylcholine receptor-lipid interactions: Mechanistic insight and biological function. *Biochim Biophys Acta*. 2015;1848(9):1806-17.
4. Rosenhouse-Dantsker A, Mehta D, Levitan I. Regulation of ion channels by membrane lipids. *Compr Physiol*. 2012;2(1):31-68.
5. Evers AS, Elliott WJ, Lefkowith JB, Needleman P. Manipulation of rat brain fatty acid composition alters volatile anesthetic potency. *J Clin Invest*.

1986;77(3):1028-33.

6. Criado M, Eibl H, Barrantes FJ. Functional properties of the acetylcholine receptor incorporated in model lipid membranes. Differential effects of chain length and head group of phospholipids on receptor affinity states and receptor-mediated ion translocation. *J Biol Chem.* 1984;259(14):9188-98.
7. Cheng WW, D'Avanzo N, Doyle DA, Nichols CG. Dual-mode phospholipid regulation of human inward rectifying potassium channels. *Biophys J.* 2011;100(3):620-8.
8. Chemin J, Patel AJ, Duprat F, Lauritzen I, Lazdunski M, Honore E. A phospholipid sensor controls mechanogating of the K⁺ channel TREK-1. *EMBO J.* 2005;24(1):44-53.
9. Hite RK, Butterwick JA, MacKinnon R. Phosphatidic acid modulation of Kv channel voltage sensor function. *Elife.* 2014;3.
10. Schmidt D, Jiang QX, MacKinnon R. Phospholipids and the origin of cationic gating charges in voltage sensors. *Nature.* 2006;444(7120):775-9.
11. Zolles G, Klocker N, Wenzel D, Weisser-Thomas J, Fleischmann BK, Roepke J, et al. Pacemaking by HCN channels requires interaction with phosphoinositides. *Neuron.* 2006;52(6):1027-36.
12. daCosta CJ, Medaglia SA, Lavigne N, Wang S, Carswell CL, Baenziger JE. Anionic lipids allosterically modulate multiple nicotinic acetylcholine receptor conformational equilibria. *J Biol Chem.* 2009;284(49):33841-9.
13. Hamouda AK, Sanghvi M, Sauls D, Machu TK, Blanton MP. Assessing the lipid requirements of the *Torpedo californica* nicotinic acetylcholine receptor. *Biochemistry.* 2006;45(13):4327-37.
14. daCosta CJ, Wagg ID, McKay ME, Baenziger JE. Phosphatidic acid and phosphatidylserine have distinct structural and functional interactions with the nicotinic acetylcholine receptor. *J Biol Chem.* 2004;279(15):14967-74.
15. Ochoa EL, Dalziel AW, McNamee MG. Reconstitution of acetylcholine

receptor function in lipid vesicles of defined composition. *Biochim Biophys Acta.* 1983;727(1):151-62.

16. Fong TM, McNamee MG. Correlation between acetylcholine receptor function and structural properties of membranes. *Biochemistry.* 1986;25(4):830-40.
17. Baenziger JE, Morris ML, Darsaut TE, Ryan SE. Effect of membrane lipid composition on the conformational equilibria of the nicotinic acetylcholine receptor. *J Biol Chem.* 2000;275(2):777-84.
18. Velisetty P, Chakrapani S. Desensitization mechanism in prokaryotic ligand-gated ion channel. *J Biol Chem.* 2012;287(22):18467-77.
19. Ellena JF, Blazing MA, McNamee MG. Lipid-protein interactions in reconstituted membranes containing acetylcholine receptor. *Biochemistry.* 1983;22(24):5523-35.
20. Mantipragada SB, Horvath LI, Arias HR, Schwarzmann G, Sandhoff K, Barrantes FJ, et al. Lipid-protein interactions and effect of local anesthetics in acetylcholine receptor-rich membranes from *Torpedo marmorata* electric organ. *Biochemistry.* 2003;42(30):9167-75.
21. Dreger M, Krauss M, Herrmann A, Hucho F. Interactions of the nicotinic acetylcholine receptor transmembrane segments with the lipid bilayer in native receptor-rich membranes. *Biochemistry.* 1997;36(4):839-47.
22. Antolini SS, Barrantes FJ. Disclosure of discrete sites for phospholipid and sterols at the protein-lipid interface in native acetylcholine receptor-rich membrane. *Biochemistry.* 1998;37(47):16653-62.
23. Bocquet N, Nury H, Baaden M, Le Poupon C, Changeux JP, Delarue M, et al. X-ray structure of a pentameric ligand-gated ion channel in an apparently open conformation. *Nature.* 2009;457(7225):111-4.
24. Prevost MS, Sauguet L, Nury H, Van Renterghem C, Huon C, Poitevin F, et al. A locally closed conformation of a bacterial pentameric proton-gated ion

- channel. *Nat Struct Mol Biol.* 2012;19(6):642-9.
25. Basak S, Schmandt N, Gicheru Y, Chakrapani S. Crystal structure and dynamics of a lipid-induced potential desensitized-state of a pentameric ligand-gated channel. *Elife.* 2017;6.
 26. Laganowsky A, Reading E, Allison TM, Ulmschneider MB, Degiacomi MT, Baldwin AJ, et al. Membrane proteins bind lipids selectively to modulate their structure and function. *Nature.* 2014;510(7503):172-5.
 27. Gault J, Donlan JA, Liko I, Hopper JT, Gupta K, Housden NG, et al. High-resolution mass spectrometry of small molecules bound to membrane proteins. *Nat Methods.* 2016;13(4):333-6.
 28. Sharp L, Salari R, Brannigan G. Boundary lipids of the nicotinic acetyl-choline receptor: Spontaneous partitioning via coarse-grained molecular dynamics simulation. *Biochim Biophys Acta Biomembr.* 2019;1861(4):887-96.
 29. Brannigan G. Direct Interactions of Cholesterol With Pentameric Ligand-Gated Ion Channels: Testable Hypotheses From Computational Predictions. *Curr Top Membr.* 2017;80:163-86.
 30. Carswell CL, Sun J, Baenziger JE. Intramembrane aromatic interactions influence the lipid sensitivities of pentameric ligand-gated ion channels. *J Biol Chem.* 2015;290(4):2496-507.
 31. Reading E, Liko I, Allison TM, Benesch JL, Laganowsky A, Robinson CV. The role of the detergent micelle in preserving the structure of membrane proteins in the gas phase. *Angew Chem Int Ed Engl.* 2015;54(15):4577-81.
 32. Liu Y, LoCaste CE, Liu W, Poltash ML, Russell DH, Laganowsky A. Selective binding of a toxin and phosphatidylinositides to a mammalian potassium channel. *Nat Commun.* 2019;10(1):1352.
 33. Nji E, Chatzikyriakidou Y, Landreh M, Drew D. An engineered thermal-shift screen reveals specific lipid preferences of eukaryotic and prokaryotic membrane proteins. *Nat Commun.* 2018;9(1):4253.

34. Zimmermann I, Marabelli A, Bertozzi C, Sivilotti LG, Dutzler R. Inhibition of the prokaryotic pentameric ligand-gated ion channel ELIC by divalent cations. *PLoS Biol.* 2012;10(11):e1001429.
35. Laha KT, Ghosh B, Czajkowski C. Macroscopic kinetics of pentameric ligand gated ion channels: comparisons between two prokaryotic channels and one eukaryotic channel. *PLoS One.* 2013;8(11):e80322.
36. Gonzalez-Gutierrez G, Lukk T, Agarwal V, Papke D, Nair SK, Grosman C. Mutations that stabilize the open state of the *Erwinia chrysanthemi* ligand-gated ion channel fail to change the conformation of the pore domain in crystals. *Proc Natl Acad Sci U S A.* 2012;109(16):6331-6.
37. Posson DJ, Rusinova R, Andersen OS, Nimigean CM. Stopped-Flow Fluorometric Ion Flux Assay for Ligand-Gated Ion Channel Studies. *Methods Mol Biol.* 2018;1684:223-35.
38. Lee SJ, Wang S, Borschel W, Heyman S, Gyore J, Nichols CG. Secondary anionic phospholipid binding site and gating mechanism in Kir2.1 inward rectifier channels. *Nat Commun.* 2013;4:2786.
39. Althoff T, Hibbs RE, Banerjee S, Gouaux E. X-ray structures of GluCl in apo states reveal a gating mechanism of Cys-loop receptors. *Nature.* 2014;512(7514):333-7.
40. Laverty D, Desai R, Uchanski T, Masiulis S, Stec WJ, Malinauskas T, et al. Cryo-EM structure of the human alpha1beta3gamma2 GABA_A receptor in a lipid bilayer. *Nature.* 2019;565(7740):516-20.
41. Carswell CL, Henault CM, Murlidaran S, Therien JPD, Juranka PF, Surujballi JA, et al. Role of the Fourth Transmembrane alpha Helix in the Allosteric Modulation of Pentameric Ligand-Gated Ion Channels. *Structure.* 2015;23(9):1655-64.
42. Cordero-Morales JF, Vasquez V. How lipids contribute to ion channel function, a fat perspective on direct and indirect interactions. *Curr Opin Struct*

Biol. 2018;51:92-8.

43. daCosta CJ, Dey L, Therien JP, Baenziger JE. A distinct mechanism for activating uncoupled nicotinic acetylcholine receptors. *Nat Chem Biol.* 2013;9(11):701-7.
44. Patrick JW, Boone CD, Liu W, Conover GM, Liu Y, Cong X, et al. Allostery revealed within lipid binding events to membrane proteins. *Proc Natl Acad Sci U S A.* 2018.
45. Habeck M, Kapri-Pardes E, Sharon M, Karlish SJ. Specific phospholipid binding to Na,K-ATPase at two distinct sites. *Proc Natl Acad Sci U S A.* 2017;114(11):2904-9.
46. daCosta CJ, Baenziger JE. A lipid-dependent uncoupled conformation of the acetylcholine receptor. *J Biol Chem.* 2009;284(26):17819-25.
47. Tobimatsu T, Fujita Y, Fukuda K, Tanaka K, Mori Y, Konno T, et al. Effects of substitution of putative transmembrane segments on nicotinic acetylcholine receptor function. *FEBS Lett.* 1987;222(1):56-62.
48. Bouzat C, Roccamo AM, Garbus I, Barrantes FJ. Mutations at lipid-exposed residues of the acetylcholine receptor affect its gating kinetics. *Mol Pharmacol.* 1998;54(1):146-53.
49. Li L, Lee YH, Pappone P, Palma A, McNamee MG. Site-specific mutations of nicotinic acetylcholine receptor at the lipid-protein interface dramatically alter ion channel gating. *Biophys J.* 1992;62(1):61-3.
50. Cheng WWL, Chen ZW, Bracamontes JR, Budelier MM, Krishnan K, Shin DJ, et al. Mapping Two Neurosteroid Modulatory Sites in the Prototypic Pentameric Ligand Gated Ion Channel GLIC. *J Biol Chem.* 2018.
51. Chen ZW, Bracamontes JR, Budelier MM, Germann AL, Shin DJ, Kathiresan K, et al. Multiple functional neurosteroid binding sites on GABA_A receptors. *PLoS Biol.* 2019;17(3):e3000157.
52. Domville JA, Baenziger JE. An allosteric link connecting the lipid-protein

- interface to the gating of the nicotinic acetylcholine receptor. *Sci Rep.* 2018;8(1):3898.
53. Lee YH, Li L, Lasalde J, Rojas L, McNamee M, Ortiz-Miranda SI, et al. Mutations in the M4 domain of *Torpedo californica* acetylcholine receptor dramatically alter ion channel function. *Biophys J.* 1994;66(3 Pt 1):646-53.
 54. Shen W, Mennerick S, Covey DF, Zorumski CF. Pregnenolone sulfate modulates inhibitory synaptic transmission by enhancing GABA(A) receptor desensitization. *J Neurosci.* 2000;20(10):3571-9.
 55. Hilt RJ, Dutzler R. X-ray structure of a prokaryotic pentameric ligand-gated ion channel. *Nature.* 2008;452(7185):375-9.
 56. Marty MT, Baldwin AJ, Marklund EG, Hochberg GK, Benesch JL, Robinson CV. Bayesian deconvolution of mass and ion mobility spectra: from binary interactions to polydisperse ensembles. *Anal Chem.* 2015;87(8):4370-6.
 57. Hattori M, Hibbs RE, Gouaux E. A fluorescence-detection size-exclusion chromatography-based thermostability assay for membrane protein precrystallization screening. *Structure.* 2012;20(8):1293-9.
 58. Miller PS, Scott S, Masiulis S, De Colibus L, Pardon E, Steyaert J, et al. Structural basis for GABAA receptor potentiation by neurosteroids. *Nat Struct Mol Biol.* 2017.
 59. Matulef K, Valiyaveetil FI. Patch-Clamp Recordings of the KcsA K(+) Channel in Unilamellar Blister. *Methods Mol Biol.* 2018;1684:181-91.
 60. Bligh EG, Dyer WJ. A rapid method of total lipid extraction and purification. *Can J Biochem Physiol.* 1959;37(8):911-7.
 61. de Jong DH, Singh G, Bennett WF, Arnarez C, Wassenaar TA, Schafer LV, et al. Improved Parameters for the Martini Coarse-Grained Protein Force Field. *J Chem Theory Comput.* 2013;9(1):687-97.
 62. Pan J, Chen Q, Willenbring D, Yoshida K, Tillman T, Kashlan OB, et al. Structure of the pentameric ligand-gated ion channel ELIC cocrystallized with its competitive antagonist acetylcholine. *Nat Commun.* 2012;3:714.

63. Van Der Spoel D, Lindahl E, Hess B, Groenhof G, Mark AE, Berendsen HJ. GROMACS: fast, flexible, and free. *J Comput Chem.* 2005;26(16):1701-18.
64. Periole X, Cavalli M, Marrink SJ, Ceruso MA. Combining an Elastic Network With a Coarse-Grained Molecular Force Field: Structure, Dynamics, and Intermolecular Recognition. *J Chem Theory Comput.* 2009;5(9):2531-43.

Chapter 5

Nicotinic Acetylcholine Receptor Boundary Lipid Characterization Within Native and Experimental Membranes

Pre-print <https://arxiv.org/abs/2102.02131>

5.1 Abstract

The nicotinic acetylcholine receptor (nAChR) and other pentameric ligand-gated ion channels (pLGICs) are native to neuronal membranes with an unusual lipid composition. While it is well-established that these receptors can be significantly modulated by lipids, the underlying mechanisms have been primarily studied in model membranes with only a few lipid species. Here we use coarse-grained molecular dynamics (MD) simulation to probe specific binding of lipids in a complex quasi-neuronal membrane. We ran a total of 50 microseconds of simulations of a single nAChR in a membrane composed of 36 species of lipids. Competition between multiple lipid species produces a complex distribution. We find that overall, cholesterol selects for concave intersubunit sites and PUFAs select for convex M4 sites, while monounsaturated and saturated lipids are unenriched in the nAChR boundary. In order to characterize binding to specific sites, we present a novel approach for calculating a “density-threshold affinity” from continuous density distributions. We find that affinity for M4 weakens with chain rigidity, which suggests flexible chains may help relax packing defects caused by

the conical protein shape. For any site, PE headgroups have the strongest affinity of all phospholipid headgroups, but anionic lipids still yield moderately high affinities for the M4 sites as expected. We observe cooperative effects between anionic headgroups and saturated chains at the M4 site in the inner leaflet. We also analyze affinities for individual anionic headgroups. Combined, these insights may reconcile several apparently contradictory experiments on the role of anionic phospholipids in modulating nAChR.

5.2 Introduction

The nicotinic acetylcholine receptor (nAChR) is a well studied excitatory pentameric ligand gated ion channel (pLGICs). nAChRs are found at high density in post-synaptic membranes and the neuromuscular junction in mammals, and the electric organ in *Torpedo* electric rays. The nAChR is activated by the binding of agonists such as nicotine or acetylcholine to the orthosteric site in the extracellular domain (ECD). When post-synaptic nAChRs are activated *en-mass* they stimulate an action potential. Thus nAChRs play a critical role in both cognition and memory[121] and neuromuscular function [183, 138]. nAChR and the greater pLGIC superfamily play various roles in neurological diseases related to inflammation [238, 195, 258, 95], addiction [74], chronic pain [253], Alzheimer's Disease [245, 201, 69, 138], spinal muscular atrophy [11], schizophrenia [120, 138] and neurological autoimmune diseases [154, 147].

nAChRs are highly sensitive to their local lipid environment. nAChR poorly conducts ions in model phosphatidylcholine (PC)-only membranes, but can conduct a current with the addition of cholesterol or anionic lipids [14, 86, 96, 80, 103, 102, 135, 236, 82, 14], though too much cholesterol can also cause a loss of function [80, 164, 20, 17]. Functional studies using *Xenopus* oocytes [260, 106, 61, 144, 187, 203, 181, 145] require lipid additives such as asolectin[80, 260, 106,

61, 187, 203, 181, 145] or lipids from synaptic membranes [71] to recover native levels of nAChR ion flux. Understanding the mechanism of modulation requires understanding how and where the modulating lipid interacts with the receptor, and these interactions may themselves be dependent upon the rest of the lipid composition.

Mammalian neuronal membranes [78, 237, 45, 128] have unique compositions compared to other mammalian membranes[173, 140, 244, 160, 129]. Neuronal membranes are more similar to the membrane of the *Torpedo* electric ray's electric organ [18, 208] than the average mammalian membrane[129]. The neuronal membrane [78, 237, 45, 128] is rich in lipids in which one or both chains are polyunsaturated fatty acids (PUFAs), particularly the *n* – 6 PUFA arachidonic acid (AA), and the *n* – 3 PUFAs docosahexaenoic acid (DHA) and eicosapentaenoic acid (EPA). These three PUFA's comprise ~ 20 – 25% of the acyl chains of neuronal phospholipids, and are involved in secondary signaling [175, 174] and neuronal development [162]. PUFAs are linked to a number of neurological diseases and disorders that overlap nAChR related diseases. PUFAs play a roll in major depressive and bipolar disorder [4, 174, 220, 143, 117], schizophrenia [197, 52, 29, 220, 162, 117], and Alzheimer's Disease [70, 91, 27, 4, 254, 98].

Functional experiments have focused on the role of anionic lipids and cholesterol as modulators of pLGICs [96, 103, 102, 135, 236, 82, 86, 3, 80] (the role of polyunsaturation has received comparatively little attention due to common challenges with oxidation of polyunsaturated chains). Such experiments have been overwhelmingly consistent with a role for direct binding of lipids as a modulatory mechanism. As for most membrane proteins, it is experimentally challenging to capture the boundary lipid composition of pLGIC because lipids are small molecules that may remain partly fluid even in their bound state. Numerous structures of pLGICs have revealed a conserved arrangement for both the TMD and the ECD. In the TMD, each subunit has four membrane helices (M1-M4) with

the five subunits forming a “star” shape around a central pore (Figure 5.1A). The M2 helix lines the pore, the M1 and M3 helices form a middle ring that includes the intersubunit cavities, and the M4 helices form the tip of the star. Structural methods have resolved potential cholesterol molecules[150, 49] and phospholipids [24, 122, 139] bound to subunit interfaces, but crystallographic disorder introduced by lipids typically precludes identification of lipid species. Mass spectrometry has revealed specific binding of anionic lipids, with additional mutagenesis studies suggesting localized sites in the inner leaflet near the M4 helices. [240]

Molecular dynamics (MD) simulations are particularly useful for visualizing and characterizing microscopic interactions within a fluid system. Given a putative cholesterol or lipid binding mode, atomistic simulations can be used to probe stability of the lipid binding mode. For pentameric channels, such approaches have primarily demonstrated stability of bound cholesterol[41], particularly at intersubunit sites[150, 123]. Unfortunately, fully atomistic simulations suffer from slow diffusion of lipids within the membrane, which prevents spontaneous lipid sorting by proteins over accessible simulation time scales.

Coarse-grained MD simulations use simplified molecular models that can reveal spontaneous lipid sorting, domain formation, and protein partitioning over simulation timescales [92, 60, 55, 130]. Coarse-grained MD simulations have been used previously to probe interactions of pLGICs with propofol[136] as well as spontaneous lipid binding in model membranes[225, 252, 240]. In previous work, we found that nAChR embedded in multiple domain-forming model membranes partitioned to the PUFA-rich liquid disordered domain[225], rather than to the cholesterol-rich liquid-ordered or “raft” domain that was suggested by cholesterol modulation. We observed that cholesterol still occupies embedded sites on the nAChR TMD, where it is shielded from the liquid disordered domain. However, native membranes are primarily composed of heteroacidic lipids with two distinct chains, where each chain has a different domain preference; such lipids will

naturally destabilize domains. In non-domain forming model membranes composed of heteroacidic lipids, two classes of five-fold symmetric sites emerged: an intersubunit site and the M4 site (Figure 5.1B). Cholesterol and saturated chains were enriched at the inter-subunit interfaces and n-3 PUFA acyl-chains were enriched around the M4 helices[252]. These results were consistent with binding to minimize packing defects: the rigid lipids could fill in the concave regions at the intersubunit sites while the flexible chains would easily deform around the “star points” of the M4 helices. Yet it was not clear whether these same patterns would be upheld in the more complex environment of a native neuronal membrane, which has many more options for minimizing any packing defect.

Neuronal membranes also contain a sizeable fraction of anionic lipids in the inner leaflet[78, 45, 237]. With collaborators in the Cheng lab, we recently[240] showed that anionic headgroups bind preferentially to the pLGIC *Erwinia* ligand-gated ion channel (ELIC), when the same acyl chains are used for both headgroups. Through coarse-grained MD, we found specific binding sites for 1-palmitoyl-2-oleoyl phosphatidylglycerol POPG in the intersubunit sites (inner leaflet); these sites contained basic amino acids that were also implicated through mutagenesis[240]. In nAChR the high-density of basic amino acids are in the M4 site (inner leaflet) rather than the intersubunit site (inner leaflet), so we would expect a shift for nAChR even in model membranes, due purely to the protein sequence. The relative roles of headgroup charge *vs* acyl chain saturation in driving affinity are unknown.

The use of complex quasi-realistic membranes in coarse-grained MD simulations is growing more feasible. In 2014, Ingólfsson et al[129] simulated an “average mammalian” membrane containing 63 lipid species, followed in 2017 by a coarse-grained neuronal membrane [128]. Multiple accessible and realistic membranes have been developed for comparison of protein-lipid interactions between model and quasi-native membranes[166, 251, 130, 55, 159]. To our knowledge,

no such coarse-grained MD simulations using quasi-native membranes have been used with pLGICs.

While the model membranes we used previously are useful for identifying putative sites, they have critical limitations. As stated previously, model membranes typically vary headgroup charge or acyl chain saturation, not both. Model membranes also do not allow for identification of more specific chemical variations within general saturation classes (i.e. n-3 PUFAs like DHA *vs* n-6 PUFAs like α -linolenic acid) or like-charged head groups (PC *vs* PE, or phosphoserine (PS) *vs* phosphoinositol (PI)). For this work, we embed the neuromuscular nAChR[242] in a coarse-grained neuronal membrane [128]. To test whether the predictions we developed from model membranes hold for native membranes, we develop a new method for quantifying affinities for partially-occupied binding sites.

The remainder of this paper is organized as follows. Section II presents our simulation and analysis approach, including introduction of the density-threshold affinity. Section III presents results and discussion of site selectivity of neutral lipids, followed by a reoriented discussion of the same data that is focused on lipid preferences of individual sites. We then consider selectivity of anionic lipids in the inner leaflet and finally consider the effects of specific headgroup differences. Section IV concludes.

5.3 Methods

5.3.1 Simulation Composition

All simulations used the coarse-grained MARTINI 2.2[90] topology and forcefield. nAChR coordinates were based on a cryo-EM structure of the $\alpha\beta\gamma\delta$ muscle-type receptor in native torpedo membrane (PDB 2BG9[242]). This is a medium resolution structure (4 \AA) and was further coarse-grained using the martinize.py script; medium resolution is sufficient for use in coarse-grained simulation, and

the native lipid environment of the proteins used to construct 2BG9 is critical for the present study. The secondary, tertiary and quaternary structure in 2BG9 was preserved via soft backbone restraints during simulation as described below, so any inaccuracies in local residue-residue interactions would not cause instability in the global conformation.

nAChR was embedded in a coarse-grained neuronal membrane based on Ingólfsson et al[128]. The neuronal membrane from described by Ingólfsson contains phospholipids, sterols, diacylglycerol, and ceramide. Membranes presented in this paper only consider phospholipids and cholesterol, for a total of 36 unique lipid species, see Table D1.

Coarse-grained membranes were built using the MARTINI script `insane.py` [247], which was also used to embed the coarse-grained nAChR within the membrane. The `insane.py` script randomly places lipids throughout the inter- and extra-cellular leaflets, and each simulation presented in this manuscript was built separately. All simulation box sizes were $40 \times 40 \times 35 \text{ nm}^3$ with $\sim 4,500 - 5,000$ lipids and total $\sim 450,000$ beads.

5.3.2 Simulations

Molecular dynamics simulations run using the MARTINI 2.2[90] forcefield and GROMACS[28, 2] 2019.2 . All systems used van der Waals (vdW) and Electrostatics with reaction-field and a dielectric constant of $\epsilon_r=15$ and electrostatic cutoff length at 1.1 nm. Energy minimization was performed for 1000000 steps, but energy minimization tended to concluded after $\sim 5000 - 10000$ steps.

Volume and pressure equilibrations were run with isothermal-isochoric (NVT) and isothermal-isobaric (NPT) ensembles respectively. NVT and NPT simulations used a time step of 15 fs and run for 0.3 ns using Berendsen thermostat held at a temperature of 323 K, and Berendsen pressure coupling with compressibility set to $3 \times 10^{-5} \text{ bar}^{-1}$ and a pressure coupling constant set to 3.0 ps for the NPT

ensemble.

Molecular dynamics simulations were run using a time step of 20 fs for 5 μ s for 10 replicas. Simulations were conducted in the NPT ensemble, by using the velocity rescaling to a temperature of 323 K with a coupling constant set to 1 ps. Semi-isotropic pressure coupling was set to Parrinello-Rahman with compressibility at 3×10^{-5} bar $^{-1}$ and pressure coupling constant set to 3.0 ps.

Secondary structures restraints with MARTINI recommendations were constructed by the martinize.py [90] script and imposed by GROMACS [28, 2]. The nAChR conformation was preserved by harmonic bonds between backbone beads separated by less than 0.5 nm and calculated using the ElNeDyn algorithm [200] associated with MARTINI [90] with a coefficient of 900 kJ·mol $^{-1}$.

5.3.3 Calculation of Polar Density Distributions

As in our previous work[225, 252, 240], the two-dimensional density distribution ρ_B of the beads within a given lipid species B around the protein was calculated on a polar grid:

$$\rho_B(r_i, \theta_j) = \frac{\langle n_B(r_i, \theta_j) \rangle}{r_i \Delta r \Delta \theta} \quad (5.1)$$

where $r_i = i\Delta r$ is the projected distance of the bin center from the protein center, $\theta_j = j\Delta\theta$ is the polar angle associated with bin j , $\Delta r = 10\text{\AA}$ and $\Delta\theta = \frac{\pi}{15}$ radians are the bin widths in the radial and angular direction respectively, and $\langle n_B(r_i, \theta_j) \rangle$ is the time-averaged number of beads of lipid species B found within the bin centered around radius r_i and polar angle θ_j . In order to determine enrichment or depletion, the normalized density $\tilde{\rho}_B(r_i, \theta_j)$ is calculated by dividing by the approximate expected density of beads of lipid type B in a random mixture, $x_B s_B N_L / \langle L^2 \rangle$, where s_B is the number of beads in one lipid of species B , N_L is the total number of lipids in the system, and $\langle L^2 \rangle$ is the average projected box

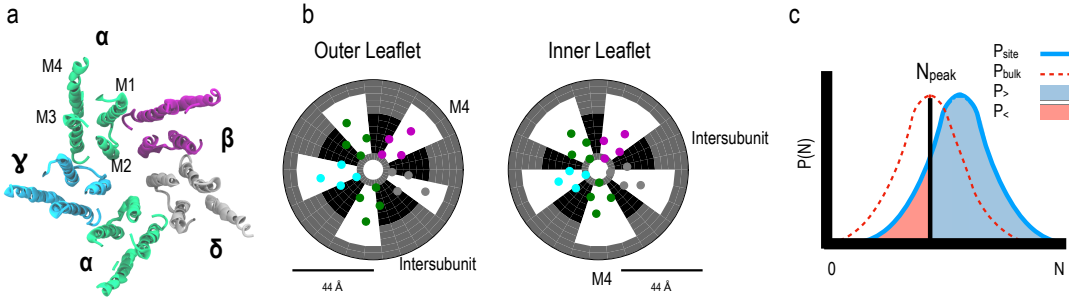


Figure 5.1: (a) Structure of the nAChRTMD[242], viewed from the extracellular domain. Helices are colored by subunit (α :green, β :purple, γ : cyan, δ :grey). (b) Boundaries of the pseudo-symmetric intersubunit (black) and M4 (white) sites. The angular components are determined by the location of the M1 and M3 alpha-helices for either two adjacent subunits (intersubunit sites) or a single subunit (M4 sites), and are listed in Table S5. Circles correspond to the helices shown in panel A. (c) The distributions $P_{site}(n)$ (blue) and $P_{bulk}(n)$ (dashed red) represent the probability distributions for number of beads of a certain lipid species in the site or in an analogously-sized area of the bulk, respectively. The value n_{peak} maximizes P_{bulk} . $P_<$ (pink) is the area under P_{site} to the right of n_{peak} while $P_>$ (light blue) is the area under P_{site} to the right of n_{peak} .

area:

$$\tilde{\rho}_B(r_i, \theta_j) = \frac{\rho_B(r_i, \theta_j)}{x_{BSB} N_L / \langle L^2 \rangle} \quad (5.2)$$

where the expected density is derived at the first frame of the simulation. Python software for these calculations are under active development and are located at [156].

This expression is approximate because it does not correct for the protein footprint or any undulation-induced deviations of the membrane area. The associated corrections are small compared to the membrane area and would shift the expected density for all species equally, without affecting the comparisons we perform here. For a given lipid species or class, analysis excluded any replicas in

which fewer than 5 lipids of the species/class were in the leaflet at any point in the sampled simulation.

5.3.4 Calculation of the density-threshold affinity

Although lipids to occupy clearly detectable hot-spots, binding to these sites are not straightforward to describe by a traditional two-state model. Lipids are chains that may partially occupy or fully occupy a site, and they may share a site with another lipid that is partly or fully occupying the site. While the standard affinity can be determined from the probability of single occupancy, the density-threshold affinity is determined from the probability that a site is occupied by more beads than would be expected based on bulk density.

For a given site, consider two probability distributions: the probability $P_{site}(n)$ of finding n beads within the site and the probability $P_{bulk}(n)$ of finding n beads within a region of equivalent area in the bulk, respectively. For a lipid that has no affinity for this binding site, we expect $P_{site}(n) = P_{bulk}(n)$, while $P_{site}(n)$ should be right-shifted for a strong affinity and left-shifted in the presence of competition. We calculate the degree of right or left shift by first finding the number of beads n_{peak} that corresponds to the peak of the density distribution in the bulk. As illustrated in Figure 5.1 C, we then integrate P_{site} on both the left and right side of the threshold n_{peak} to yield $P_<$ and $P_>$ respectively:

$$P_< \equiv \sum_{n \leq n_{peak}} P_{site}(n) \quad (5.3)$$

$$P_> \equiv \sum_{n > n_{peak}} P_{site}(n) \quad (5.4)$$

Note that this step breaks the distribution into two macrostates on either side of the threshold, allowing clear analogy with a classic binary binding model. The free energy difference between the two macrostates is

$$\Delta G = -RT \ln \frac{P_>}{P_<} \quad (5.5)$$

where R is the gas constant and T is temperature. We term this free energy difference the “density-threshold affinity”. In the special case of binary occupancy,

$$P_{site}(n) = \begin{cases} (1 + K_D/[L])^{-1}, & \text{if } n = 1 \\ (1 + [L]/K_D)^{-1}, & n = 0 \end{cases} \quad (5.6)$$

where K_D is the dissociation constant and $[L]$ is the ligand concentration. In a dilute solution the volume per ligand is typically much larger than the site volume, so $P_{bulk}(n) = 1$ for $n = 0$ and vanishes for all $n > 0$, so $n_{peak} = 0$. Consequently, for this special case, $P_< = (1 + [L]/K_D)^{-1}$ and $P_> = (1 + K_D/[L])^{-1}$. Then Equation 5.5 reduces to the classic form for the chemical potential $RT \ln K_D - RT \ln[L]$.

5.3.5 Binding Site Definition and Occupancy Calculations

We consider two classes of site: intersubunit sites and M4 sites. Each pLGIC has ten of each site (five in the outer leaflet and five in the lower leaflet) for a total of twenty sites (Figure 5.1B). The boundaries for each site were drawn to correspond to the localized binding hot spots observed for heteroacidic membranes[252], and are non-overlapping. Inter-subunit sites include bins with angular components between the M1 and M3 alpha-helices of two adjacent subunits, and a radial component satisfying $10 < r \leq 32\text{\AA}$. M4 sites include bins with complementary angular components (so that no sites overlap) falling within the M1 and M3 alpha-helices of a single subunit, and a radial component satisfying $10 < r \leq 44\text{\AA}$. For a full description of radial and angular dependencies, please see Table D4.1.

In order to calculate $P_{site}(n)$, a distribution was taken across frames at 10 ns intervals. For any frame, the beads of a given lipid or chain type were binned onto a fine polar grid with $\Delta r = 4\text{\AA}$ and $\Delta\theta = \frac{\pi}{25}$. The bins falling within the site boundaries were then summed to calculate the occupancy n . This approach allowed for straightforward adjustment of site boundaries if needed without needing

to re-bin the whole trajectory.

5.3.6 Calculation of Accessible Area

Calculation of P_{bulk} requires determining the accessible site area in order to calculate the densities in a bulk region of similar area. The area A accessible to the lipids is the difference between the total site area A_{tot} and the area A_{ex} excluded by the protein: $A = A_{tot} - A_{ex}$. A_{tot} is straightforward to calculate by summing over the areas of the bins i within the site boundaries: $A_{tot} = \sum_i r_i \Delta r_i \Delta \theta_i$. Calculating A_{ex} is less straightforward, and although there are many possible ways to do this, for self-consistency we used the same tools from our primary analysis.

In a single lipid membrane, $P_{site}(n) = P_{bulk}(n)$ as long as $P_{bulk}(n)$ is calculated using the proper area A . We exploit this identity to calculate A for each site, by running a single nAChR in pure di-palmitoyl phosphatidylcholine (DPPC) for ~ 370 ns and determining the value of A for each site such that $P_{site}(n)$ and $P_{bulk}(n)$ have the same peak. These areas are reported in Table D4.1.

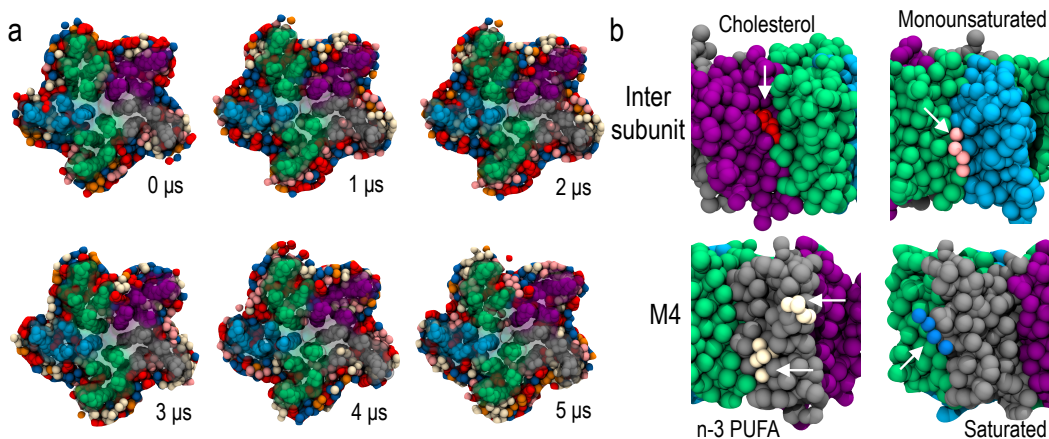


Figure 5.2: . a) Multiple frames from a single simulation replica over $5 \mu s$. The nAChR TMD is shown in surface representation and colored as in Figure 1. Cholesterol and acyl chains within 15 \AA of nAChR are shown as beads, and colored by chain type: saturated lipids: blue, monounsaturated lipids:orange, n-6 PUFA:s pink, n-3 PUFA:s beige, and cholesterol: red. Each phospholipid color includes several lipid species of the same type, and simulations included a larger membrane and the ECD, which is not shown. b) Representative poses of lipids for individual sites, colored as in A, but viewed from within the membrane looking at the TMD surface. Cholesterol selects for the intersubunit site while monounsaturated lipids have a particularly low affinity for this site. PUFA:s select for the M4 site, while saturated lipids have a particularly low affinity.

5.4 Results and Discussion

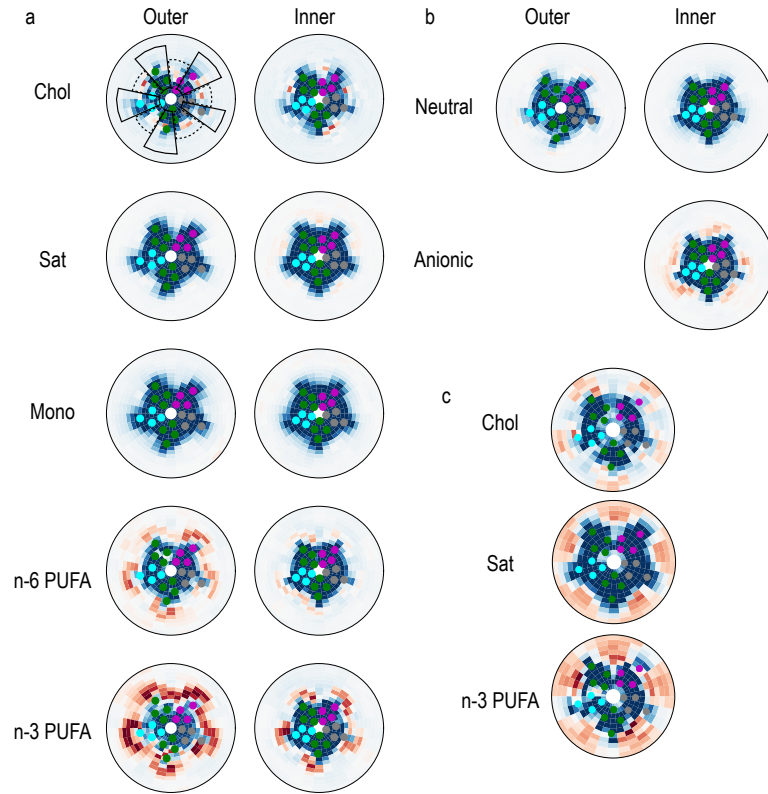


Figure 5.3: (a) and (b) Density enrichment $\tilde{\rho}_a$ for lipids in a neuronal membrane, calculated using eq 5.2 for both outer and inner leaflets, averaged over 10 replicas for $2.5 \mu\text{s}$ each. The maximum radius from the nAChR pore is 60 \AA . Depletion relative to a random mixture ($\log \tilde{\rho}_a < 0$) is blue while enrichment ($\log \tilde{\rho}_a > 0$) is red. Lipids are organized by acyl chain (a) or headgroup (b). Acyl chain density includes only the relevant chain of a heteroacidic lipid, while headgroup density includes the whole lipid. Helices are represented as circles colored as in Figure 1. Intersubunit (solid line) and M4 (dashed line) site boundaries are marked. (c) Equivalent analysis for nAChR in a model membrane of 2:2:1 n-3 PUFA:saturated:cholesterol, using previously published trajectories[252].

5.4.1 Effect of acyl chain on site selectivity among neutral lipids

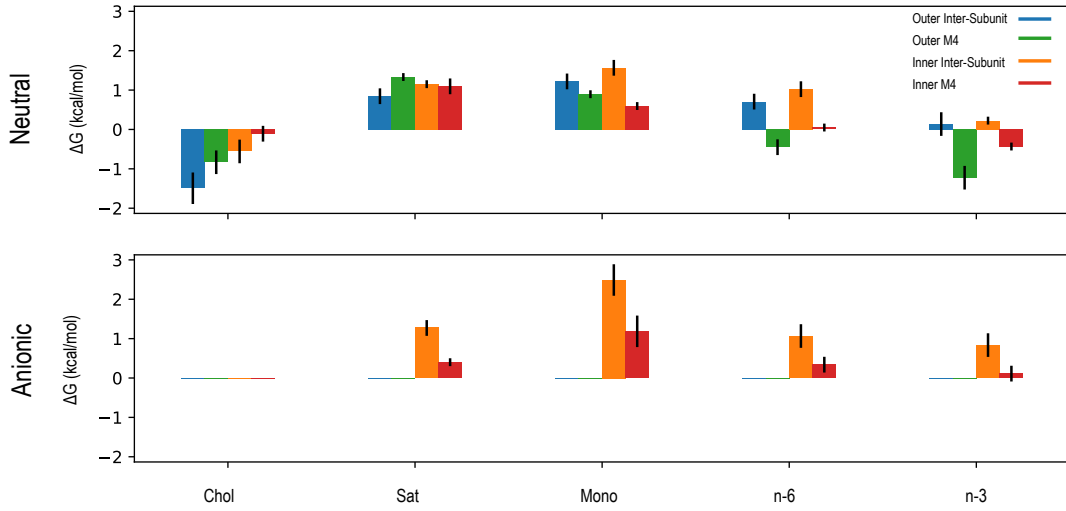


Figure 5.4: The density-threshold affinities(ΔG) are calculated using Equation 5.5, where error bars are the standard error ($n=10$ independent replicas). Density-threshold affinities are colored by site; in the outer leaflet: intersubunit (blue) and M4 (green), and for the inner leaflet: intersubunit (orange) and M4 (red). Values are separated by headgroup charge (rows) and acyl chain type (columns). More negative values indicate stronger affinities, while more positive values indicate more displacement of the lipid by other lipid species. Data incorporates 10 replicas averaging over the last half of the $5\mu s$ trajectory, with five-fold averaging over each type of pseudosymmetric site. Figure 5.5 has an alternate representation of the same data.

Representative frames from a typical trajectory of boundary lipids are shown in Figure 5.2A, with representative poses shown in Figure 5.2B. In order to quantitatively compare the lipid distributions for the native system to our previous model system, we plotted the enrichment of boundary density relative to bulk density on a two-dimensional polar heat map centered around the protein. This

enrichment is shown in Figure 5.3A for cholesterol and various acyl chains grouped by saturation. Saturated and monounsaturated acyl chains are not significantly depleted or enriched in the boundary of the protein. Regions of cholesterol density are much more localized than in the model membrane (Figure 5.3C) , with pockets of high enrichment very close to the protein and weak depletion in the remainder of the boundary region. Both n-6 and n-3 PUFA chains yield five-fold symmetric enrichment around the M4 alpha-helices, as observed for n-3 PUFAs in the model membrane. In the neuronal membrane, however, this enrichment is less well-defined and spreads into the intersubunit regions. In particular, additional pockets of significant enrichment are apparent in the $\beta - \delta$ subunit interface in the outer leaflet. The overall area of the regions of PUFA-enrichment decrease in the inner leaflet, where n-3 PUFAs are enriched around M4 helices, but n-6 PUFA density is not five-fold symmetric and has weak enrichment. Overall, the loss of definition in site boundaries diverges from the well-defined five fold enrichment for n-3 PUFAs we saw in model membranes[252].

In order to reduce these distributions to affinities that are more straightforward to interpret, we calculated the density-threshold affinity ΔG for various lipid species as defined in Eq. 5.5. We organize this information in two different ways: Figure 5.4 provides the “lipid’s perspective” and is organized to identify the preferred site for a given lipid type (the lipids’ “site selectivity”), while Figure 5.5 provides the “site’s perspective” and is organized to identify the most favorable lipids for a given site (the sites’ “lipid specificity”).

We first consider site selectivity for neutral lipids. Affinities for neutral lipids and cholesterol are shown in Figure 5.4A, where more negative values of ΔG indicate a stronger density-threshold affinity and more positive values indicate more displacement by other lipids. Overall, as shown in Figure 5.4A, saturated lipids have similar density-threshold affinities across all sites, which is consistent with the generally flat distribution observed in Figure 5.3. Yet saturated lipids do

yield a slightly stronger affinity for intersubunit sites, at least in the outer leaflet, which may drive the high amount of saturated enrichment observed at these sites in model membranes. Outer leaflet monounsaturated lipids are slightly more unfavorable in intersubunit sites than M4 sites, and this difference grows in the inner leaflet.

In contrast to saturated and monounsaturated lipids, PUFAs and cholesterol are highly selective for particular sites. As shown in Figure 5.4A, neutral PUFAs have significantly stronger affinities for M4 sites than for innersubunit sites in the same leaflet. Such selectivity is consistent with the PUFA enrichment density in Figure 5.3A, where n-3 PUFAs can occupy most regions of the TMD but have particularly high levels of enrichment around M4. It is further consistent with our expectations from model membranes (Figure 5.3C). Regardless of the site class, PUFAs favor the outer leaflet site over the inner leaflet site, but both sets of M4 sites are more favorable than both sets of intersubunit sites. Conversely, cholesterol has significantly stronger affinities for innersubunit sites than for M4 sites, which is also consistent with the enrichment density in Figure 5.3A and our expectations from model membranes (Figure 5.3C). For cholesterol, however, the leaflet is a bigger determinant of affinity than the site; cholesterol has a stronger affinity for either outer leaflet site compared to either inner leaflet site.

5.4.2 Lipid preferences of intersubunit and M4 sites

We now switch perspectives to considering which neutral lipids are most favorable for particular sites. As shown in Figure 5.5 A and B, intersubunit sites in both leaflets prefer cholesterol to phospholipids, which is expected based on the results from model membranes. Upon visual inspection, this result may appear to diverge from the cholesterol polar density plots in neuronal membranes (Figure 5.3 A). The present results show that while the overall footprint of cholesterol enrichment in (Figure 5.3 A) is small, this small region actually reflects a tight and persistently

occupied binding site. The highly right-shifted distributions for cholesterol are shown in Figure S1.

PUFA chains yield affinities for the intersubunit site that are approximately >0.5 kcal/mol stronger than saturated lipid affinities (Figure 5.5 A and B), which was unexpected based on results from model membranes but is consistent with the corresponding enrichment density in Figure 5.3A. More generally, neutral phospholipid affinities for intersubunit sites obey the following trend, from strongest to weakest: n-3 $>$ n-6 $>$ saturated $>$ monounsaturated. Thus, even though PUFA chains prefer M4 sites to intersubunit sites, and saturated chains prefer intersubunit sites to M4 sites, PUFAs have a stronger affinity for either site type than do saturated lipids.

For intersubunit sites, monounsaturated lipids have the weakest affinities (>0.5 kcal/mol), which may reflect a limited number of ways to pack the single kink of a monounsaturated chain in this concave site. In contrast, cholesterol and PUFAs are either small or highly flexible and may more easily pack across multiple sites. Saturated chains may pack parallel to the protein surface in these sites.

As shown in Figure 5.5C and D, M4 sites in both leaflets have the strongest affinity for n-3 PUFAs, and affinity weakens as acyl chain rigidity increases; from strongest to weakest the phospholipid affinities follow: n-3 $>$ n-6 $>$ monounsaturated $>$ saturated. This is consistent with a role for PUFAs in minimizing unfavorable membrane deformations caused by the pLGIC's conical-star shape.[40, 141, 87, 112, 113, 104] Surprisingly, cholesterol had a stronger affinity for M4 sites than any acyl chains other than n-3 PUFAs. Cholesterol is rigid, small, and has asymmetric sides (rough and smooth) which potentially allows it to embed between alpha-helices and compete with n-3 PUFAs for binding. Any cholesterol bound within the grooves of the subunit interface (as hypothesized based on atomistic simulations[41] and observed in β subunits of nAChR (using

coarse-grained simulations[225]), will also get counted within the M4 site.

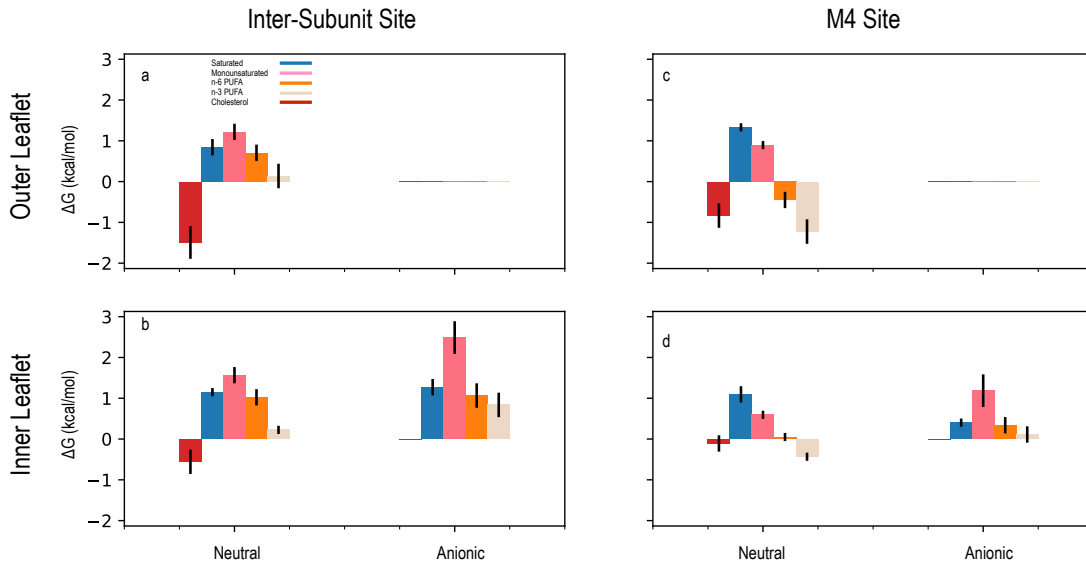


Figure 5.5: Data shown is identical but reorganized and recolored from Figure 5.4. Here, density-threshold affinities are colored by chain type (Saturated:blue, Monounsaturated:pink, n-6 PUFAs:orange, n-3 PUFAs:tan, Cholesterol:red), and separated by leaflet (rows) and site (columns).

5.4.3 Effect of Head Group Charge on Affinity Depends on Leaflet and Binding Site

Figure 5.3b compares the density enrichment for anionic headgroups with that of neutral headgroups. Data is shown for the inner leaflet only, because anionic lipids are not present in the outer leaflet at the start of simulations and few anionic lipids flip flop to the outer leaflet.

In the inner leaflet, the anionic lipids are expected to select for sites that are lined with basic amino acids, which are in different locations depending on subunit (Figure D2) As shown in Figure 5.3b, anionic lipids are generally enriched around the M3/M4 helices for the α_γ , γ , δ , and β subunits. Anionic lipids are enriched

at intersubunit sites and around M4 sites for all subunits but the α subunits. Non- α nAChR subunits have basic amino acids closer to M4 alpha-helices, as shown in Figure D2. We incorporate data from all five pseudo-symmetric sites to obtain the density-threshold affinities reported in Figure 5.4B, which suggest that anionic lipids have significantly stronger affinities for M4 sites on average. The average anionic affinity difference between inter-subunit and M4 sites is ~ -1.0 kcal/mol, as shown in Figures 5.4, 5.5d and SI D2. Although the magnitude of the affinity difference varies with acyl chain saturation, the sign is unchanged. We now switch again to the “site perspective” to compare whether inner leaflet sites would prefer occupancy by anionic or neutral lipids. As shown in Figure 5.5C, lipid affinity values for inter-subunit sites are either insensitive to charge (saturated or n-6 PUFA chains) or weaker for anionic lipids by at least 0.5 kcal/mol (monounsaturated and n-3 PUFA chains). In comparison, at the M4 site, saturated chains in anionic lipids have significantly stronger affinities than those in neutral lipids (a difference of ~ 0.5 kcal/mol). All other lipid chains attached to anionic headgroups have weaker affinities for the M4 site. The clear trend observed in neutral lipids (stronger affinities for more flexible acyl chains) is thus broken in anionic lipids because saturated anionic lipids are so favorable.

In summary, we observe that binding sites have clear preferences for particular head group charge and acyl-chain saturation, suggesting nAChR lipid occupancy to be driven in two steps, a “coarse-sorting” by head groups, and then “fine-sorting” by acyl-chains. A neutral lipid will occupy nAChR’s boundary region but acyl chains dictate where specific lipids occupy nAChR. Anionic lipids diverge from this pattern at the inner M4 site which has the strongest affinity for anionic lipids independent of saturation.

5.4.4 Role of Individual Lipid Headgroups in Determining Affinity

Neutral and anionic are bulk terms that categorize numerous lipid head-groups by charge. To understand the role of the chemical distinctions between head groups of like charge, we broke the headgroup affinities down by headgroup species in Table 5.1. In the outer leaflet, lipids contain a mixture of PE and PC headgroups. The small neutral PE head group has the strongest affinity across all headgroups for both inter-subunit and M4 sites, -0.2 ± 0.3 and -1.1 ± 0.2 kcal/mol respectively. The larger neutral PC headgroups are weaker than PE by $\sim > 0.5$ kcal/mol. In living cells, as in this neuronal membrane, PUFAs are more frequently tethered to PE than to PC or SM [78, 237, 45, 128, 160], so it is possible that this affinity simply reflects the high affinity of PUFA chains. However, even for identical chains, both experimental and simulation data [225] suggests stronger PE-ELIC than PC-ELIC interactions.

Table 5.2 shows specific head group affinities in the inner leaflet. As in the outer leaflet, lipids with PE headgroups still have the strongest affinity of all lipids, but in the inner leaflet we are also able to distinguish affinities for anionic species. For the intersubunit site, PI, PS, and PC have similar affinities (within statistical error), and have significantly stronger affinities for these sites than the phosphoinositides (PIPS) PIP1, PIP2, PIP3, which have a significantly stronger affinity than phosphatidic acid (PA). Thus, from strongest to weakest, PE>PI~PS~PC>>PIP1~PIP2~PIP3>>PA for the intersubunit site. In contrast, at the M4 site, more significant differences among moderate affinity headgroups emerge. PI has significantly stronger affinity than PS (a difference of 0.3 ± 0.1 kcal/mol), and PS has a significantly stronger affinity than PC (a difference of 0.2 ± 0.1 kcal/mol). From strongest to weakest, PE>PI>PS>PC>>PIP1~PIP2~PIP3~PA for the M4 site.

Table 5.1: Errors are standard errors (n=10 independent replicas).

	Intersubunit Sites ΔG (kcal/mol)	M4 Sites ΔG (kcal/mol)
PE	-0.2 ± 0.3	-1.1±0.2
PC	1.4±0.2	1.1 ±0.2

Table 5.2: Values are sorted by strength of affinity for intersubunit sites. Errors are standard errors (n=10 independent replicas).

	Inner Inter Sites ΔG (kcal/mol)	Inner M4 Sites ΔG (kcal/mol)
PE	0.3±0.2	-0.1±0.1
PI	0.9±0.3	0.2±0.1
PS	1.0 ±0.2	0.4±0.1
PC	1.0±0.2	0.9±0.1
PIP3	2.6±0.4	1.8 ±0.4
PIP2	2.8 ±0.2	2.1±0.4
PIP1	2.4 ±0.3	2.1±0.4
PA	3.0 ±0.3	2.2±0.4

5.5 Conclusions

Using coarse-grained simulations of the nAChR within a quasi-neuronal membrane containing over thirty lipid species, we have observed spontaneous lipid binding and quantified lipid specificity for two types of sites in the protein TMD. These two site classes represent the most concave (intersubunit site) and convex (M4 site) portions of the star-shaped nAChR and were initially observed as “hot spots” in our previous simulations[252, 240] of model membranes. Compared to classic ligand binding sites, these sites are superficial and have a large volume. The “ligands” occupying them are also non-traditional: lipids are flexible chain molecules that may only partially occupy the site and are likely to share the site with other partially-occupying ligands. While our lab has developed promising alchemical approaches[213] for calculating traditional affinities of atomistic lipids for more highly localized, well-defined sites, these hot spots required a different approach. Here we have proposed a softer “density-threshold affinity” for characterizing these affinities from spontaneous, unbiased coarse-grained simulations. While we restrict the use of this method here to nAChR, it should be straightforward to extend to any other transmembrane proteins with detectable regions of density enrichment.

Our results are summarized graphically in Figure 5.6. Based on our results from model membranes, we had hypothesized that PUFAs would select for the convex M4 sites and that raft-forming lipids like cholesterol and saturated lipids would select for the concave inter-subunit sites. Overall, our results were consistent with this expectation. Yet although lipids containing PUFAs do prefer the M4 site to the intersubunit site, their affinity for even the intersubunit sites are stronger than that of all other phospholipids. This result underscores the reliable partitioning of nAChR to PUFA-rich, liquid-disordered domains that we observed in homoacidic, domain forming membranes[225], and suggests PUFAs may have

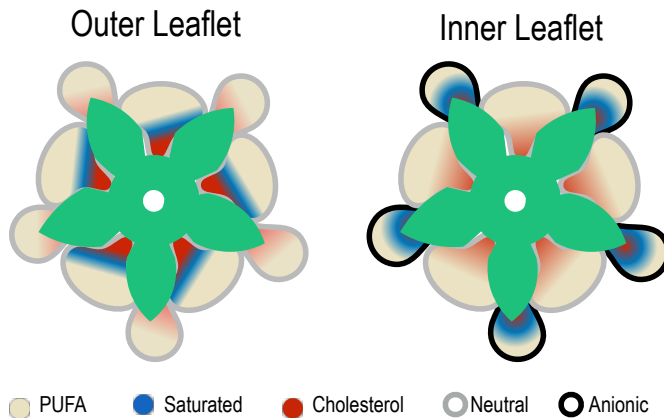


Figure 5.6: Protein is shown in the center of both leaflets in a cyan floral shape. Grey and black outlines depict sites favorable for neutral and anionic lipids respectively. Fill color represents the lipids most likely to occupy each site (red: cholesterol, blue: saturated, beige: PUFA) and outline represents headgroup charge (gray: neutral, black: anionic).

been absent from the intersubunit site in heteroacidic membranes[252] because of the constraints of the lipid topology. In the latter simulations, all lipids contained one saturated chain and one PUFA chain, so binding of the PUFA chain to its preferred M4 site requires the saturated chain to find the most favorable location nearby (in the intersubunit site) and may block binding of other PUFA chains to that site. These constraints are relaxed in the native neuronal membrane, which has a more diverse lipid composition with multiple different chain pairings; about 6% of the phospholipids in our simulated membranes contain no saturated chain at all. Nonetheless, our previous results[252] using simplified binary heteroacidic/cholesterol membranes played a key role in identifying the natural site boundaries.

As expected, within each leaflet cholesterol has the strongest affinity for the inter-subunit sites, although the affinity of cholesterol for the M4 sites was second only to that of n-3 PUFAs. Combined, these results are consistent with

an overwhelming amount of evidence spanning four decades that suggests direct interactions between cholesterol and nAChRs, regardless of the phospholipid composition of the membrane. One surprise for cholesterol was the role of the leaflet in determining affinity: cholesterol has a stronger affinity for either outer leaflet site compared to either inner leaflet site. This result may reflect competition with anionic saturated lipids in the inner leaflet, which would be consistent with multiple experiments[16, 248, 118, 239], suggesting that anionic lipids can partially or fully compensate for a loss of cholesterol. This result is also consistent with cholesterol embedded[41] in the outer TMD (which has numerous gaps in the amino acid density) but not the inner TMD.

Based on our results using ELIC[240], we had expected that anionic lipids would select for sites on the inner leaflet lined with basic residues. In the homomeric ELIC, these residues are symmetrically-arranged, while in the heteromeric nAChR they vary by subunit(figure D2a), with the M4 site containing the most such residues on most subunits. The present results support that expectation: anionic lipids have a stronger affinity for M4 than inter-subunit sites.

For both outer and inner leaflets, neutral lipids with smaller head groups (PE) have stronger affinity than the larger PC headgroup. It is unclear why PE is more favorable than other neutral lipids at this time, though this is consistent with previous work [225, 240], and the most straightforward explanation is that the smaller headgroup introduces fewer clashes with the protein TMD.

Among anionic lipids in the inner leaflet, regardless of the site, PS and PI have an affinity greater than or equal to PC, and much greater than the other anionic lipid headgroups (PIP1,PIP2,PIP3, and PA). The lipid headgroups PS and PI both have a charge of -1, while PA in the MARTINI forcefield[90] carries a charge of -2, and PIP1, PIP2, and PIP3 have charges of -3,-5, and -7. These results suggest that the inner leaflet sites select for monoanionic headgroups, while multianionic headgroups are highly unfavorable. Due to the limitations of

the coarse-grained model, future atomistic calculations are required to validate and understand the apparent preference of the M4 site for PI over PS.

The present results highlight the utility of model membranes for developing hypotheses of specific lipid-protein interactions, and the need to test those hypothesis within more complex native membranes. The present results could be tested and aid in interpretation of experiments carried out in more complex membranes. For instance, we would expect that mutations of the basic residues facing the inner leaflet would reduce binding of saturated phospholipids with anionic headgroups, which would be replaced with bound cholesterol. We would also predict that if PUFAAs cause gain of function via binding to the intersubunit site, this gain would be enhanced by replacing some heteroacidic lipids with homoacidic lipids while keeping the total fraction of PUFA chains constant. In general the present results provide valuable insight into how to predict lipid competition, which is one of the primarily challenges of interpreting experiments in complex membranes.

Acknowledgments

GB and LS were supported by the Busch Biomedical Foundation. This project was supported by generous allocation through the Rutgers University Office of Advanced Research Computing (OARC), which is supported by Rutgers University and the state of New Jersey. We are grateful to Dr. Jérôme Hénin for helpful input and suggestions.

Data Availability Statement

The data that support the findings of this study are available from the corresponding author upon reasonable request. Scripts for polar density analysis and plotting scripts can be found on github: <https://github.com/BranniganLab/densitymap>.

Appendix A: Domain formation around pLGICs in membranes of n-6 and n-3 polyunsaturated fatty acids

Pentameric ligand-gated ion channels (pLGIC) share a similar structure across both eukaryotes and prokaryotes. In mammals pLGICs are essential neuronal receptors found in both the central and peripheral nervous system [132]. The extra-cellular domain (ECD) is composed of beta-sheets with agonist binding sites at inter-subunit sites [116]. The transmembrane domain (TMD) resides in the membrane and is composed of 5 sets of 4 alpha-helices bundles (M1 to M4), see Figure A1A.

pLGIC alpha-helices can be described as three rings. The pore made of M2s, the central ring made of M1s and M3s, and the most external which is in direct contact with the membrane M4s. While M1-M3 helices are \sim perpendicular to the membrane, M4 is slightly tilted towards the membrane. This tilt provides a star and a cone shape to pLGICs, see Figure A1a. We hypothesize there acyl-chain saturation specificity associated with the star/cone shape.

We previously showed using domain forming model membranes, nAChR partitioned into PUFA rich liquid disordered domain l_{do} [225]. We chose two pLGICs, the homo-pentamer *Erwinia* ligand-gated ion channels (ELIC) and the hetero-pentamer γ -aminobutyric acid type A receptors (GABA_AR) simulated in two series of model domain forming PUFA rich membranes. Series one and two consisted of 20 simulations each of the n-6 PUFA dilinoleoylphosphatidylcholine(DLiPC) or the n-3 PUFA didocosahexaenoylphosphatidylethanolamine (dDHA-PE) , the saturated lipid dipalmitoylphosphatidylcholine (DPPC), and cholesterol.

Using VMD as a computational microscope [126] we observed pLGIC phase partitioning. All pLGICs simulated in these model membranes were observed to partition into l_{do} phases, consistent with [225], see Figure A1. n-6 PUFAs did not form well-defined domains, and while all three pLGICs are observed to

reside in the l_{do} raft forming lipids intermittently play a boundary lipid role. n-3 PUFAs formed well-defined domains with the bulk of a pLGIC residing in the l_{do} . However, in all cases, at least one side of the protein resides near the $l_{\text{o}}/l_{\text{do}}$ interface. pLGICs at the $l_{\text{o}}/l_{\text{do}}$ interface have a buffer of annular PUFAs. This suggests pLGICs partitioning to l_{do} phase is independent of protein sequence.

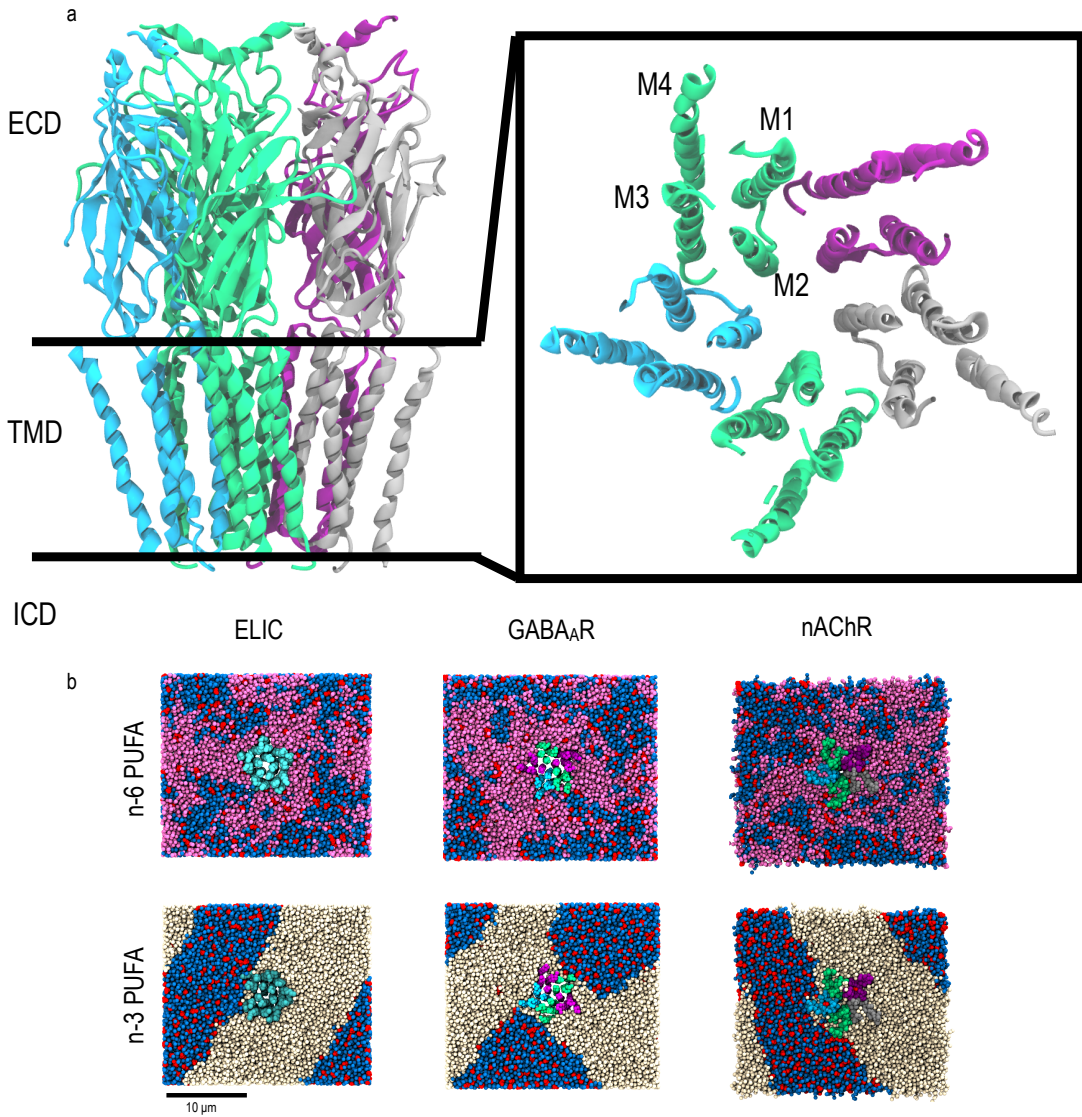


Figure A1: nAChR as a model pLGIC structure and pLGICs in PUFA rich model domain forming membranes. Colors for nAChR and GABA_AR are given by α : green, β : purple, δ : gray, γ : cyan, ELIC is cyan only. Lipids colors are $n - 6$: pink, $n - 3$: cream, saturated : blue, cholesterol : red. a) The pLGIC nAChR show in new cartoon. Left shows nAChR from a side view with the extra-cellular and transmembrane domains. Right is the transmembrane domain viewed from the extra-cellular point of view down. b) Domain forming membranes organized by protein and PUFA. All membranes are $\sim 25 \times 25 \text{ nm}^2$, and image is taken at the end of $4 \mu\text{s}$ (GABA_AR and ELIC) or $2 \mu\text{s}$ (nAChR) simulation.

Appendix B: Chapter 2 Supplementary

Supplementary figures associated with chapter 2.

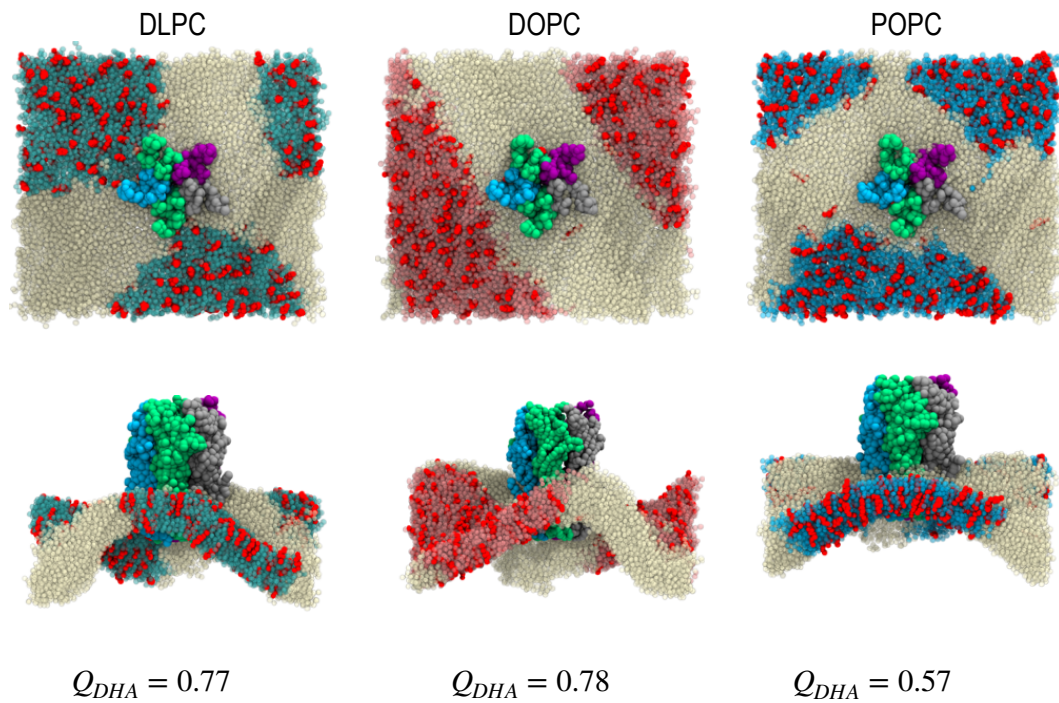


Figure B1: Membrane domain formation and protein domain partitioning in small membranes. Two viewpoints are shown of the final frame of a single nAChR in a membrane composed of dDHA-PE: X :CHOL 42.5:42.5:15, where X is either DLPC, DOPC, or POPC. Subunits are colored: α : green, β : purple, δ : gray, γ : cyan. Lipids are colored: Chol: red, dDHA-PE: white, DLPC: teal, DOPC : pink, POPC : cyan. Large deformations and undulations are caused by the highly flexible domains formed by dDHA-PE and the conical shape of nAChR.

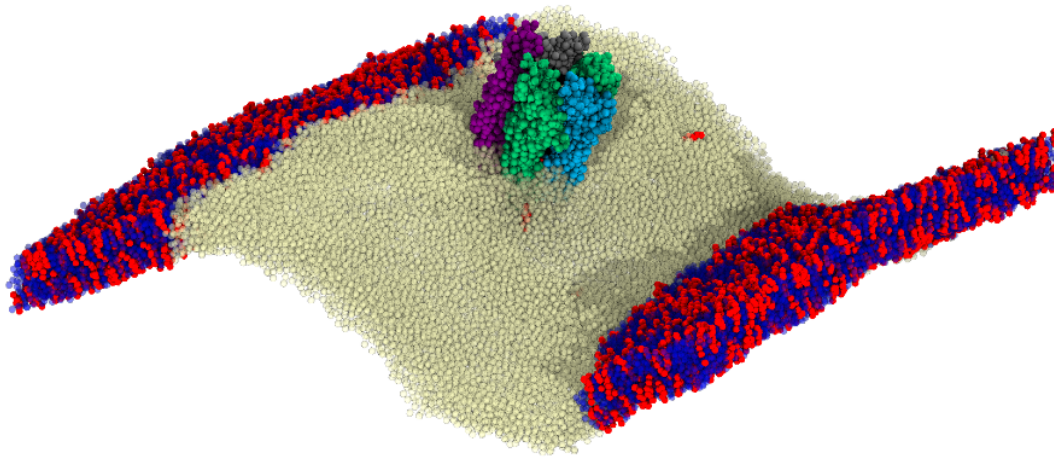


Figure B2: Alternate view of membrane from Figure 2.3A. The l_{do} domain formed by dDHA-PE (white) is highly flexible with large undulations; this flexibility may also result in more favorable incorporation of the cone-shaped nAChR transmembrane domain.

Appendix C : Chapter 4 Supplementary

Supplementary figures associated with chapter 5.

E coli

PE	m/z	Intensity	Theo. Mass	Delta (mmu)	Composition
14:0/14:0	634.4453	2.30E+04	634.4453	-0.07	C33 H65 O8 N P
14:0/16:0	662.4765	1.70E+05	662.4766	-0.11	C35 H69 O8 N P
16:0/16:1	688.4922	1.80E+05	688.4923	-0.06	C37 H71 O8 N P
16:0/16:0	690.5079	2.20E+06	690.5079	-0.06	C37 H73 O8 N P
16:0/17:1	702.5079	1.20E+06	702.5079	-0.06	C38 H73 O8 N P

PG	m/z	Intensity	Theo. Mass	Delta (mmu)	Composition
16:0/16:1	719.4868	2.60E+05	719.4869	-0.09	C38 H72 O10 P
16:0/16:0	721.5024	4.80E+05	721.5025	-0.07	C38 H74 O10 P
16:0/17:1	733.5024	1.20E+06	733.5025	-0.14	C39 H74 O10 P

16:1/18:1; 17:1/17:1	745.5023	3.10E+05	745.5025	-0.17	C40 H74 O10 P
16:0/18:1	747.518	4.80E+05	747.5182	-0.21	C40 H76 O10 P
17:1/18:1	759.5181	3.30E+05	759.5182	-0.05	C41 H76 O10 P
17:1/18:0; 17:0/18:1	761.5337	1.30E+06	761.5338	-0.1	C41 H78 O10 P
18:0/18:2	773.5337	6.30E+05	773.5338	-0.1	C42 H78 O10 P
18:1/19:1	787.5494	2.80E+05	787.5495	-0.1	C43 H80 O10 P
19:1/19:1	801.5649	2.60E+05	801.5651	-0.18	C44 H82 O10 P

ELIC

PE	m/z	Intensity	Theo. Mass	Delta (mmu)	Composition
14:0/14:0					
14:0/16:0	662.4769	9.30E+03	662.4766	0.3	C35 H69 O8 N P
16:0/16:1	688.4924	2.20E+04	688.4923	0.11	C37 H71 O8 N P
16:0/16:0	690.5078	8.30E+05	690.5079	-0.12	C37 H73 O8 N P
16:0/17:1	702.5078	1.70E+05	702.5079	-0.09	C38 H73 O8 N P

PG	m/z	Intensity	Theo. Mass	Delta (mmu)	Composition
16:0/16:1	719.4868	5.50E+04	719.4869	-0.1	C38 H72 O10 P
16:0/16:0	721.5025	2.30E+05	721.5025	-0.06	C38 H74 O10 P
16:0/17:1	733.5024	3.60E+05	733.5025	-0.12	C39 H74 O10 P
16:1/18:1; 17:1/17:1	745.5024	1.80E+05	745.5025	-0.14	C40 H74 O10 P
16:0/18:1	747.518	1.10E+05	747.5182	-0.19	C40 H76 O10 P
17:1/18:1	759.5182	2.00E+06	759.5182	0.04	C41 H76 O10 P
17:1/18:0; 17:0/18:1	761.5338	4.00E+05	761.5338	-0.04	C41 H78 O10 P
18:0/18:2	773.5338	3.20E+05	773.5338	0	C42 H78 O10 P
18:1/19:1	787.5494	1.80E+05	787.5495	-0.04	C43 H80 O10 P
19:1/19:1	801.5651	9.10E+04	801.5651	-0.03	C44 H82 O10 P

Table C1: Phophatidylethanolamine and phosphatidyl-glycerol species identified in lipid extracts by MS/MS. Table shows m/z, intensity, mass and mass accuracy of each phospholipid species.

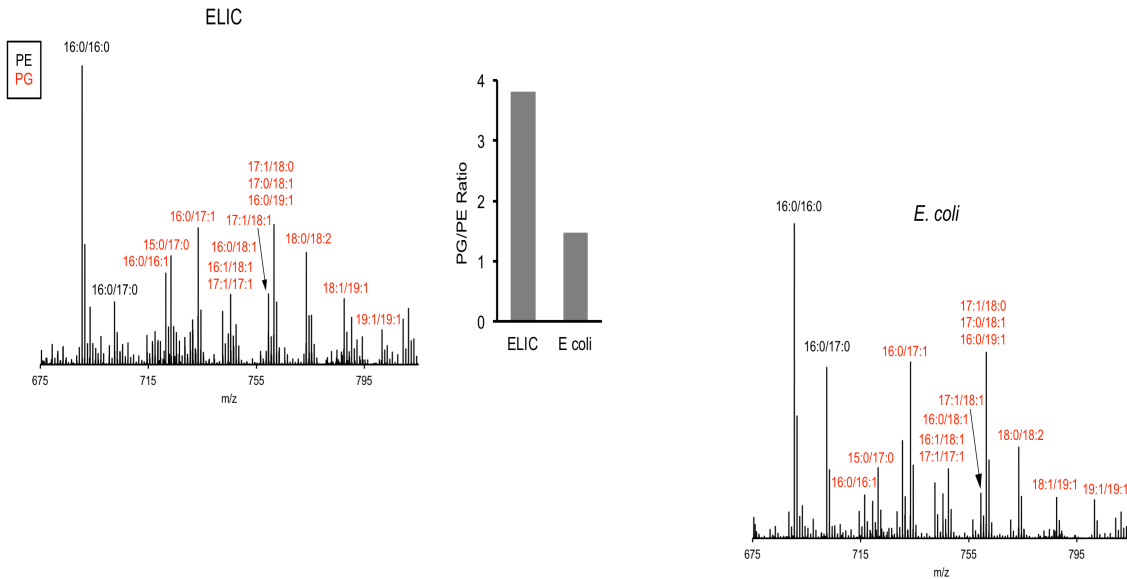


Figure C1: Labeled peaks correspond to PG (red) and PE (black) phospholipids with specific acyl chain combinations determined from MS2 fragmentation. *Right:* Graph shows quantification of the intensity of all PG species relative to PE species for ELIC and *E. coli* membrane samples.

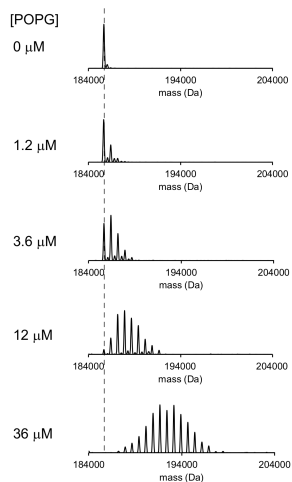


Figure C2: Representative deconvoluted spectra of 1 μM ELIC in C10E5 with increasing concentration of POPG. Dashed line indicates mass of apo ELIC.

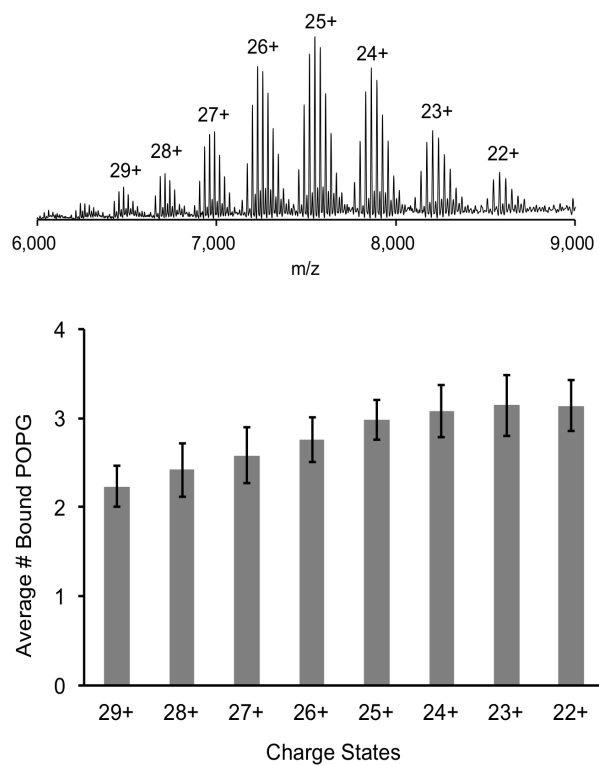


Figure C3: *Top:* Representative full native spectrum of the ELIC pentamer with 12 μM POPG with each charge state labeled. *Bottom:* Quantification of the average number of bound POPG to the ELIC pentamer at each charge state ($n=13$, $\pm\text{SD}$).

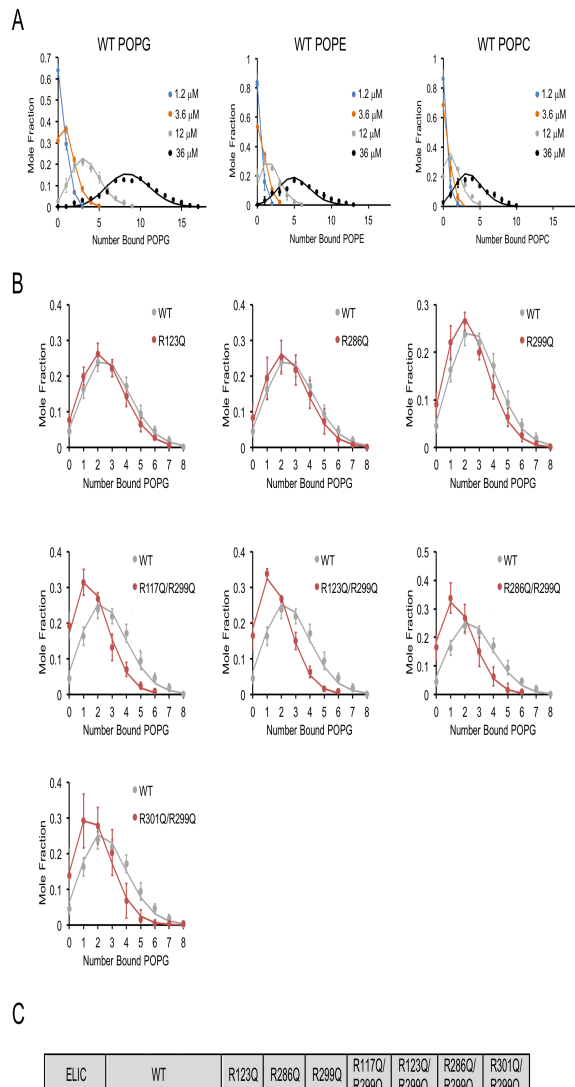


Figure C4:

Figure C4: Lipid binding data fit to binomial distributions. **(A)** Plots of mole fraction of phospholipid-bound ELIC derived from native MS experiments with varying concentrations of phospholipid (circles, n=3-6, \pm SD). Solid lines show global fits from a binding model based on a binomial distribution with 32 sites (N) of equal affinity (K) using K as shown in (C). **(B)** Plots of mole fraction of POPG-bound ELIC WT and mutants at 12 μ M POPG (circles, n=3-6, \pm SD). Solid lines show fits as in (A) in which K is held constant at 102 μ M and N is varied as indicated in (C). **(C)** Table showing dissociation constants (K) and number of sites (N) used in fits shown in (A) and (B).

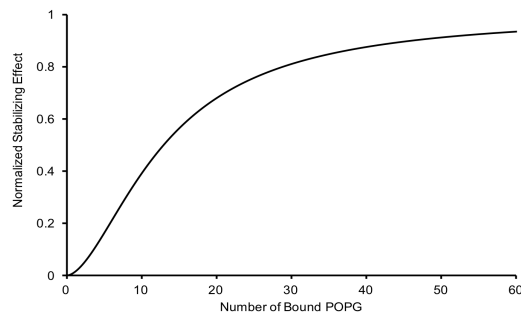


Figure C5: Relationship of the thermal stabilizing effect of POPG vs the average number of bound POPG derived from equating concentration of POPG from the sigmoid functions used to fit the POPG binding (Fig. 4.1B) and thermal stability data (Fig. 4.2A). The resulting relationship is: $S = \frac{1}{1 + (\frac{13.7}{P})^{1.7}}$, where P is the average number of bound POPG and S is the normalized thermal stabilizing effect.

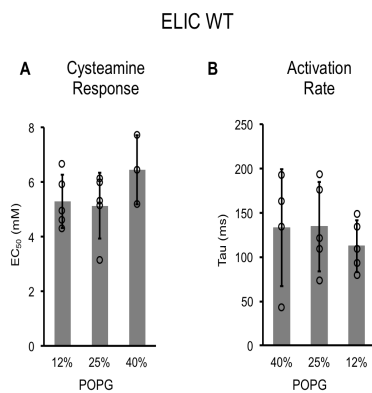


Figure C6: Channel properties of WT ELIC responses to cysteamine. **(A)** EC₅₀ for peak responses to cysteamine of WT ELIC in giant liposomes of varying mole% POPG (n=3-5, \pm SD). **(B)** Activation time constants (τ) derived from single exponential fits of WT ELIC in response to 30 mM cysteamine in giant liposomes of varying mole% POPG (n=4-5, \pm SD).

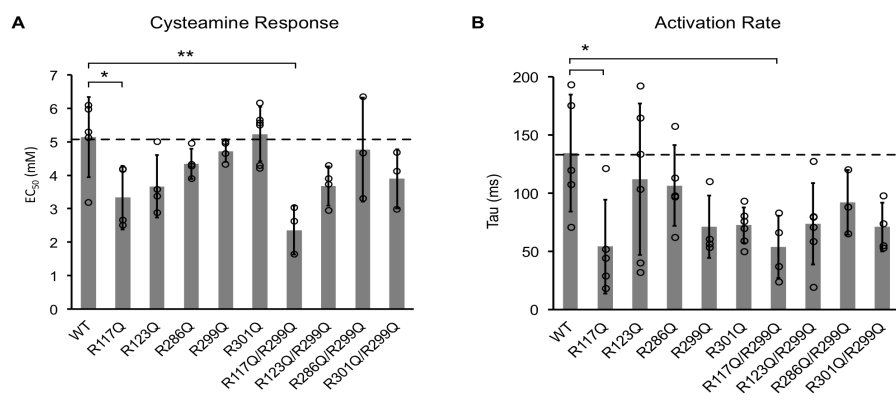


Figure C7: Channel properties of ELIC WT and mutant responses to cysteamine in giant liposomes of 25 mole% POPG. (A) Graph of EC₅₀ for peak responses to cysteamine of ELIC WT and mutants (n=4-7, \pm SD, *p<0.05, **p<0.01). (B) Activation time constants (tau) of ELIC WT and mutants in response to 30 mM cysteamine (n=4-7, \pm SD, **p<0.01).

Appendix D : Chapter 5 Supplementary

Supplementary figures associated with chapter 5.

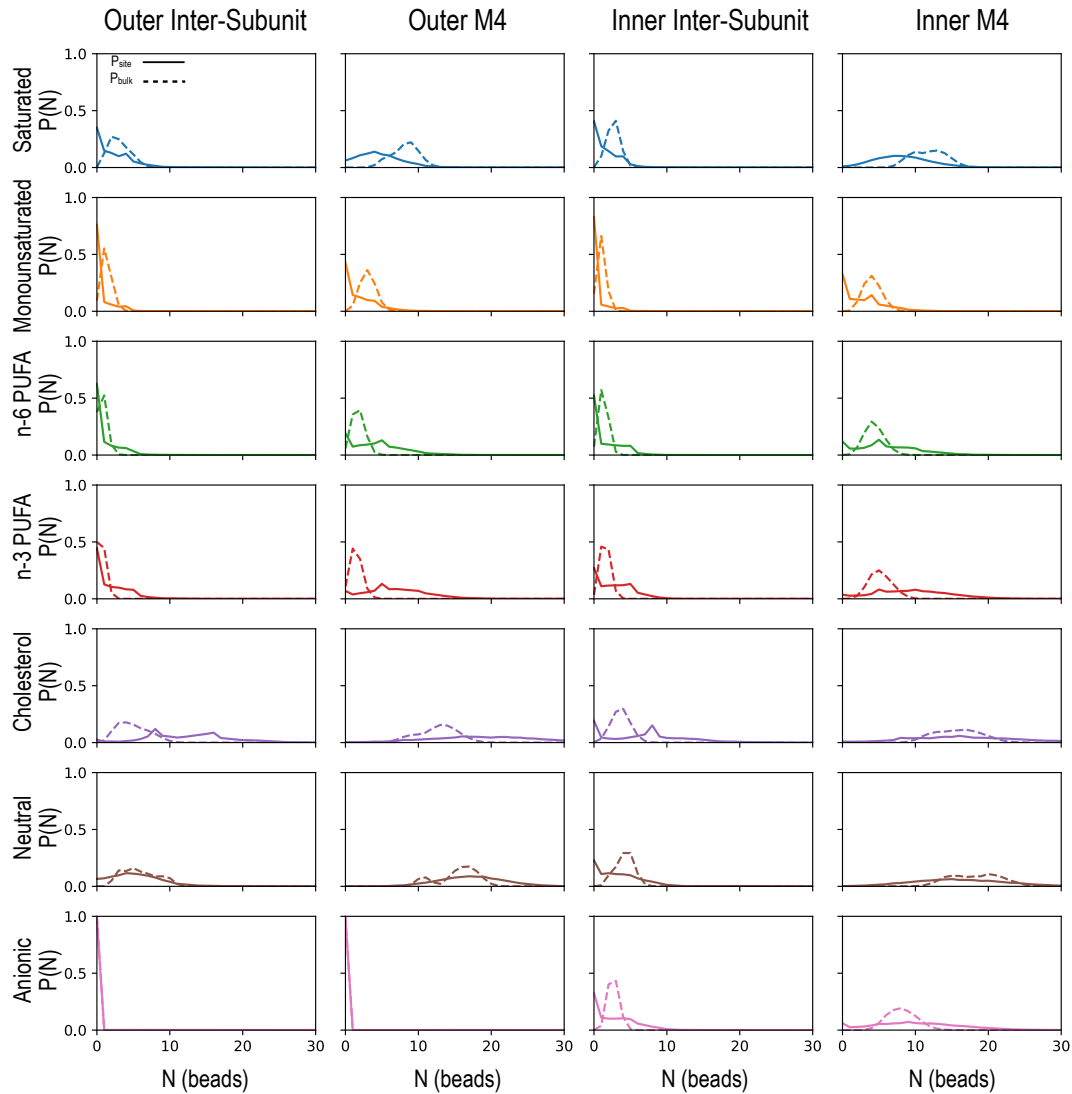


Figure D1: Solid lines represent P_{site} , the probability of a given number of beads found at occupancy site, averaged over both the course of the simulation and subunit sites. Dashed lines represent P_{bulk} , the probability of a given number of beads in the bulk averaged over time. Bulk areas are square regions of equal area to occupancy sites.

Table D1: Lipid ratios used for neuronal simulations grouped by head group.

Head Group	Lipids	Outer (%)	Inner (%)
	CHOL	44.3	40.67
PC		30.5	15
PC	DPPC	6.7	3.3
	DOPC	2.8	1.4
	POPC	11	5.4
	PFPC	0.7	0.4
	PAPC	5.9	2.9
	PUPC	2.1	1.0
	OIPC	0.7	0.4
	OUPC	0.5	0.3
PE		13.8	23.4
PE	POPE	1.6	2.7
	PAPE	4	6.7
	PUPE	6.3	10.7
	OIPE	0.2	0.3
	OAPE	0.9	1.5
	OUPE	0.9	1.5
SM		11.3	2.5
SM	DPSM	7.4	1.7
	PBSM	1.4	0.3
	POSM	0.9	0.2
	PNSM	1.7	0.4
PS		0.0	10.8
PS	DPPS	0.0	0.5
	POPS	0.0	2.7
	PAPS	0.0	3.0
	PUPS	0.0	3.8
	OUPS	0.0	0.8
PA		0.0	0.4
PA	POPA	0.0	0.1
	PAPA	0.0	0.3
PI		0.0	2.3
PI	POPI	0.0	1.4
	PIPI	0.0	0.6
	PAPI	0.0	1.4
	PUPI	0.0	2.3
PIPS		0.0	1.5
PIPS	POP1	0.0	0.2
	PAP1	0.0	0.3
	POP2	0.0	0.2
	PAP2	0.0	0.3
	POP3	0.0	0.2
	PAP3	0.0	0.3

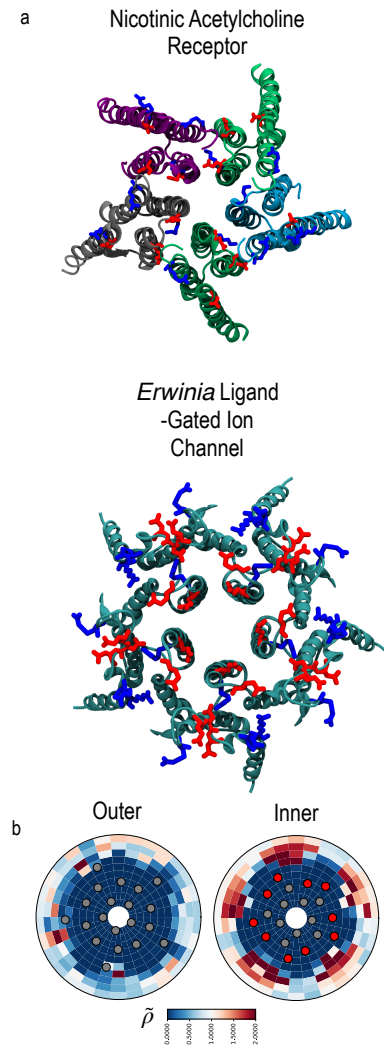


Figure D2: a) Structure of the TMD viewed from the extracellular side looking at the membrane, of nAChR (top)[242] and ELIC[193] (bottom). nAChR is colored as in Figure 1, ELIC is cyan. Basic amino acids are colored in blue while acidic amino acids are colored in red for both structures. b) Anionic polar density enrichment observed in ELIC, derived from [240]. Grey circles represent center of mass of alpha-helices, red circles represent center of mass of alpha-helices with basic amino acids.

Table D2: Affinities broken down by headgroup and acyl chain to reveal cross-correlation.

	Outer Inter Sites ΔG (kcal/mol)	Outer M4 Sites ΔG (kcal/mol)	Inner Inter Sites ΔG (kcal/mol)	Inner M4 Sites ΔG (kcal/mol)
CHOL	-1.5 ±0.4	-0.8±0.3	-0.6±0.3	-0.1±0.2
Sat	0.7 ±0.3	1.3 ±0.2	1.0 ± 0.2	1.1 ±0.2
Mono	1.2 ±0.2	0.8± 0.2	1.4 ±0.1	0.7 ±0.2
n-6	0.6 ±0.2	-0.5 ±0.1	0.3 ±0.2	-0.3 ±0.2
n-3	-0.0 ±0.4	-1.3 ±0.3	-0.20.2±	-0.9±0.2
Neutral	0.4 ±0.3	-0.4±0.2	0.5 ±0.2	0.5±0.2
Anionic	2.4 ±0.4	2.4 ±0.4	0.3 ±0.2	-0.3 ±0.1
Sat Neutral	0.8 ±0.2	1.3 ±0.1	1.1±0.1	1.1 ±0.2
Mono Neutral	1.2±0.2	0.9 ±0.1	1.6 ±0.2	0.6 ±0.1
n-6 Neutral	0.7 ±0.2	-0.5 ±0.2	1.0 ±0.2	0.0 ±0.1
n-3 Neutral	0.1 ±0.3	-1.2±0.3	0.2 ±0.1	-0.4 ±0.1
Sat Anionic			1.3±0.2	0.4±0.1
Mono Anionic			2.5 ±0.4	1.2 ±0.4
n-6 Anionic			1.1 ±0.3	0.3±0.2
n-3 Anionic			0.8 ±0.3	0.1 ±0.2

Table D3.1: Complete listing of affinities for intersubunit sites in the outer leaflet.

Lipids	Outer $\alpha_\gamma - \beta$ (ΔG (kcal/mol))	Outer $\beta - \delta$ (ΔG (kcal/mol))	Outer $\delta - \alpha_\delta$ (ΔG (kcal/mol))	Outer $\alpha_\delta - \gamma$ (ΔG (kcal/mol))	Outer $\gamma - \alpha_\gamma$ (ΔG (kcal/mol))
Lipid Species					
CHOL	-0.9	-1.4	-1.5	-1.6	-2.0
DOPC	3.5	3.4	2.2	2.8	2.3
DPPC	3.3	2.1	2.3	1.4	2.0
DPPS	4.1	4.1	4.2	3.9	4.2
DPSM	2.1	2.7	2.3	1.2	2.1
OAPE	1.9	2.5	1.9	1.4	1.9
OIPC	3.0	2.9	2.4	4.0	2.6
OIPE	2.4	4.0	3.5	3.8	2.4
OUPC	2.0	2.2	1.9	1.7	2.9
OUPE	0.9	1.0	1.4	2.0	1.7
PAPC	0.6	0.9	1.0	1.1	1.2
PAPE	1.1	1.2	1.1	1.4	1.2
PBSM	4.9	4.9	3.4	4.4	3.1
PFPC	1.9	1.3	2.4	3.1	3.3
PNSM	3.2	4.9	2.5	4.3	2.7
POPC	2.2	1.8	1.7	2.0	1.6
POPE	2.8	2.6	2.4	3.0	2.6
POSM	3.3	2.6	3.8	2.9	3.4
PUPC	1.4	1.5	1.9	1.0	1.9
PUPE	0.0	0.3	0.1	-0.5	0.2
Head Groups PC	0.9	0.4	1.0	0.7	1.1
PE	-0.4	-0.3	-0.2	-0.3	0.4
SM	1.9	2.5	2.2	1.2	2.0
Acyl-Chain Saturation Sat	1.0	0.6	0.9	0.5	0.7
Monounsat	1.1	1.1	1.1	1.3	1.4
n-6	0.4	0.5	0.8	0.7	0.7
n-3	-0.2	-0.2	0.0	-0.1	0.5
Head Group Charge					
Neutral	0.7	-0.1	0.7	0.2	0.5
Acyl-Chain Saturation by Charge Neutral Sat	1.0	0.6	0.9	0.5	1.2
Neutral Monounsat	1.1	1.2	1.1	1.3	1.4
Neutral n-6	0.4	0.5	0.8	0.7	1.1
Neutral n-3	-0.2	0.2	0.3	-0.1	0.5

Table D3.2: Complete listing of affinities for M4 sites in the outer leaflet.

Lipids	Outer α_γ (ΔG (kcal/mol))	Outer β (ΔG (kcal/mol))	Outer δ (ΔG (kcal/mol))	Outer α_δ (ΔG (kcal/mol))	Outer γ (ΔG (kcal/mol))
Lipid Species					
CHOL	-1.0	-1.3	-0.8	-0.8	-0.2
DOPC	1.8	2.1	1.5	1.5	1.9
DPPC	1.3	2.0	1.7	2.2	1.8
DPSM	1.6	1.5	1.7	1.7	2.0
OAPE	1.5	1.3	1.3	0.9	1.1
OIPC	2.2	1.8	2.8	2.1	2.2
OIPE	2.0	2.2	3.1	2.6	2.8
OUPC	1.7	1.5	1.5	1.5	1.3
OUPE	0.6	0.8	0.8	0.9	0.9
PAPC	0.2	0.3	0.5	0.3	0.2
PAPE	0.4	0.3	0.1	0.4	0.4
PBSM	2.7	3.0	3.5	2.7	2.9
PFPC	2.0	1.3	1.9	1.8	1.7
PNSM	2.3	2.3	2.5	2.5	2.6
POPC	1.1	1.4	1.5	1.4	1.7
POPE	1.9	1.9	1.7	1.7	2.3
POSM	2.7	2.8	2.8	2.9	2.9
PUPC	0.5	0.8	1.0	0.8	0.5
PUPE	-0.3	-0.6	-0.6	-1.0	-0.9
Head Groups					
PC	0.3	0.2	0.8	0.8	0.3
PE	-0.7	-1.0	-1.3	-1.3	-1.2
SM	1.5	1.6	1.8	1.8	1.9
Acyl-Chain Saturation					
Sat	1.0	1.0	1.3	1.9	1.4
Monounsat	0.8	0.7	0.7	0.7	1.1
n-6	-0.4	-0.6	-0.3	-0.5	-0.4
n-3	-1.1	-1.2	-1.0	-1.3	-1.8
Head Group Charge					
Neutral	-0.2	-0.9	0.0	0.0	-0.7
Acyl-Chain Saturation by Charge Neutral Sat					
Neutral Monounsat	1.0	1.0	1.3	2.0	1.4
Neutral n-6	0.8	0.7	0.7	1.2	1.1
Neutral n-3	-0.4	-0.6	-0.3	-0.5	-0.4
	-0.8	-1.2	-1.0	-1.3	-1.8

Table D3.3: Complete listing of affinities for intersubunit sites in the inner leaflet.

Lipids	Inner $\alpha_\gamma - \beta$ (ΔG (kcal/mol))	Inner $\beta - \delta$ (ΔG (kcal/mol))	Inner $\delta - \alpha_\delta$ (ΔG (kcal/mol))	Inner $\alpha_\delta - \gamma$ (ΔG (kcal/mol))	Inner $\gamma - \alpha_\gamma$ (ΔG (kcal/mol))
Lipid Species					
CHOL	-0.4	-0.4	-1.1	0.3	-1.2
DOPC	2.4	3.1	2.9	2.6	2.9
DPPC	1.9	2.7	2.1	2.3	2.1
DPPS	4.4	4.2	3.5	4.9	5.3
DPSM	2.5	1.7	2.1	2.6	2.5
OAPE	2.3	2.5	1.9	1.9	3.1
OIPC	3.1	2.9	3.8	3.0	3.4
OIPE	4.9	3.3	3.5	3.8	3.3
OUPC	3.1	3.2	2.3	2.7	2.1
OUPE	2.4	1.4	1.5	1.8	1.7
OUPS	2.4	2.8	1.5	2.2	2.1
PAP1	1.4	3.3	1.5	1.6	2.9
PAP2	1.9	3.9		1.1	2.1
PAP3	2.7	1.7	3.2	1.6	2.0
PAPA	3.9	2.4	2.7	3.1	3.2
PAPC	1.7	1.7	1.7	1.6	1.9
PAPE	0.9	1.5	1.1	1.4	1.2
PAPI	1.7	1.7	1.9	1.6	1.4
PAPS	1.5	2.2	1.8	1.7	1.7
PBSM	3.2	3.5	3.5	3.8	3.5
PFPC	2.2	2.6	2.9	2.6	3.6
PIPI	3.6	2.9	1.8	3.3	2.4
PNSM	3.0	2.8	2.8	3.6	3.2
POP1	5.3		3.2	3.3	4.6
POP2	3.5	3.5	3.5	3.4	
POP3	3.2	4.4		3.4	
POPA			5.3	5.3	
POPC	2.4	1.7	2.0	2.0	1.8
POPE	2.7	3.0	2.6	3.4	2.4
POPI	2.4	2.9	2.5	2.4	2.3
POPS	2.7	3.0	1.7	3.8	2.8
POSM	3.9	4.1	2.7	4.3	3.4
PUPC	2.0	1.7	1.7	2.1	2.0
PUPE	0.1	0.2	0.4	0.5	0.4
PUPI	1.0	1.0	1.4	1.1	0.7
PUPS	1.2	1.7	1.0	1.5	1.6
Head Groups PC					
PE	-0.1	0.3	0.3	0.4	0.6
SM	2.4	1.7	1.9	2.6	2.5
PS	0.8	1.4	0.5	1.1	1.4
PA	3.7	2.5	2.6	3.1	3.3
PI	0.9	0.9	1.0	0.9	1.0
PIP1	1.5	3.6	1.6	2.0	3.3
PIP2	2.1	4.0	4.1	1.3	2.4
PIP3	3.3	2.2	3.6	1.8	2.3
Acyl-Chain Saturation Sat					
Monounsat	1.4	1.5	0.9	1.4	1.6
n-6	0.1	0.6	0.3	0.0	0.7
n-3	-0.3	0.0	-0.3	-0.2	0.1
Head Group Charge Neutral					
Anionic	0.1	0.8	0.1	0.1	0.4
Acyl-Chain Saturation by Charge Neutral Sat					
Neutral Monounsat	1.7	1.6	1.5	1.6	1.4
Neutral n-6	0.7	1.2	0.8	1.0	1.4
Neutral n-3	0.0	0.0	0.1	0.3	0.6
Anionic Sat					
Anionic Monounsat	2.4	3.0	1.6	3.0	2.4
Anionic n-6	0.9	1.6	1.1	0.6	1.1
Anionic n-3	0.7	1.1	0.6	0.9	0.8

Table D3.4: Complete listing of affinities for M4 sites in the inner leaflet.

Lipids	Inner α_γ (ΔG (kcal/mol))	Inner β (ΔG (kcal/mol))	Inner δ (ΔG (kcal/mol))	Inner α_δ (ΔG (kcal/mol))	Inner γ (ΔG (kcal/mol))
Lipid Species					
CHOL	-0.3	0.2	-0.4	-0.3	0.3
DOPC	1.6	1.4	1.8	1.5	1.6
DPPC	1.1	1.1	1.4	1.2	1.3
DPPS	2.2	2.6	2.9	2.6	3.1
DPSM	1.6	1.3	1.6	1.3	1.6
OAPE	1.4	1.3	1.5	1.2	1.4
OIPC	2.1	2.0	2.2	2.0	1.9
OIPE	2.2	2.8	2.7	2.1	2.4
OUPC	2.2	2.3	2.6	2.0	1.6
OUPE	1.2	1.0	1.0	0.9	0.8
OUPS	1.5	2.0	1.6	1.5	1.6
PAP1	2.6	1.7	2.4	1.9	1.3
PAP2	2.7	1.7	2.8	2.4	1.1
PAP3	2.0	1.9	1.3	2.3	1.1
PAPA	2.6	1.9	2.4	2.6	2.0
PAPC	0.8	0.8	0.9	0.7	0.8
PAPE	0.4	0.4	0.5	0.3	0.4
PAPI	1.2	1.1	1.0	1.2	1.1
PAPS	0.8	0.9	1.1	1.0	0.7
PBSM	2.2	2.1	2.3	2.5	2.5
PFPC	2.2	2.0	2.1	1.9	2.1
PIPI	2.3	2.1	2.3	1.8	2.7
PNSM	2.4	2.1	2.1	1.9	2.5
POP1	3.6	3.5	2.9	3.0	2.6
POP2	3.9	2.6	2.4	3.0	2.6
POP3	2.9	2.9	2.9	3.3	2.2
POPA	3.1	3.2	3.8	3.1	3.4
POPC	0.9	1.0	0.9	0.9	1.1
POPE	1.3	1.3	1.6	1.4	1.6
POPI	1.5	1.6	1.7	1.3	1.7
POPS	1.6	1.6	1.5	1.5	1.8
POSM	2.5	2.7	2.9	2.8	2.6
PUPC	1.5	1.2	1.5	1.1	1.0
PUPE	-0.1	-0.4	-0.1	-0.1	-0.3
PUPI	0.9	0.4	0.4	0.9	0.3
PUPS	0.9	0.7	0.5	0.8	0.7
Head Groups					
PC	0.6	0.7	0.8	0.7	0.6
PE	0.0	-0.2	-0.3	-0.1	-0.1
SM	1.4	1.4	1.4	1.1	1.6
PS	0.3	0.5	0.3	0.5	0.3
PA	2.5	1.8	2.4	2.5	2.0
PI	0.4	0.2	0.1	0.4	0.1
PIP1	2.7	1.8	2.3	2.1	1.4
PIP2	2.8	1.7	2.3	2.4	1.2
PIP3	2.0	2.1	1.4	2.3	1.2
Acyl-Chain Saturation					
Sat	0.9	1.2	0.8	1.4	1.2
Monounsat	0.4	0.8	0.5	0.8	0.9
n-6	-0.1	-0.4	-0.3	-0.1	-0.6
n-3	-0.5	-1.0	-1.0	-0.5	-1.2
Head Group Charge					
Neutral	0.3	0.4	0.3	0.6	0.5
Anionic	0.0	-0.3	-0.4	0.2	-0.7
Acyl-Chain Saturation by Charge					
Neutral Sat	0.9	1.2	0.8	1.2	1.4
Neutral Monounsat	0.5	0.7	0.6	0.4	0.8
Neutral n-6	0.0	0.1	0.1	-0.1	0.1
Neutral n-3	-0.2	-0.6	-0.4	-0.4	-0.6
Anionic Sat	0.3	0.5	0.1	0.7	0.3
Anionic Monounsat	1.1	1.2	1.2	1.2	1.2
Anionic n-6	0.5	0.2	0.5	0.5	-0.1
Anionic n-3	0.5	0.0	0.0	0.3	-0.1

Table D4.1: Angular and radial boundaries are used to define sites for a given total area. Accessible areas are as described in Methods *Binding Site Definition and Occupancy Calculations*. Methods *Calculation of Accessible Area*

	Outer $\alpha_\gamma - \beta$	Outer $\beta - \delta$	Outer $\delta - \alpha_\delta$	Outer $\alpha_\delta - \gamma$	Outer $\gamma - \alpha_\gamma$
Angular Boundaries	$1.13 \geq \theta \leq 1.63$ rad	$0.37 \geq \theta \leq 6.16$ rad	$4.9 \geq \theta \leq 5.4$ rad	$3.64 \geq \theta \leq 4.15$ rad	$2.38 \geq \theta \leq 2.89$ rad
Radial Boundaries	$10 < r \leq 32\text{\AA}$	$10 < r \leq 32\text{\AA}$	$10 < r \leq 32\text{\AA}$	$10 < r \leq 32\text{\AA}$	$10 < r \leq 32\text{\AA}$
Total Area	301.59\AA^2	361.91\AA^2	301.59\AA^2	301.59\AA^2	301.59\AA^2
Accessible Area	104.40\AA^2	50.89\AA^2	63.80	81.20\AA^2	34.80\AA^2

Table D4.2: Angular and radial boundaries are used to define sites for a given total area. Accessible areas are as described in Methods *Binding Site Definition and Occupancy Calculations*. Methods *Calculation of Accessible Area*

	Outer α_γ	Outer β	Outer δ	Outer α_δ	Outer γ
Angular Boundaries	$1.76 \geq \theta \leq 2.26$ rad	$0.5 \geq \theta \leq 1$ rad	$5.52 \geq \theta \leq 6.03$ rad	$4.27 \geq \theta \leq 4.78$ rad	$3.02 \geq \theta \leq 3.52$ rad
Radial Boundaries	$10 < r \leq 44\text{\AA}$	$10 < r \leq 44\text{\AA}$	$10 < r \leq 44\text{\AA}$	$10 < r \leq 44\text{\AA}$	$10 < r \leq 44\text{\AA}$
Total Area	703.72\AA^2	703.72\AA^2	703.72\AA^2	703.72\AA^2	703.72\AA^2
Accessible Area	173.14\AA^2	117.29\AA^2	184.31\AA^2	195.48\AA^2	161.97\AA^2

Table D4.3: Angular and radial boundaries are used to define sites for a given total area. Accessible areas are as described in Methods *Binding Site Definition and Occupancy Calculations*. Methods *Calculation of Accessible Area*

	Inner $\alpha_\gamma - \beta$	Inner $\beta - \delta$	Inner $\delta - \alpha_\delta$	Inner $\alpha_\delta - \gamma$	Inner $\gamma - \alpha_\gamma$
Angular Boundaries	$1.38 \geq \theta \leq 1.88$ rad	$0.13 \geq \theta \leq 0.62$ rad	$5.15 \geq \theta \leq 5.65$ rad	$3.77 \geq \theta \leq 4.27$ rad	$2.64 \geq \theta \leq 3.01$ rad
Radial Boundaries	$10 < r \leq 32\text{\AA}$				
Total Area	301.59\AA^2	241.27\AA^2	301.59\AA^2	241.27\AA^2	241.27\AA^2
Accessible Area	68.29\AA^2	74.68\AA^2	68.29\AA^2	63.19\AA^2	40.21\AA^2

Table D4.4: Angular and radial boundaries are used to define sites for a given total area. Accessible areas are as described in Methods *Binding Site Definition and Occupancy Calculations*. Methods *Calculation of Accessible Area*

	Inner α_γ	Inner β	Inner δ	Inner α_δ	Inner γ
Angular Boundaries	$2.01 \geq \theta \leq 2.51$ rad	$.75 \geq \theta \leq 1.26$ rad	$5.78 \geq \theta \leq 6.16$ rad	$4.4 \geq \theta \leq 5.03$ rad	$3.14 \geq \theta \leq 3.64$ rad
Radial Boundaries	$10 < r \leq 44\text{\AA}$	$10 < r \leq 44\text{\AA}$	$10 < r \leq 44\text{\AA}$	$10 < r \leq 44\text{\AA}$	$10 < r \leq 44\text{\AA}$
Total Area	703.72\AA^2	844.46\AA^2	703.72\AA^2	844.46\AA^2	844.46\AA^2
Accessible Area	211.69\AA^2	273.88\AA^2	205.97\AA^2	302.41\AA^2	273.88\AA^2

Vita

Education

Academics

- 2016-Expected Winter 2020 Computational and Integrative Biology, Rutgers University Camden, NJ *PhD*
- 2014-2016 Computational and Integrative Biology Rutgers University Camden, NJ *MS*
- 2008–2012 Physics Juniata College Huntingdon, PA *BS*

Certificates

- **2019 Software Carpentry** Software Carpentries Instructor
- **2015 Rutgers University Camden** Level I Tutor
- **2012 Pennsylvania State University** Nanofabrication Manufacturing Technology (NMT) Capstone Semester

Publications

- **2019:** Liam Sharp, Reza Salari, Grace Brannigan, *Boundary lipids of the nicotinic acetylcholine receptor: Spontaneous partitioning via coarse-grained molecular dynamics simulation*, Biochimica et Biophysica Acta (BBA) - Biomembranes, ISSN 0005-2736, <https://doi.org/10.1016/j.bbamem.2019.01.005>.
- **2019:** Kristen Woods*, Liam Sharp*, Grace Brannigan, *Untangling direct and domain-mediated interactions between nicotinic acetylcholine receptors in dha-rich membranes*, The Journal of membrane biology, ISSN 0022-2631, <https://doi.org/10.1007/s00232-019-00079-0>.
 - Joint first author.

- **2019:** Ailing Tong, John T. Petroff II, Fong-Fu Hsu, Philipp A. M. Schmid-peter, Crina M. Nimigean, Liam Sharp, Grace Brannigan, Wayland W. L. Cheng, *Direct Binding of Phosphatidylglycerol at Specific Sites Modulates Desensitization of a Pentameric Ligand-Gated Ion Channel*, eLife, doi: 10.7554/eLife.50766.
 - I ran coarse-grained simulations of ELIC in membranes containing PG, which were validated by our experimental collaborators.

Leadership Experience

Leadership Roles

- Co-Computational Chair for Center for Computational and Integrative Biology's student run organization. This position is shared with an Experimental Chair and a Sitting President. Assists with:
 - Planning student social and student informational events.
 - Leading journal readings and discussions.
 - Communicating student issues with the Director and Graduate Director.
 - Welcoming and guiding prospective and new students.
 - Representing CCIB at undergraduate open houses and keeping track of questions asked about undergraduate program.
- CCIB Graduate Student Liaison with the Graduate Student Union Representative. I am in charge of keeping in contact with the union, bringing up issues students have with university related concerns, and setting up meeting with our center's students and the union representative.
- Senior graduate student within the Brannigan Lab.
 - Helped train and mentor two undergraduate and four graduate students.
 - Assisted with keeping computers and users up to date with IT.
 - On occasion, led lab group meetings.
 - Discussed approaches and concerns dealing with peers research.
 - Assisted with daily lab maintenance and reporting lab issues.
 - Assisted with benchmarking molecular dynamic simulations for various allocation grants.
 - Assisted with developing in house manuals.

Teaching

- Developed, adapted, and maintained curriculums for algebra and mathematical physics courses.
- Participated in approximately 10 educational training sessions through Rutgers Camden Learning Center and the Biophysics Society Annual Conference.
- Taken part in Software Carpentry Instructor reviews and updates three times a year .
- Taught classes as small as three students and as large as thirty-five.
- Tutored one-on-one in math and physics during my MS.

Courses Taught

- **Spring Semester 2019:**
Mathematical Physics (3 credits)
- **Fall Semester 2018:**
Introductory Physics Lab (1 credits)
- **2017-2018:**
Advanced Algebra (4 credits)
- **2016-2017:**
Introductory Algebra (3 credits)

Additional Teaching Experience

- **Fall 2020:** Guided Version Control with Git in Software Carpentry Workshop.
- **Fall 2019:** Guided Data Organization in Spreadsheets and Introduction to R in Data Carpentry Workshop.
- **Summer 2019:** Guided Programming with Python in Software Carpentry Workshop.
- **Spring 2019:** Guided Programming with Python in Software Carpentry Workshop.
- **Fall 2014-Spring 2016** Tutor at Rutgers University Camden Learning Center.

Additional Experiences

- **Internship Summer 2011** University of Pennsylvania, High Energy Physics Laboratory: Developed code to track annealing rate of irradiated transistors.

Presentations

- **2020 Paper Talk:** Boundary lipids of the nicotinic acetylcholine receptor in model and native membranes, Center for Computational and Integrative Biology, Rutgers University Camden, NJ 2020.
- **2020 Seminar:** Nicotinic Acetylcholine Receptors Lipid Preferences Within Complex Quasi-Native Membranes, Center for Computational and Integrative Biology, Rutgers University Camden, NJ 2020.
- **2020 Poster:** Nicotinic Acetylcholine Receptors Lipid Preferences Within Complex Quasi-Native Membranes, Biophysical Society Annual Meeting, San Diego, CA 2020.
- **2019 Demonstrations:** Science Carnival, Science on the Parkway, Science Week, Philadelphia, PA 2019.
- **2019 Seminar:** Boundary Lipids Of The Nicotinic Acetylcholine Receptor In Quasi-Native Membranes, Q-Step, Rutgers University Camden, NJ 2019.
- **2019 Poster:** Boundary Lipids Of The Nicotinic Acetylcholine Receptor In Quasi-Native Membranes, Biophysical Society Annual Meeting, Baltimore, MD 2019.
- **2018 Seminar:** Boundary Lipids of the Nicotinic Acetylcholine Receptor in Quasi-Native Membranes, Center For Computational and Integrative Biology, Rutgers University, Camden, NJ. 2018.
- **2018 Poster:** Interactions of nicotinic acetylcholine receptors with cholesterol and polyunsaturated fatty acids in model, native-like, and oocyte membranes. Biophysical Society Annual Meeting, San Francisco, CA. 2018.
- **2017 Seminar:** A Coarse Grained Study of Nicotinic Acetylcholine Receptor-Lipid Interactions, Center For Computational and Integrative Biology, Rutgers University, Camden, NJ. 2017.
- **2017 Poster:** Interactions of nicotinic acetylcholine receptors with liquid-disordered domains rich in n-3 polyunsaturated fatty acids. Biophysical Society Annual Meeting, New Orleans, LA. 2017.

- **2016 Poster:** Effects of quasi-native lipid composition on membrane domain formation induced by nicotinic acetylcholine receptors. Biophysical Society Annual Meeting, Los Angeles, CA. 2016.

Awards and Allocations:

- **2019 CCIB Best Paper Award (3rd Place)**
- **2019** The Rutgers Office of Advanced Research Computing Allocation; ~30000000 Service Units Allotted
- **2018 CCIB Best Poster Award (3rd Place)**

Technical skills

- **Programming Languages:** Proficient in: Python, TCL, Bash, git, TeX.
- **Industry Software Skills:** GROMACS, VMD, Slurm, Spyder, MATLAB.

Bibliography

- [1] Abadji, V. C., Raines, D. E., Watts, A., & Miller, K. W. 1993, Biochimica et Biophysica Acta (BBA)-Biomembranes, 1147, 143
- [2] Abraham, M. J., Murtola, T., Schulz, R., et al. 2015, SoftwareX, 1-2, 19
- [3] Addona, G. H., Jr, H. S., Kloczewiak, M. A., Husain, S. S., & Miller, K. W. 1998, Biochimica et Biophysica Acta (BBA)-Biomembranes, 1370, 299
- [4] Adibhatla, R. M., & Hatcher, J. F. 2007, Future lipidology, 2, 403
- [5] Albuquerque, E. X., Pereira, E. F. R., Alkondon, M., & Rogers, S. W. 2009, Physiological Reviews, 89, 73, pMID: 19126755
- [6] Althoff, T., Hibbs, R. E., Banerjee, S., & Gouaux, E. 2014, Nature, 512, 333
- [7] Amminger, G. P., Schäfer, M. R., Papageorgiou, K., et al. 2010, Archives of general psychiatry, 67, 146
- [8] Anholt, R., Lindstrom, J., & Montal, M. 1980, European journal of biochemistry, 109, 481
- [9] Antollini, S. S., & Barrantes, F. J. 2016, Frontiers in physiology, 7, 573
- [10] Aranda-Espinoza, H., Berman, a., Dan, N., Pincus, P., & Safran, S. A. 1996, Biophysical journal, 71, 648
- [11] Arnold, A. S., Gueye, M., Guettier-Sigrist, S., et al. 2004, Laboratory Investigation, 84, 1271
- [12] Baaden, M., & Marrink, S. J. 2013, Current Opinion in Structural Biology, 23, 878 , catalysis and regulation / Protein-protein interactions
- [13] Baenziger, J. E., & Corringer, P.-J. 2011, Neuropharmacology, 60, 116
- [14] Baenziger, J. E., Domville, J. A., & Therien, J. P. D. 2017, Current topics in membranes, 80, 95
- [15] Baenziger, J. E., Hénault, C. M., Therien, J. P. D., & Sun, J. 2015, Biochimica et Biophysica Acta - Biomembranes, 1848, 1806
- [16] Baenziger, J. E., Morris, M.-l., Darsaut, T. E., & Ryan, S. E. 2000, Journal of Biological Chemistry, 275, 777

- [17] Baier, C. J., Fantini, J., & Barrantes, F. J. 2011, *Scientific Reports*, 1, 69
- [18] Barrantes, F. J. 1989, *Critical Reviews in Biochemistry and Molecular Biology*, 24, 437
- [19] —. 2007, *Journal of neurochemistry*, 103, 72
- [20] —. 2010, *Sub-Cellular Biochemistry*, 51, 467
- [21] —. 2014, Cell-surface translational dynamics of nicotinic acetylcholine receptors, doi:10.3389/fnsyn.2014.00025
- [22] Barrantes, F. J., Antollini, S. S., Blanton, M. P., & Prieto, M. 2000, *Journal of Biological Chemistry*, 275, 37333
- [23] Barrantes, F. J., Bermudez, V., Borroni, M. V., et al. 2010, in *Journal of Molecular Neuroscience*, Vol. 40, 87–90
- [24] Basak, S., Schmandt, N., Gicheru, Y., & Chakrapani, S. 2017, *eLife*, 6, e23886
- [25] Bednarczyk, P., Szewczyk, A., & Dolowy, K. 2002, *Acta Biochimica Polonica*
- [26] Bednarczyk, P., Szewczyk, A., & Dołowy, K. 2002, *Acta Biochimica Polonica*, 49, 869
- [27] Bennett, S. A. L., Valenzuela, N., Xu, H., et al. 2013, *Frontiers in Physiology*, 4 JUL, 1
- [28] Berendsen, H., van der Spoel, D., & van Drunen, R. 1995, *Computer Physics Communications*, 91, 43
- [29] Berger, G. E., Smesny, S., & Amminger, G. P. 2006, *International Review of Psychiatry*, 18, 85
- [30] Bermúdez, V., Antollini, S. S., Fernández Nievas, G. A., Aveldaño, M. I., & Barrantes, F. J. 2010, *J. Lipid Res.*, 51, 2629
- [31] Bermudez, V., Antollini, S. S., Nievas, G. A. F., Aveldao, M. I., & Barrantes, F. J. 2010, *Journal of lipid research*, 51, 2629
- [32] Bhushan, A., & McNamee, M. G. 1993, *Biophysical journal*, 64, 716
- [33] Bleecker, J. V., Cox, P. A., & Keller, S. L. 2016, *Biophysical Journal*, 110, 2305
- [34] Bond, P. J., & Sansom, M. S. P. 2006, *Journal of the American Chemical Society*, 128, 2697
- [35] Borroni, M. V., Vallés, A. S., & Barrantes, F. J. 2016, *Biochimica et biophysica acta*, 1858, 2662

- [36] Bouzat, C. B., & Barrantes, F. J. 1993, Receptors & channels, 1, 251
- [37] Brannigan, G. 2017, Current topics in membranes, 80, 163
- [38] Brannigan, G., & Brown, F. 2006, Biophys J, 90, 1501
- [39] Brannigan, G., & Brown, F. L. 2005, Journal of Chemical Physics, 122, doi:10.1063/1.1851983
- [40] —. 2007, Biophysical Journal, 92, 864
- [41] Brannigan, G., Henin, J., Law, R., Eckenhoff, R., & Klein, M. L. 2008, Proceedings of the National Academy of Sciences, 105, 14418
- [42] Brannigan, G., Hénin, J., Law, R., Eckenhoff, R., & Klein, M. L. 2008, Proceedings of the National Academy of Sciences, 105, 14418
- [43] Breckenridge, W., Gombos, G., & Morgan, I. 1972, Biochimica et Biophysica Acta (BBA) - Biomembranes, 266, 695
- [44] Breckenridge, W., Morgan, I., Zanetta, J., & Vincendon, G. 1973, Biochimica Et Biophysica Acta Bba - Gen Subj, 320, 681
- [45] Breckenridge, W. C., Morgan, I. G., Zanetta, J. P., & Vincendon, G. 1973, BBA - General Subjects, 320, 681
- [46] Bristow, D. R., & Martin, I. L. 1987, Journal of Neurochemistry, 49, 1386
- [47] Brown, D. A. 2007, Methods in molecular biology (Clifton, N.J.), 398, 9
- [48] Brusés, J. L., Chauvet, N., & Rutishauser, U. 2001, Journal of Neuroscience, 21, 504
- [49] Budelier, M. M., Cheng, W. W. L., Chen, Z. W., et al. 2019, Biochimica et Biophysica Acta - Molecular and Cell Biology of Lipids, 1864, 128
- [50] Buehler, L. K. 2016, Cell membranes (Garland Science, Taylor Francis Group)
- [51] Burger, K., Gimpl, G., & Fahrenholz, F. 2000, Cellular and Molecular Life Sciences, 57, 1577
- [52] Bushe, C., & Paton, C. 2005, Journal of Psychopharmacology, 19, 76
- [53] Butler, D. H., & McNamee, M. G. 1993, Biochimica et Biophysica Acta (BBA) - Biomembranes, 1150, 17
- [54] Campagna, J., & Fallon, J. 2006, Neuroscience, 138, 123
- [55] Carpenter, T. S., López, C. A., Neale, C., et al. 2018, Journal of Chemical Theory and Computation, 14, 6050

- [56] Carswell, C. L., Hénault, C. M., Murlidaran, S., et al. 2015, *Structure*, 23, 1655
- [57] Celie, P. H., Van Rossum-Fikkert, S. E., Van Dijk, W. J., et al. 2004, *Neuron*, 41, 907
- [58] Chang, H. W., & Bock, E. 1977, *Biochemistry*, 16, 4513
- [59] Changeux, J.-P., Corringer, P.-J., & Maskos, U. 2015, *Neuropharmacology*, 96, 135
- [60] Chavent, M., Duncan, A. L., & Sansom, M. S. 2016, *Current Opinion in Structural Biology*, 40, 8
- [61] Chen, Q., Kinde, M. N., Arjunan, P., et al. 2015, *Sci Rep*, 5, 13833
- [62] Chen, Z. W., & Olsen, R. W. 2007, *Journal of Neurochemistry*, 100, 279
- [63] Chen, Z. W., Bracamontes, J. R., Budelier, M. M., et al. 2019, *PLoS Biology*, 17, 1
- [64] Cheng, M. H., Liu, L. T., Saladino, A. C., Xu, Y., & Tang, P. 2007, *The Journal of Physical Chemistry B*, 111, 14186
- [65] Cheng, M. H., Xu, Y., & Tang, P. 2009, *Journal of Physical Chemistry B*, 113, 6964
- [66] Cheng, W. W. L., Chen, Z. W., Bracamontes, J. R., et al. 2018, *Journal of Biological Chemistry*, 293, 3013
- [67] Chorev, D. S., Baker, L. A., Wu, D., et al. 2018, *Science (New York, N.Y.)*, 362, 829
- [68] Cicuta, P., Keller, S. L., & Veatch, S. L. 2007, *Journal of Physical Chemistry B*, 111, 3328
- [69] CM, M., Court, J., & Molnar, E. 1999, *Journal of ...*, doi:10.1046/j.1471-4159.1999.0731635.x
- [70] Conquer, J. A., Tierney, M. C., Zecevic, J., Bettger, W. J., & Fisher, R. H. 2000, *Lipids*, 35, 1305
- [71] Conti, L., Limon, A., Palma, E., & Miledi, R. 2013, *The Biological bulletin*, 224, 47
- [72] Corbin, J., Wang, H. H., & Blanton, M. P. 1998, *Biochimica et Biophysica Acta (BBA)-Biomembranes*, 1414, 65
- [73] Cordero-Morales, J. F., & Vásquez, V. 2018, *Current Opinion in Structural Biology*, 51, 92

- [74] Cornelison, G. L., Pflanz, N. C., Tipps, M. E., & Mihic, S. J. 2016, European Journal of Pharmacology, 780, 252
- [75] Corradi, V., Mendez-Villuendas, E., Ingólfsson, H. I., et al. 2018, ACS Central Science, 4, 709
- [76] Corrie, J., Ogrel, A. A., Mccardy, E. A., Blanton, M. P., & Baenziger, J. E. 2002, Journal of Biological Chemistry, 277, 201
- [77] Corringer, P.-J., Poitevin, F., Prevost, M. S., et al. 2012, Structure, 20, 941
- [78] Cotman, C., Blank, M. L., Moehl, A., & Snyder, F. 1969, Biochemistry, 8, 4606
- [79] Criado, M., Eibl, H., & Barrantes, F. 1982, Biochemistry, 21, 3622
- [80] Criado, M., Eibl, H., & Barrantes, F. J. 1983, Biochemistry, 22, 524
- [81] —. 1984, Functional properties of the acetylcholine receptor incorporated in model lipid membranes. Differential effects of chain length and head group of phospholipids on receptor affinity states and receptor-mediated ion translocation, Tech. Rep. 14
- [82] DaCosta, C. J., Medaglia, S. A., Lavigne, N., et al. 2009, Journal of Biological Chemistry, 284, 33841
- [83] DaCosta, C. J., Wagg, I. D., McKay, M. E., & Baenziger, J. E. 2004, Journal of Biological Chemistry, 279, 14967
- [84] Dacosta, C. J. B., & Baenziger, J. E. 2013, Structure, 21, 1271
- [85] daCosta, C. J. B., Ogrel, A. A., McCardy, E. A., Blanton, M. P., & Baenziger, J. E. 2001, Journal of Biological Chemistry, 277, 201
- [86] Dalziel, A. W., Rollins, E. S., & McNamee, M. G. 1980, FEBS Letters, 122, 193
- [87] Dan, N., Pincus, P., & Safran, S. A. 1993, Langmuir, 9, 2768
- [88] Dani, J. A. 2001, Biological psychiatry, 49, 166
- [89] De Felice, C., Signorini, C., Durand, T., et al. 2012, Genes and Nutrition, 7, 447
- [90] De Jong, D. H., Singh, G., Drew Bennett, W. F., et al. 2012, doi:10.1021/ct300646g
- [91] Di Paolo, G., & Kim, T.-W. 2011, Nature Reviews Neuroscience, 12, 284
- [92] Domanski, J., Marrink, S. J., & Schaefer, L. V. 2012, Biochimica et Biophysica Acta (BBA)-Biomembranes, 1818, 984

- [93] Dostalova, Z., Zhou, X., Liu, A., et al. 2014, Protein science : a publication of the Protein Society, 23, 157
- [94] Dunn, S. M., Martin, C. R., Agey, M. W., & Miyazaki, R. 1989, Biochemistry, 28, 2545
- [95] Egea, J., Buendia, I., Parada, E., et al. 2015, Anti-inflammatory role of microglial alpha7 nAChRs and its role in neuroprotection, doi:10.1016/j.bcp.2015.07.032
- [96] Ellena, J. F., Blazing, M. A., & McNamee, M. G. 1983, Biochemistry, 22, 5523
- [97] Epstein, M., & Racker, E. 1978, The Journal of Biological Chemistry, 253, 6660
- [98] Escribá, P. V. 2017, doi:10.1016/j.bbamem.2017.05.017
- [99] Feller, S. E. 2008, Chemistry and Physics of Lipids, 153, 76
- [100] Ferreira, C. R., Saraiva, S. a., Catharino, R. R., et al. 2010, Journal of lipid research, 51, 1218
- [101] Flinner, N., & Schleiff, E. 2015, PLoS ONE, 10, 1
- [102] Fong, T., & McNamee, M. 1987, Biochemistry, doi:10.1021/bi00387a020
- [103] Fong, T. M., & McNamee, M. G. 1986, Biochemistry, 25, 830
- [104] Fournier, J. B., & Galatola, P. 2015, European Physical Journal E, 38, 1
- [105] Gahbauer, S., & Böckmann, R. A. 2016, Frontiers in Physiology, 7, 494
- [106] Gamba, G., Hill, W. G., Southern, N. M., et al. 2005, American Journal of Physiology-Renal Physiology, 15261, 217
- [107] Gawrisch, K., Eldho, N. V., & Holte, L. L. 2003in , 445–452
- [108] Georgieva, R., Chachaty, C., Hazarosova, R., et al. 2015, Biochimica et Biophysica Acta (BBA) - Biomembranes, 1848, 1424
- [109] Gonzalez-Ros, J. M., Llanillo, M., Paraschos, A., & Martinez-Carrion, M. 1982, Biochemistry, 21, 3467
- [110] Goose, J. E., & Sansom, M. S. 2013, PLoS Computational Biology, 9, 1003033
- [111] Gotti, C., Fornasari, D., & Clementi, F. 1997, Prog Neurobiol, 53, 199
- [112] Goulian, M. 1996, Current Opinion in Colloid & Interface Science, 1, 358

- [113] Goulian, M., Bruinsma, R., & Pincus, P. 1993, EPL (Europhysics Letters), 22, 145
- [114] Guesnet, P., & Alessandri, J. M. 2011, Biochimie, 93, 7
- [115] Gupta, K., Li, J., Liko, I., et al. 2018, Nature protocols, 13, 1106
- [116] Guros, N. B., Balijepalli, A., & Klauda, J. B. 2020, Proceedings of the National Academy of Sciences of the United States of America, 117, 405
- [117] Hamazaki, K., Maekawa, M., Toyota, T., et al. 2015, Psychiatry Research, 227, 353
- [118] Hamouda, A. K., Chiara, D. C., Sauls, D., Cohen, J. B., & Blanton, M. P. 2006, Biochemistry, 45, 976
- [119] Hamouda, A. K., Sanghvi, M., Sauls, D., Machu, T. K., & Blanton, M. P. 2006, Biochemistry, 45, 4327
- [120] Haydar, S. N., & Dunlop, J. 2010, Current topics in medicinal chemistry, 10, 144
- [121] Hénault, C. M., Sun, J., Therien, J. P. D., et al. 2015, Neuropharmacology, 96, 157
- [122] Hénault, C. M., Govaerts, C., Spurny, R., et al. 2019, Nature Chemical Biology, doi:10.1038/s41589-019-0369-4
- [123] Hénin, J., Salari, R., Murlidaran, S., & Brannigan, G. 2014, Biophysical Journal, 106, 1938
- [124] Hénin, J., Salari, R., Murlidaran, S., & Brannigan, G. 2014, Biophys. J., 106, 1938
- [125] Hibbs, R. E., & Gouaux, E. 2011, Nature, 474, 54
- [126] Humphrey, W., Dalke, A., & Schulten, K. 1996, Journal of Molecular Graphics, 14, 33
- [127] Hung, A., & Yarovsky, I. 2011, Biochemistry, 50, 1492
- [128] Ingólfsson, H. I., Carpenter, T. S., Bhatia, H., et al. 2017, Biophysical Journal, 113, 2271
- [129] Ingólfsson, H. I., Melo, M. N., Van Eerden, F. J., et al. 2014, Journal of the American Chemical Society, 136, 14554
- [130] Ingólfsson, H. I., Bhatia, H., Zeppelin, T., et al. 2020, The journal of physical chemistry. B, 124, 7819

- [131] Iyer, S. S., Tripathy, M., & Srivastava, A. 2018, Biophysical Journal, 115, 117
- [132] Jaiteh, M., Taly, A., & Hénin, J. 2016, PLoS One, 11, e0151934
- [133] Jensen, M. Ø., & Mouritsen, O. G. 2004, Biochimica et biophysica acta, 1666, 205
- [134] Jones, O. T., Eubanks, J. H., Earnest, J. P., & McNamee, M. G. 1988, Biochemistry, 27, 3733
- [135] Jones, O. T., & Mcnamee, M. G. 1988, Biochemistry, 27, 2364
- [136] Joseph, T. T., & Mincer, J. S. 2016, PLoS ONE, 11, 1
- [137] Kaiser, H.-J., Lingwood, D., Levental, I., et al. 2009, Proceedings of the National Academy of Sciences, 106, 16645
- [138] Kalamida, D., Poulas, K., Avramopoulou, V., et al. 2007, FEBS Journal, 274, 3799
- [139] Kim, J. J., Gharpure, A., Teng, J., et al. 2020, Nature, 585, 303
- [140] Kim, J. Y., Kinoshita, M., Ohnishi, M., & Fukui, Y. 2001, Reproduction, 122, 131
- [141] Kim, K. S., Neu, J., & Oster, G. 1998, Biophysical Journal, 75, 2274
- [142] Klaassen, C. D., & Watkins, J. B. 2015, Casarett & Doull's essentials of toxicology (McGraw Hill Professional)
- [143] Koga, N., Ogura, J., Yoshida, F., et al. 2019, Translational Psychiatry, 9, doi:10.1038/s41398-019-0536-0
- [144] Kouvatsos, N., Giastas, P., Chroni-Tzartou, D., Poulopoulou, C., & Tzartos, S. J. 2016, Proceedings of the National Academy of Sciences, 113, 9635
- [145] Kumar, P., Wang, Y., Zhang, Z., et al. 2020, Proceedings of the National Academy of Sciences of the United States of America, 117, 1788
- [146] —. 2019, doi:10.1073/pnas.1906823117/-/DCSupplemental
- [147] Kumari, S., Borroni, V., Chaudhry, A., et al. 2008, Journal of Cell Biology, 181, 1179
- [148] Landreh, M., Marty, M. T., Gault, J., & Robinson, C. V. 2016, A sliding selectivity scale for lipid binding to membrane proteins, arXiv:NIHMS150003
- [149] Lavandera, J. V., Saín, J., Fariña, A. C., Bernal, C. A., & González, M. A. 2017, Nutritional Neuroscience, 20, 424

- [150] Laverty, D., Thomas, P., Field, M., et al. 2017, *Nature Structural & Molecular Biology*, 1
- [151] Laverty, D., Desai, R., Uchański, T., et al. 2019, *Nature*, 565, 516
- [152] Lee, A. G. 2004, How lipids affect the activities of integral membrane proteins, doi:10.1016/j.bbamem.2004.05.012
- [153] Leibel, W. S., Firestone, L. L., Legler, D. C., Braswell, L. M., & Miller, K. W. 1987, *Biochimica et Biophysica Acta (BBA) - Biomembranes*, 897, 249
- [154] Lennon, V. A., Ermilov, L. G., Szurszewski, J. H., & Vernino, S. 2003, *J Clin Invest*, 111, 907
- [155] Levental, K., Lorent, J., Lin, X., Skinkle, A., & Surma, M. 2016, *Biophysical journal*
- [156] Liam Sharp, G. B. 2020, DensityMap, github
- [157] Lin, X., Gorfe, A. A., & Levental, I. 2018, *Biophysical Journal*, 114, 1936
- [158] Lingwood, D., & Simons, K. 2010, *Science*, 327, 46
- [159] Lorent, J., Ganesan, L., Rivera-Longsworth, G., et al. 2019, *bioRxiv*, 698837
- [160] Lorent, J. H., Levental, K. R., Ganesan, L., et al. 2020, *Nature Chemical Biology*, 16, 644
- [161] Lorenzen, K., & van Duijn, E. 2010, *Current Protocols in Protein Science*, 1
- [162] Maekawa, M., Watanabe, A., Iwayama, Y., et al. 2017, *Translational Psychiatry*, 7, 1
- [163] Manor, I., Magen, A., Keidar, D., et al. 2011, *European Psychiatry*, 27, 335
- [164] Mantipragada, S. B., Horváth, L. I., Arias, H. R., et al. 2003, *Biochemistry*, 42, 9167
- [165] Marchand, S., Devillers-Thiéry, A., Pons, S., Changeux, J.-P., & Cartaud, J. 2002, *The Journal of neuroscience : the official journal of the Society for Neuroscience*, 22, 8891
- [166] Marrink, S. J., Corradi, V., Souza, P. C., et al. 2019, *Chemical Reviews*, 119, 6184
- [167] Marrink, S. J., Risselada, H. J., Yefimov, S., Tielemans, D. P., & de Vries, A. H. 2007, *The Journal of Physical Chemistry B*, 111, 7812, pMID: 17569554
- [168] Marrink, S. J., Risselada, H. J., Yefimov, S., Tielemans, D. P., & Vries, A. H. D. 2007, *The Journal of Physical Chemistry B*, 111, 7812

- [169] Marsh, D. 2010, *Biochimica et Biophysica Acta (BBA)-Biomembranes*, 1798, 688
- [170] Marsh, D., & Barrantes, F. 1978, *Proceedings of the National Academy of Sciences*, 75, 4329
- [171] Marsh, D., Watts, A., & Barrantes, F. 1981, *Biochimica et Biophysica Acta (BBA)-Biomembranes*, 645, 97
- [172] Masiulis, S., Desai, R., Uchański, T., et al. 2019, *Nature*, 565, 454
- [173] McEvoy, T. G., Coull, G. D., Broadbent, P. J., Hutchinson, J. S. M., & Speake, B. K. 2000, *J Reprod Fertil*, 118, 163
- [174] McNamara, R. K., Jandacek, R., Rider, T., et al. 2008, *Psychiatry Research*, 160, 285
- [175] McNamara, R. K., Ostrander, M., Abplanalp, W., et al. 2006, *Prostaglandins Leukotrienes and Essential Fatty Acids*, 75, 237
- [176] McNamee, M., Ellena, J., & Dalziel, A. 1982, *Biophysical journal*, 37, 103
- [177] McNamee, M., & Fong, T. 1988, *Lipid Domains and the Relationship to Membrane Function*. New York, Liss, 43
- [178] Middlemas, D. S., & Raftery, M. A. 1987, *Biochemistry*, 26, 1219
- [179] Miyazawa, A., Fujiyoshi, Y., & Unwin, N. 2003, *Nature*, 423, 949
- [180] Mlayeh, L., Chatkaew, S., Léonetti, M., & Homblé, F. 2010, *Biophysical Journal*, 99, 2097
- [181] Moffett, S. X., Klein, E. A., Brannigan, G., & Martin, J. V. 2019, *PLoS ONE*, 14, 1
- [182] Morales-Perez, C. L., Noviello, C. M., & Hibbs, R. E. 2016, *Nature*, 538, 411
- [183] Mukhtasimova, N., DaCosta, C. J. B., & Sine, S. M. 2016, *The Journal of General Physiology*, 148, 43
- [184] Narayanaswami, V., & McNamee, M. G. 1993, *Biochemistry*, 32, 12420, pMID: 8241132
- [185] Nemecz, Á., Prevost, M. S., Menny, A., & Corringer, P. J. 2016, *Neuron*, 90, 452
- [186] Nemecz, Á., Prevost, M. S., Menny, A., & Corringer, P.-J. 2016, *Neuron*, 90, 452

- [187] Nys, M., Wijckmans, E., Farinha, A., et al. 2016, Proceedings of the National Academy of Sciences, 113, E6696
- [188] Ochoa, E. L., Dalziel, A. W., & Mcnamee, M. G. 1983, Biochimica et Biophysica Acta (BBA)-Biomembranes, 727, 151
- [189] Olsen, R. E., Dragnes, B. T., Myklebust, R., & Ringø, E. 2003, Fish Physiology and Biochemistry, 29, 181
- [190] Oshikawa, J., Toya, Y., Fujita, T., et al. 2003, American journal of physiology. Cell physiology, 285, C567
- [191] Ourisson, G., & Rohmer, M. 1992, Acc. Chem. Res, 25, 403
- [192] Padilla-Morales, L. F., Colón-Sáez, J. O., González-Nieves, J. E., Quesada-González, O., & Lasalde-Dominicci, J. A. 2016, Biochimica et biophysica acta, 1858, 47
- [193] Pan, J., Chen, Q., Willenbring, D., et al. 2012, Nat Commun, 3, 714
- [194] Parton, D., Tek, A., Baaden, M., & Sansom, M. 2013, PLoS Comput Biol, 9, e1003034
- [195] Patel, H., McIntire, J., Ryan, S., Dunah, A., & Loring, R. 2017, Journal of Neuroinflammation, 14, doi:10.1186/s12974-017-0967-6
- [196] Pato, C., Stetzkowski-Marden, F., Gaus, K., et al. 2008, Chemico-Biological Interactions, 175, 64
- [197] Peet, M. 2003, Prostaglandins Leukotrienes and Essential Fatty Acids, 69, 477
- [198] Perillo, V. L., Peñalva, D. A., Vitale, A. J., Barrantes, F. J., & Antollini, S. S. 2016, Archives of Biochemistry and Biophysics, 591, 76
- [199] Periole, X., Cavalli, M., Marrink, S., & Ceruso, M. A. 2009, 5, 2531
- [200] Periole, X., Cavalli, M., Marrink, S. J., & Ceruso, M. A. 2009, Journal of Chemical Theory and Computation, 5, 2531
- [201] Picciotto, M., & Zoli, M. 2008, Front Biosci
- [202] Piomelli, D., Astarita, G., & Rapaka, R. 2007, Nat Rev Neurosci, 8, 743
- [203] Polovinkin, L., Gherici Hassaine, G., Perot, J., et al. 2018, Nature, doi:10.1038/s41586-018-0672-3
- [204] Prevost, M. S., Sauguet, L., Nury, H., et al. 2012, Nature structural & molecular biology, 19, 642
- [205] Pronk, S., Pöll, S., Schulz, R., et al. 2013, Bioinformatics

- [206] Pucadyil, T. J., & Chattopadhyay, A. 2006, Progress in lipid research, 45, 295
- [207] Pun, S., Sigrist, M., Santos, A. F., et al. 2002, Neuron, 34, 357
- [208] Quesada, O., González -Freire, C., Ferrer, M. C., et al. 2016, Scientific Reports, 6, 32766
- [209] Ramarao, M. K., & Cohen, J. B. 1998, Proceedings of the National Academy of Sciences of the United States of America, 95, 4007
- [210] Rankin, S. E., Addona, G. H., Kloczewiak, M. A., Bugge, B., & Miller, K. W. 1997, Biophysical journal, 73, 2446
- [211] Regost, C., Arzel, J., Robin, J., Rosenlund, G., & Kaushik, S. J. 2003, Aquaculture, 217, 465
- [212] Rüchel, R., Watters, D., & Maelicke, A. 1981, European journal of biochemistry, 119, 215
- [213] Salari, R., Joseph, T., Lohia, R., Henin, J., & Brannigan, G. 2018, arXiv:1801.04901
- [214] Salari, R., Murlidaran, S., & Brannigan, G. 2014, Mol. Simul., 40, 821
- [215] Santiago, J., Guzmán, G. R., Rojas, L. V., et al. 2001, Journal of Biological Chemistry, 276, 46523
- [216] Sauguet, L., Howard, R. J., Malherbe, L., et al. 2013, Nature Communications, 4, 1
- [217] Sauguet, L., Shahsavari, A., Poitevin, F., et al. 2014, Proceedings of the National Academy of Sciences, 111, 966
- [218] SCHIEBLER, W., & HUCHO, F. 1978, European Journal of Biochemistry, 85, 55
- [219] Schindler, H., Spillecke, F., & Neumann, E. 1984, Proceedings of the National Academy of Sciences of the United States of America, 81, 6222
- [220] Schneider, M., Levant, B., Reichel, M., et al. 2017, Neuroscience and Biobehavioral Reviews, 76, 336
- [221] Schneiter, R., Brügger, B., Sandhoff, R., et al. 1999, Journal of Cell Biology, 146, 741
- [222] Scott, K. A., Bond, P. J., Iveta, A., et al. 2008, Structure, 16, 621
- [223] Sezgin, E., Levental, I., Grzybek, M., et al. 2012, Biochimica et Biophysica Acta - Biomembranes, 1818, 1777

- [224] Shaikh, S. R., Dumaual, A. C., Castillo, A., et al. 2004, Biophysical Journal, 87, 1752
- [225] Sharp, L., Salari, R., & Brannigan, G. 2019, Biochimica et biophysica acta. Biomembranes, doi:10.1016/j.bbamem.2019.01.005
- [226] Shevchenko, A., & Simons, K. 2010, Nature Reviews Molecular Cell Biology, 11, 593
- [227] Simons, K., & Ikonen, E. 1997, Nature, 387, 569
- [228] Simons, K., & Toomre, D. 2000, Nature Reviews Molecular Cell Biology, 1, 31
- [229] Smithers, N., Bolivar, J. H., Lee, A. G., & East, J. M. 2012, Biochemistry, 51, 7996
- [230] Sodt, A. J., Sandar, M. L., Gawrisch, K., Pastor, R. W., & Lyman, E. 2014, Journal of the American Chemical Society, 136, 725
- [231] Søgaard, R., Werge, T. M., Bertelsen, C., et al. 2006, Biochemistry, 45, 13118
- [232] Sooksawate, T., & Simmonds, M. A. 2001, Neuropharmacology, 40, 178
- [233] Stetzkowski-Marden, F., Gaus, K., Recouvreur, M., Cartaud, A., & Cartaud, J. 2006, Journal of lipid research, 47, 2121
- [234] Stillwell, W., & Wassall, S. R. 2003, Docosahexaenoic acid: Membrane properties of a unique fatty acid, doi:10.1016/S0009-3084(03)00101-4
- [235] Sunshine, C., & McNamee, M. G. 1992, Biochimica Et Biophysica Acta (BBA)-Biomembranes, 1108, 240
- [236] —. 1994, Biochimica et Biophysica Acta (BBA)-Biomembranes, 1191, 59
- [237] Taguchi, R., & Ishikawa, M. 2010, Journal of Chromatography A, doi:10.1016/j.chroma.2010.04.034
- [238] Taly, A., Corringer, P.-J., Guédin, D., Lestage, P., & Changeux, J.-P. 2009, Nature Publishing Group, 8, doi:10.1038/nrd2927
- [239] Thompson, M. J., & Baenziger, J. E. 2020, Biochimica et Biophysica Acta (BBA) - Biomembranes, 1862, 183304
- [240] Tong, A., Hsu, F. F., Schmidpeter, P. A., et al. 2019, eLife, 8, doi:10.7554/eLife.50766
- [241] Turk, H. F., & Chapkin, R. S. 2013, Prostaglandins Leukotrienes and Essential Fatty Acids, 88, 43

- [242] Unwin, N. 2005, *Journal of Molecular Biology*, 346, 967
- [243] —. 2017, *IUCrJ*, 4, 393
- [244] van Meer, G., & de Kroon, A. I. P. M. 2010, *Journal of Cell Science*, 124, 5
- [245] Walstab, J., Rappold, G., & Niesler, B. 2010, *Pharmacology & Therapeutics*, 128, 146
- [246] Wassall, S. R., & Stillwell, W. 2008, *Chemistry and Physics of Lipids*, 153, 57
- [247] Wassenaar, T. A., Ingólfsson, H. I., Bo ckmann, R. A., Tielemans, D. P., & Marrink, S. J. 2015, *Journal of Chemical Theory and Computation*, 11, 2144
- [248] Wenz, J. J., & Barrantes, F. J. 2005, *Biochemistry*, 44, 398
- [249] Westergard, T., Salari, R., Martin, J. V., & Brannigan, G. 2015, *PLoS ONE*, 10, 1
- [250] Willmann, R., Pun, S., Stallmach, L., et al. 2006, *The EMBO journal*, 25, 4050
- [251] Wilson, K. A., MacDermott-Opeskin, H. I., Riley, E., Lin, Y., & O'Mara, M. L. 2020, *Biochemistry*, 59, 3010
- [252] Woods, K., Sharp, L., & Brannigan, G. 2019, *Journal of Membrane Biology*, 252, 385
- [253] Xiong, W., Cui, T., Cheng, K., et al. 2012, *The Journal of Experimental Medicine*, 209, 1121
- [254] Yadav, R. S., & Tiwari, N. K. 2014, *Lipid Integration in Neurodegeneration: An Overview of Alzheimer's Disease*, doi:10.1007/s12035-014-8661-5
- [255] Yeagle, P. L. 2016, Chapter 7-structures of lipid assemblies, 115–154
- [256] —. 2016, Chapter 9-Cholesterol and Related Sterols, 191–215
- [257] —. 2016, *The Membranes of Cells*, 3rd edn. (Elsevier Science)
- [258] Yocum, G. T., Turner, D. L., Danielsson, J., et al. 2017, *American Journal of Physiology - Lung Cellular and Molecular Physiology*, 313, L406
- [259] Zabrecky, J. R., & Raftery, M. A. 1985, *Journal of Receptors and Signal Transduction*, 5, 397
- [260] Zhou, Y., Nelson, M. E., Kuryatov, A., et al. 2003, *The Journal of neuroscience : the official journal of the Society for Neuroscience*, 23, 9004

- [261] Zhu, D., Xiong, W. C., & Mei, L. 2006, *The Journal of neuroscience : the official journal of the Society for Neuroscience*, 26, 4841
- [262] Zhu, S., Noviello, C. M., Teng, J., et al. 2018, *Nature*, 559, 67
- [263] Zingsheim, H. P., Neugebauer, D. C., Frank, J., Hänicke, W., & Barrantes, F. J. 1982, *The EMBO journal*, 1, 541
- [264] Zuber, B., & Unwin, N. 2013, *Proceedings of the National Academy of Sciences of the United States of America*, 110, 10622